SURFACE DEGRADATION AND CREEP OF INCONEL 617 AND HAYNES 230 AT HIGH TEMPERATURES

BY

HSIAO-MING TUNG

DISSERTATION

Submitted in partial fulfillment of the requirements
for the degree of Doctor of Philosophy in Nuclear Engineering
in the Graduate College of the
University of Illinois at Urbana-Champaign, 2012

Urbana, Illinois

Doctoral Committee:

Professor James F. Stubbins, Chair
Associate Professor Brent J. Heuser
Associate Professor Jian-Ku Shang
Professor Rizwan Uddin

ABSTRACT

The high temperature gas-cooled reactor (HTGR) design has been selected for the Next Generation Nuclear Plant (NGNP) project. The helium coolant in the primary circuit has been found to contain low levels of impurities (e.g. CO, CO_2, H_2O, CH_4, and H_2) after steady-state operation. This can lead to an environmental degradation of high temperature alloys used for internals and heat exchangers. Depending on the impurity concentration and the temperature, the materials can undergo oxidation, carburization and decarburization, which can be detrimental to the mechanical behavior of the materials. In addition, the most critical metallic component of the HTGR is the heat exchanger. The materials serve in the temperature range of 760-950^{o}C and withstand coolant pressure up to 7 MPa for a design life of 60 years. Therefore, understanding the environmental effects on the materials and the relevant creep deformation behavior is critical for the design and long-term operation of the HTGR.

Inconel 617 (alloy 617) and Haynes 230 (alloy 230) are considered as primary candidate materials for serving in the HTGR, due to their exceptional combination of high temperature strength and oxidation resistance. In this study, surface degradation owing to environmental effects as well as creep deformation of the two alloys were investigated. The alloys were exposed to air, He+5% H_2 and He+5% H_2 +1% CH_4 to study oxidizing, reducing (low-pO_2 gas), and carburizing phenomena. Short-term exposures were conducted from 850 to 1000^{o}C and long-term exposures (up to 1512 h) were performed at 950^{o}C. For the creep deformation studies, biaxial thermal creep behavior using a pressurized tube technique for both alloys was employed. The experimental results and microstructural characterization lead to the following conclusions:

1. Short-term exposure in air showed a two-stage oxidation kinetics for both alloys. For alloy 617, the transition between the stages was related to Cr outward diffusion in the Cr_2O_3 and the matrix. The second stage oxidation for alloy 230 is associated with the significant formation of $MnCr_2O_4$.

2. Results of long-term exposure indicated that around 360 h exposure in air, the oxide scale grown on alloy 617 consisted of Cr_2O_3 and $NiCr_2O_4$. Significant spallation of oxide scale resulted in the decrease in weight after 1224 h exposure as observed for alloy 617, while alloy 230 exhibited a stable increase in weight. Both short-term and long-term exposure indicated that alloy 230 possesses better oxidation resistance than alloy 617.

3. Exposures in a reducing environment caused a faster scale growth rate in alloy 617 whereas a slower scale growth rate was observed in alloy 230. Microstructural characterization showed that much finer grains were formed in low-pO_2 gas, compared with air environment for both alloys.

4. Carburization tests showed that alloy 617 had superior carburization resistance to alloy 230. X-ray diffraction analysis showed that chromium-rich carbide near the surface area is in a form of Cr_3C_2.

5. Residual stress measurement showed the intrinsic residual stress of Cr_2O_3 are tensile during the growth of the oxide for both alloys. The development of intrinsic stress with increasing exposure time in low-pO_2 gas is relatively stable than in air, which may be attributed to smaller grain size formed in the reducing environment.

6. Creep properties were measured with a biaxial creep tube technique. At 950^{o}C, alloy 617 and alloy 230 had similar creep rupture life, whereas alloy 230 exhibited better creep rupture life than alloy 617 at 850^{o}C. Nucleation, growth and coalescence of creep voids at grain boundaries are the dominant micro-mechanism for creep fracture. At the secondary creep regime, void formation was observed along grain boundaries and at triple junction of grain boundaries.

To my wife, Ching-Chun

ACKNOWLEDGMENTS

First of all, I would like to thank my dear Lord Jesus, who gives me unfading hope during the research period. He is always with me as I faced qualifying exam, preliminary exam and oral exam. The most important thing I learned is that he is the source of blessing and grace. He takes care of all my needs with tender care. And I just would like to say " Lord, you know all the things; you know that I love you." (John 21:17)

Secondly, I would like to thank my advisor, Prof. James Stubbins, for his guidance and patience during the early stage of my doctoral research. Without his support, it is not possible for me to accomplish this research. I also appreciate the committee members for the final exam of my doctoral degree: Prof. Uddin, Prof. Heuser, and Prof. Shang for their time and efforts to make this research better. Special thanks are given to Prof. Shang who provided valuable discussion for the creep tests. I am also grateful to Prof. J.-H. Huang and Prof. G.-P Yu from National Tsing Hua University in Taiwan for carrying out the oxygen partial pressure measurements. I would also like to thank to Dr. Haijun Yao from School of Chemical Science, University of Illinois at Urbana-Champaign for technical assistance of using thermogravimety analysis. I am also grateful to my colleague, Dr. Chen and Dr. Mo, who shared their experimental experience and ideals along with fruitful discussion. I would like to thank Dr. White from Haynes International Inc. for freely providing an plate of alloy 230 for corrosion studies. My appreciations also go to Yang Zhao who helped polish raw materials.

Thirdly, I would like to express my thanks to my fellow brethren in Christ for their bountiful supplies through prayer, including Fucheng Qu, Kuo-Ting Wang, Joe Chang, and other brothers in Hsinchu, Taiwan.

Fourthly, the work was supported by the U.S. Department of Energy (DOE) grants DE-FC07-07ID14819 and NEUP 09-516. The microstructural analysis was carried out in part in the Frederick Seitz Materials Research Laboratory Central Facilities, University of Illinois.

Finally, I am also deeply grateful to my parents with their support and love. I would like to express my love and gratitude in Christ to my wife, Ching-Chun, who always accompanies me with care and love.

TABLE OF CONTENTS

LIST OF TABLES

LIST OF FIGURES

CHAPTER 1

INTRODUCTION

1.1 Motivation

The high temperature gas-cooled reactor (HTGR) design has been selected for the Next Generation Nuclear Plant (NGNP) project. The helium coolant in the primary circuit has been found to contain low levels of impurities (e.g. CO, CO_2, H_2O, CH_4, and H_2) after steady-state operation. This can lead to an environmental degradation of high temperature alloys used for internals and heat exchangers. Depending on the impurity concentration and the temperature, the materials can undergo oxidation, carburization and decarburization, which can be detrimental to the mechanical behavior of the materials. In addition, the most critical metallic component of the HTGR is the heat exchanger. The materials serve in the temperature range of 760-950^{o}C and withstand coolant pressure up to 7 MPa for a design life of 60 years. This indicated that the assessment of high temperature creep deformation of the materials is of particular importance. Therefore, understanding the environmental effects on the materials and the relevant creep deformation behavior is critical for the design and long-term operation of the HTGR.

1.2 Introduction

Nuclear power is being considered as an energy source to meet growing electricity consumption for sustaining economic growth in the future. Therefore, development of next generation nuclear power plant becomes necessary with higher efficiency, cost effective and safer design. Furthermore, using nuclear power will also decrease the use of limited natural resources while providing a long-lasting source of energy.

Generation IV Nuclear Energy Systems (Gen IV) have been proposed to enhance thermal efficiency, improve nuclear safety, minimize waste and natural resource utilization, and to decrease the cost to build and operate such plants. Over 100 further systems were considered initially; however, with the participation of over 100 experts from Generation IV International Forum (GIF) over 2 year period, the effort ended in December 2002 with the roadmap selecting the six most promising Generation IV systems for worldwide development [1.1]. One of the most promising reactors is Very High Temperature Reactor (VHTR) or High Temperature Gas-Cooled Reactor (HTGR), a helium-cooled thermal spectrum reactor. The system has two main advantages. First, the operating temperature of HTGR is expected to be as high as 1000^{o}C, in order to gain high efficiency energy conversion, over 50%, compared with 33% for the light water reactors (LWRs) currently used. Fig. 1.1 shows the schematic of the original VHTR design proposed in the Generation IV international forum. More recently, the outlet temperature was reduced from 1000^{o}C to 950^{o}C, with slightly decreased power output [1.2]. Furthermore, by taking advantage of high outlet temperature in the HTGR, hydrogen, a clean and green energy source to replace fossil fuels, can be generated through thermal-chemical process [1.3]. Approximately 90% of the HTGR heat will be used to generate electricity and 10% to produce hydrogen.

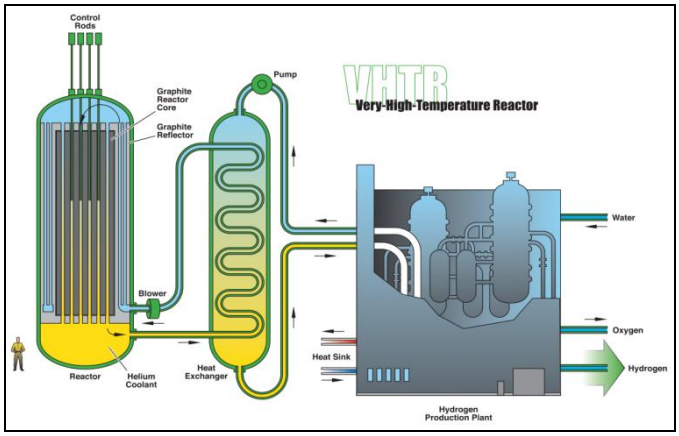

Fig. 1.1: Schematic diagram of the VHTR design [1.1]

Internal core structures and cooling systems, such as the intermediate heat exchanger, the hot gas ducts, process components, and isolation valves are in contact with the hot helium up to about 950^{o}C. The Intermediate Heat Exchanger (IHX) is a major component of the HTGR. This

component will transfer heat to secondary systems that will generate electricity or hydrogen. The thermal, environmental, and service life conditions for the construction of IHX will make selection and qualification of the high-temperature materials a significant challenge.

To qualify the materials, a significant amount of data must be acquired, which includes tensile response, creep resistance, corrosion and creep/fatigue behavior under various corrosive environments. Creep and corrosion are the two main concerns for the HTGR. Creep is the major process controlling the deformation behavior of the materials used at high temperatures. Understanding creep properties of the materials requires long-term testing in order to predict allowable creep strains within the design life of the materials used in the HTGR. In addition, corrosive environments due to active impurities in the helium gas coolant may cause oxidation, carburization and decarburization of the materials [1.4-1.6]. Therefore, efforts must be made not only to obtain the creep and rupture data but also to understand the fundamental creep deformation mechanisms and the corrosion behavior of the materials as a basis for the construction of the IHX and other reactor components. Furthermore, it has been suggested that the corrosion issues may be detrimental to the mechanical behavior of the materials [1.7-1.9]. This must also be taken into account.

Fig. 1.2 shows the design limit for some of the potential structural materials for the HTGR, suggesting that Inconel 617 (alloy 617) and Haynes 230 (alloy 230) are the most promising materials for use in the HTGR. Hastelloy XR is a modified version of Hastelloy X, and is currently being used for the Japanese High-Temperature Engineering Test Reactor (HTTR) IHX design. Hastelloy XR is known to have nearly equivalent creep strength compared with Hastelloy X, but it has significantly improved corrosion resistance under the simulated helium environments [1.11]. However, inferior strength of Hastelloy XR at temperature over 900^{o}C limits the possible application in the HTGR. Incoloy 800H (or alloy 800H) is the only iron based material among the candidate alloys. The approved temperature for alloy 800H for nuclear application is 760 ℃. Even though the allowable temperature is lower compared to other nickel based alloys, alloy 800H is still being considered as a structural material for some components with lower operation temperature, e.g., the secondary heat exchanger in two stage design of the IHX [1.12]. Alloy 800HT is similar to alloy 800H with restricted carbon and larger grain size due to higher annealing temperature, offering higher creep strength.

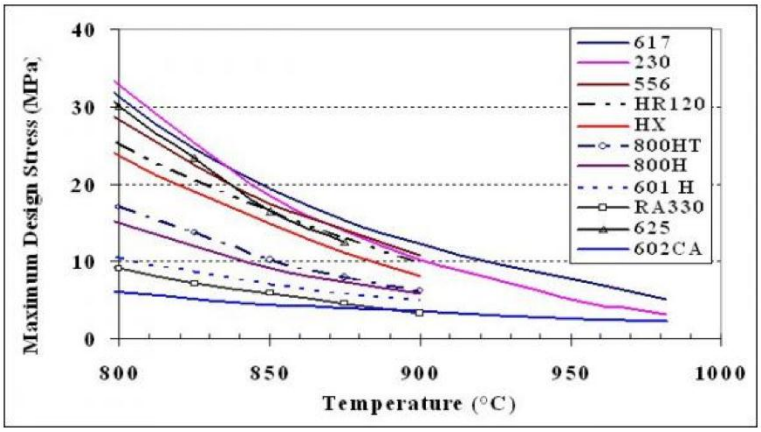

Fig. 1.2: Maximum design limit from ASME VIII I (2006) [1.10]

Alloy 617 and alloy 230 are considered as primary candidate materials for service in the HTGR, due to its exceptional combination of high temperature strength and oxidation resistance [1.12,1.13]. Alloy 617 is a solid-solution, strengthened, nickel-chromium alloy with further alloying additions of cobalt, molybdenum, and aluminum. The high nickel and chromium contents make the alloy resistant to a variety of both reducing and oxidizing media. Solid-solution strengthening is imparted by the cobalt and molybdenum and precipitate hardening is due to formation of $M_{23}C_6$ carbides. Grain boundary carbide mitigate grain boundary sliding and impart resistance to creep deformation. It has been found that, after long-time exposure at high temperature, the alloy retains toughness. No embrittling phase, such as sigma, mu, or laves is formed [1.14,1.15]. Alloy 230 is a relatively new solid-solution strengthened Ni-Cr-W alloy introduced in the early 1980s [1.16]. The addition of tungsten can produce relatively low stacking energy, and formation of tungsten-rich M_6C carbide can pin grain boundaries [1.17]. However, limited amount of data available concerning high temperature mechanical properties [1.17] and corrosion behavior of alloy 230 [1.18]. The limiting chemical composition of alloy 617 and alloy 230 is listed in Table 1.1.

Table 1.1: Limiting Chemical Composition, wt%, of alloy 617 and alloy 230

Alloy	Ni	Cr	Co	Mo	Al	C	Fe	Mn
617	44.5 min	20-24	10-15	8-10	0.8-1.5	0.05-0.15	3.0 max	1.0 max
230	Bal.	20-24	5.0 max	1-3	0.2-0.5	0.05-0.15	3.0 max	0.3-1.0
	Si	S	Ti	Cu	B	P	W	La
617	1.0 max	0.015 max	0.6 max	0.5 max	0.006 max	—	—	—
230	0.25-0.75	0.015 max	—	—	0.015 max	0.03 max	13-15	0.005-0.05

1.3 Research Objective

Since alloy 617 and alloy 230 are the leading materials for the construction of IHX, environmental degradation and the resistance to creep damage for both alloys is a major concern for the HTGR. For corrosion issues, due to the complexity of gas atmosphere, the research will focus the exposure of both alloys in oxidizing, reducing and carburizing atmospheres. Creep deformation of the two alloys was studied using biaxial stress states developed utilizing pressurized tube technique. This approach accounts for the creep behavior more closely related to the realistic conditions to which the materials are subject in practice.

The objectives of the research for alloy 617 and alloy 230 include:

(1) to examine biaxial thermal creep properties, especially for deformation mechanism in secondary creep regime and creep fracture mechanism;

(2) to compare the similarities and differences in creep behavior, if any, between biaxial stress state and uniaxial stress state;

(3) to study the surface degradation phenomena and evolution of the microstructure when the two alloys are exposed to oxidizing, reducing and reducing plus carburizing environments.

The first task establishes the material property data, which is important based on design consideration, and develops an understanding of the creep deformation mechanisms and creep damage mechanisms at high temperatures. The second task focuses on the difference between uniaxial stress state and biaxial stress state. The current empirical relation that was used to predict long-term creep rupture life from short-term tests was examined. The third task

investigates corrosion behavior under various environments. Since the operating environments may be reducing but carburizing, the relevant knowledge for the alloys under oxidizing, reducing and reducing plus carburizing environments is necessary. The exposure times included short-term exposures (several hours) and long-term exposures (up to 1512 h). In addition, microstructural characterization techniques including metallography, scanning electron microscope (SEM), energy-dispersive X-ray spectroscopy (EDX), X-ray diffraction (XRD), Focus ion beam (FIB), and Auger electron spectroscopy (AES) were employed. The information produced by the techniques helps correlate the evolution of microstructure with the experimental results obtained. The approach presented above for the course of the present work can help to establish a systematic understanding of high temperature performance of the two alloys subject to creep and corrosion conditions. This also provides a useful database for designers working on the HTGR development program.

CHAPTER 2

BACKGROUND AND LITERATURE

2.1 Creep

2.1.1 Creep phenomenology

When a material component is subjected to constant applied stress at elevated temperature, continuous deformation can occur. This is a particular concern in metals and alloys since this process usually limits the stresses they can carry in service. This time dependent deformation process is known as creep. The temperature for creep is of an at least 0.3 to 0.4 homologous temperatures T/T_m (T_m: absolute melting temperature of the materials). As indicated in Fig.2.1, the creep curve generally exhibits three characteristic regions. In region I, the region of primary creep, the specimen begins to deform relatively quickly; however, the deformation rate eventually decreases to some near constant value. In region II, secondary creep occurs, where the specimen deforms at this near constant rate throughout; the region is often characterized by a "steady state" creep rate. In the third region, the region of tertiary creep, the deformation of the specimen accelerates to relatively high levels until the specimen fails. Also in Fig. 2.1, upon loading, the specimen extends instantaneously by elastic expansion an amount ε_e. Over a period of time, the specimen creeps with an amount ε_c. The total strain accumulation terminates when the specimen fails at a time t_r, a process referred to as creep rupture or stress rupture.

The primary part and the secondary part of the creep curve are frequently described using an empirical relation [2.1]:

$$\varepsilon = \varepsilon_e + \beta\left[1-\exp(-rt)\right] + \dot{\varepsilon}_{II} t \qquad (2.1)$$

In this equation, β describes the additional strain during transient creep, r^{-1} quantifies the transition time between regions I and II, and $\dot{\varepsilon}_{II}$ is the constant creep rate during secondary creep. In addition, the greatest interest in creep behavior of materials has been at temperature greater than $0.5T_m$. In many cases, almost all of the creep deformation occurs in the secondary regime. Therefore, creep characteristics in a steady-state creep rate as a function of materials and operating variables has been of significant interest from the view point of the designer. Typically, in secondary creep, the strain rate $\dot{\varepsilon}_{II}$ depends with a power law on the stress σ and exponentially on the temperature T:

$$\dot{\varepsilon}_{II} = A(\frac{\sigma}{E})^n \exp(-\frac{Q}{RT}) \qquad (2.2)$$

where A is constant, n is stress exponent, σ is external stress, E is elastic modulus of the materials, R is gas constant and Q is an activation energy characterizing the creep process. Eq. (2.2) is also called power-law creep. Creep is a thermally activated process as indicated by the Arrhenius temperature dependence in Eq. (2.2).

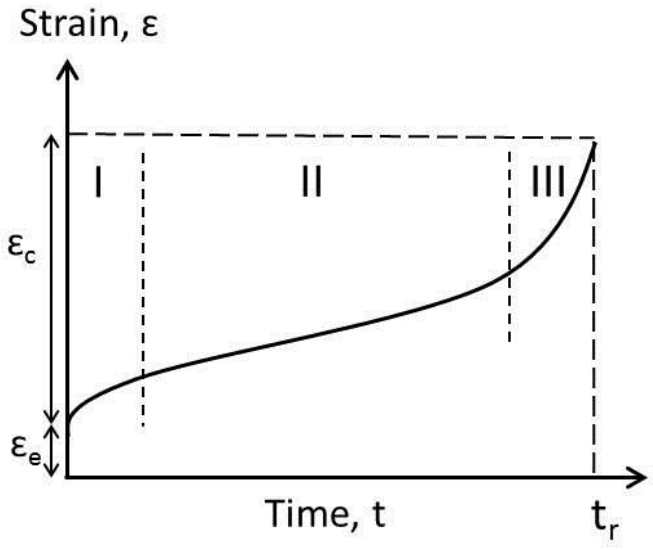

Fig. 2.1: Typical creep strain vs. time

2.1.2 Creep mechanisms

During the primary and secondary creep, it is generally accepted that creep rate is determined by strain hardening rate and recovery softening rate. Assuming the flow stress is a function of time t and strain ε, one can obtain

$$d\sigma = (\frac{\partial \sigma}{\partial t})_{\varepsilon} dt + (\frac{\partial \sigma}{\partial \varepsilon})_{t} d\varepsilon \tag{2.3}$$

Equation (2.3) represents a general form of Baily-Orowan equation [2.2]. This equation can be re-written as the following form:

$$d\sigma = -rdt + hd\varepsilon \tag{2.4}$$

where

$$r = -(\frac{\partial \sigma}{\partial t})_{\varepsilon} \tag{2.5}$$

is the recovery rate under invariant strain and

$$h = (\frac{\partial \sigma}{\partial \varepsilon})_{t} \tag{2.6}$$

is the coefficient of strain hardening where h denotes the change in flow stress σ by $\partial\sigma$ due to an increment in strain ε by $\partial\varepsilon$ over a period of dt at a time point of t. Since the stress remains unchanged during creep, the creep rate in terms of equation (2.4) can be obtained as follows:

$$\dot{\varepsilon} = \frac{r}{h} \tag{2.7}$$

For the primary creep, the decrease in creep rate suggests that strain hardening rate is larger than recovery softening rate, while secondary creep signifies that strain hardening rate is equal to recovery softening rate. For primary creep, in terms of a microstructure point of view, strain hardening may result from dislocation intersection and dislocation pile up at an obstacles. Strain

softening may result from thermally-activated cross slip, rearrangement of dislocations, dynamic recovery, and activation of secondary slip systems.

As discussed in section 2.2.1, microscopic processes in secondary creep regime are of greater interest. According to previous literature, equation 2.2 can be further expanded by the Bird-Mukherjee-Dorn (BMD) equation [2.3]:

$$\frac{\dot{\varepsilon}_{ss} kT}{DEb} = C_o (\frac{\sigma}{E})^n (\frac{b}{d})^r \tag{2.8}$$

where C_o is a constant, $\dot{\varepsilon}_{ss}$ the steady state creep rate, E the elastic modulus, b the Burgers vector, k the Boltzmann constant, T the absolute temperature, σ the applied stress, d the grain diameter, p the inverse grain exponent, n stress exponent, and D the diffusivity which can be described by the following equation:

$$D = D_o \exp(\frac{-Q}{RT}) \tag{2.9}$$

where D_o is the frequency factor, Q the activation energy and R the universal gas constant. Table 2.1 summarizes the constant n, r, and Q. Creep parameters n, r and Q are used to determine the operating creep mechanism. From Table 2.1, climb of edge dislocation, low temperature clime and viscous glide can be generally termed dislocation creep, since the creep rate is related to dislocation movement. The difference lies in the rate-controlling process for the creep rate. Climb of dislocation suggests dislocation can climb over an obstacle by adding or emitting vacancies via lattice diffusion (Q_L) at high temperature. At low temperature, diffusion of vacancies along dislocation core (Q_B) is important, called “Low temperature climb”. Viscous glide suggests that climb of dislocation through diffusion is no longer rate-controlling step whereas glide of dislocation is a rate-determining step. The mechanism for viscous glide is related to interaction of solute atoms with dislocations (Qs) as glide of dislocations proceeds [2.4]. Nabarro-Herring and Coble creep can be generally termed diffusional creep, where vacancy diffusion produces directly deformation and occurs at low stress regime compared with dislocation creep. It is noted that the common point for the two mechanisms is the stress exponent is unity. The difference for the two mechanisms is that Nabarro-Herring creep occurs at high temperature through lattice diffusion (Q_L) whereas Coble creep occurs at intermediate

temperature through grain boundary diffusion (Q_B). Table 2.1 shows that grain diameter is significantly influence creep rate as Coble creep dominates. Grain boundary sliding (GBS) is important as materials exhibits superplasticity. GBS is not an independent process and is usually accommodated by diffusional creep at high temperatures (Q_B). Harper-Dorn creep via lattice diffusion (Q_L) has been only observed in high purity materials with large grain size (e.g. pure lead with grain size of 1 mm) [2.5].

Most materials used in high temperatures are second phase particle strengthened alloys. Therefore, some characteristics of creep deformation may be slightly different from pure metals and simple solid-solution alloys. These alloys usually exhibit much lower creep rate than that without second phase particles. Activation energy can be much higher than that for self-diffusion. The stress exponent, n, can be as high as 10-40. Due to high stress exponent, a threshold stress below which creep rate cannot occur is observed. Therefore, the BMD equation is further modified by taking into account the threshold stress, as follows [2.6]:

$$\frac{\dot{\varepsilon}_{ss} kT}{DEb} = C_o \left(\frac{\sigma - \sigma_{th}}{E}\right)^n \left(\frac{b}{d}\right)^r \qquad (2.10)$$

where σ_{th} is the threshold stress. This equation suggests that the effective stress, ($\sigma - \sigma_{th}$), actually controls the creep mechanism instead of applied stress [2.7].

A convenient way to illustrate the deformation mechanisms which can occur within a particular metal or alloy can be shown in a deformation mechanism map. The maps are usually presented as normalized shear stress versus homologous temperature with lines of constant strain rate drawn within the particular fields of dominance. The advantage of these maps allows us to obtain a considerable amount of information to be presented in a compact and visual fashion. An example of one such map is pure nickel, as can be seen in Fig.2.2. From this example, it is easily shown that dislocation-based creep begins above 0.2 T_m and above 10^{-4} σ_s/μ depending on strain rate. Although many maps are available for pure metals and many commercially important alloys, it should be pointed out that the degree of accuracy depends strongly on the quality of the experimental data and the choice of theoretical equations from which the map is constructed. However, no map can be found for alloy 617 and alloy 230.

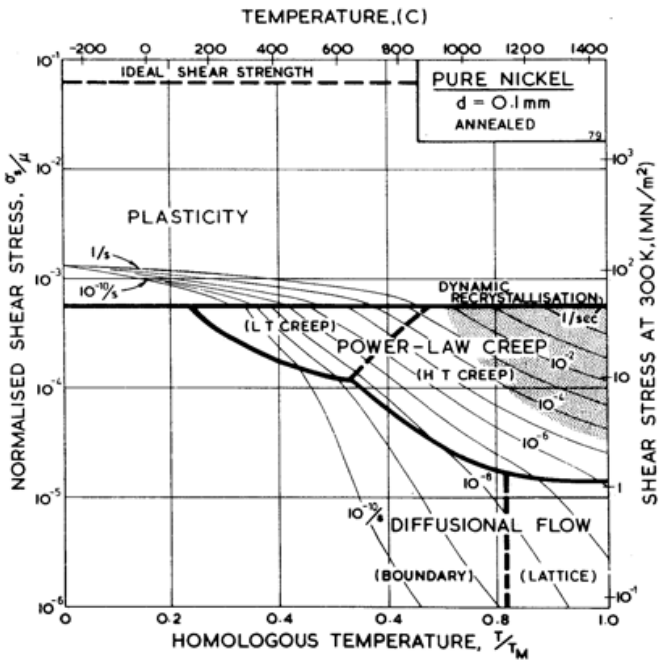

Fig. 2.2: Deformation map for 0.1mm grain-size nickel. Isostrain line superimposed on the map. [2.8]

Table 2.1: Parametric dependencies of different creep mechanisms [2.6]

Mechanism	n	r	Q
Climb of Edge dislocation	5	0	Q_L
Low Temperature Climb	7	0	Q_C
Viscous Glide	3	0	Q_S
Grain Boundary Sliding (Super plasticity)	2	2	Q_B
Nabarro-Herring	1	2	Q_L
Coble	1	3	Q_B
Harper-Dorn	1	0	Q_L

Type of activation energies: lattice diffusion (Q_L), dislocation core diffusion (Q_C), solution atom diffusion (Q_S), grain boundary diffusion (Q_B)

2.1.3 Creep Rupture

After sufficiently long loading times, the creep deformation occurring at high temperatures always give rise to fracture of the materials. The strain rate, which attained its minimum value during secondary creep, increases again in the tertiary stage of creep. This processes ends with failure, so-called creep rupture. Creep rupture can be regarded as the end result of the creep damage accumulation, a degradation process that is responsible for the increased creep strain rates in the stage III creep. There are two types of fracture that can occur in materials. In a typical condition (low stress and high temperatures), nucleation, growth and coalescence of creep voids along grain boundaries is usually the major failure process. Fig. 2.3 (a) shows this type of creep fracture. At a high stress condition, intergranular wedge cracks form as a result of grain boundary sliding at triple points, shown schematically in Fig. 2.3 (b). The formation of intergranular cavities usually forms at stress concentrations (e.g. grain corners) and at various irregularties along grain boundaries. These stresses cause decohesion locally and cavities are thereby initiated. Other sites for favoring the cavities formation may be precipitates on the grain boundaries or dislocation pile-up. For instance, in nickel superalloys, cavities nucleate at grain-boundary $M_{23}C_6$-carbides, especially at the junction with a slip band impinging on the particle. For intergranular wedge cracks, there is a large stress concentration that can cause failure of the grain boundaries if their cleavage strength is exceeded. Accordingly, this type of cracks tends to form at higher stresses.

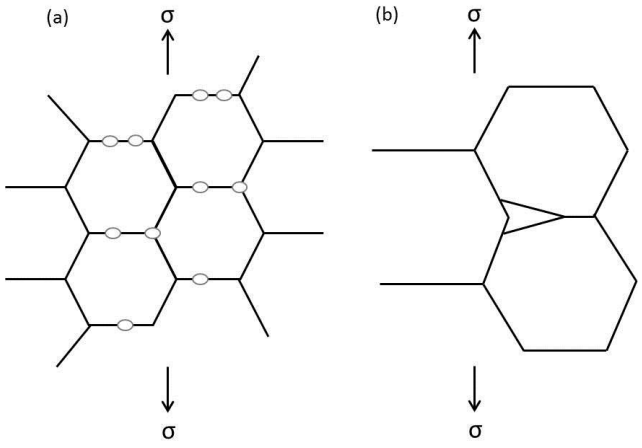

Fig. 2.3: Schematic illustration of creep fractures

2.1.4 Creep behavior of alloy 617 and alloy 230

It has been shown [2.9] that the creep curve of alloy 617 follows a classical behavior at 850^{o}C; however, no recognizable secondary creep regime was observed at 950^{o}C. Recently, Roy et al. [2.10] found that with increasing applied stress levels and temperature, the steady-state region became shorter and finally disappeared at 950^{o}C, showing only a steeper tertiary creep curve. However, in a study by Chomette [2.11], non-classical creep behavior at 850 and 950^{o}C were observed, with a strain rate drop at the beginning of the tests followed by a creep rate increase to a plateau before the onset of the tertiary creep. Since the creep rate is related to the microstructure of the materials, the information produced by microstructure examination is necessary. Microstructure examination of the crept alloy 617 showed that the intragranular carbides are effective in lowering creep rate, and the unstable intragranular carbides redissolve in favor of the more stable grain boundary carbides at 1000^{o}C [2.12]. More recently, it has been found that in a creep-deformation environment, carbides observed in alloy 617 may dissolve and reprecipitate on boundaries in tension [2.12,2.13]. It was believed that the difference in the stability of the carbides in compressive vs tensile environments is the driving force for the distribution [2.12]. Schlegel et al. [2.13] studied the location of the carbides, grain boundary character, and precipitate type and concluded that the carbides distribution is mainly influenced by grain boundary characters. To understand the deformation mechanism of alloy 617 in secondary creep regime, Fig. 2.4 summarizes the stress exponents based on different independent studies. It can be seen that about the temperature range from 850 to 950^{o}C, the stress exponent, n, is larger than unity even as the stress can be as low as 20 MPa at 950^{o}C. This indicated that deformation is related to dislocation movement (or dislocation creep). However, very limited amount of data published for alloy 230 and therefore, deformation mechanism is not fully understood up to now.

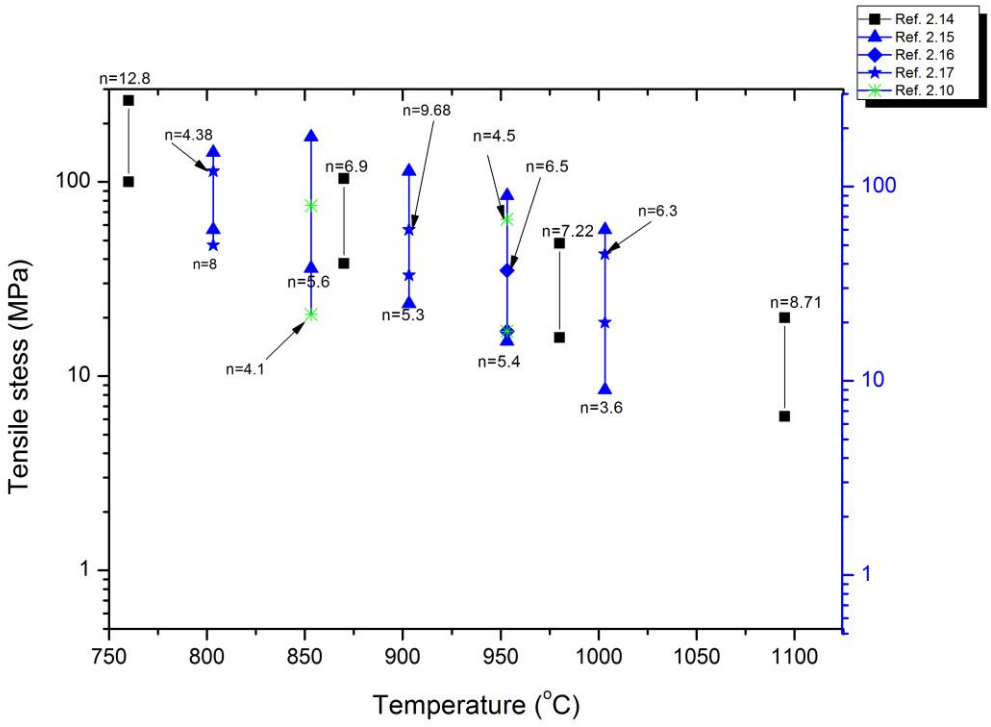

Fig. 2.4: Stress exponent of alloy 617 for different stresses at various temperatures [2.10,2.14-2.17].

2.2 Environmental Issues

2.2.1 Gas chemistry in the HTGR

In the HTGR, helium is the coolant gas of choice because of its chemical inertness and stability at very high temperatures. Although helium is nominally pure, there are, inevitably, impurities at the parts per million by volume (ppm) levels in the coolant during operation of the HTGR. These impurities coming from gas reactions with the graphite in the nuclear reactor core include CO, CO_2, H_2O, CH_4, and H_2. It is noted that some of the H_2 could be due to the diffusion of H_2 from the process plant into the primary coolant circuit [2.18]. Table 2.2 shows the impurity levels reported for steady state operation. As shown in the Table, these impurities are of similar levels. Although their concentrations are quite low, these elements are very reactive toward metallic surface at high temperatures. It is crucial to understand the interplay between the alloy

surface, temperature, and gas composition to determine whether corrosive oxidation, carburization, or decarburization occurs. The corrosion mechanisms of carburization and decarburization are of particular importance to the mechanical stability of the metal alloys. Carburization is related to lower temperature embrittlement [2.19] while decarburization is associated with reduced creep rupture strength [2.20]. Therefore, a continuous self-healing, passivating oxide layer is needed to establish the most corrosion-resistance alloy. In the cases of alloy 617 and alloy 230, it has been suggested [2.21] that surface chromia formed within slight oxidizing environment may act as an effective barrier to minimize environmental degradation of the materials in the HTGR environment and reduce negative synergistic effects which could degrade mechanical properties (e.g. tensile and creep) under these conditions. Understanding the oxidation characteristics and stability of surface chromia for the two alloys are of major significance for determining service life and possible failure modes..

Due to the complexity of gas-metal reaction, a simplistic breakdown of the environmental response of alloy 617 and alloy 230 at various gas concentrations and temperatures can be portrayed in Fig. 2.5. There are five zones where strongly reducing (I), highly oxidizing (II), stable external oxide with stable internal carbide (III), strongly carburizing internally and externally (IV), and strong external carburization with stable oxide layer (IVa) can be differentiated [2.22]. The carbon activity and oxygen partial pressure in the environments mainly determines corrosion behavior of the alloys. During the steady-state operation of HTGR, the materials are expected to be in gas composition of zone III [2.22].

Table 2.2: Impurities reported in the helium coolant during steady-state operation of HTGR (in ppm) [2.23-2.26].

	H_2O	H_2	CO	CO_2	CH_4	O_2	N_2
Peach Bottom	0.5	10	0.5	<0.05	1	–	0.5
Fort St. Vrain	1	7	3	1	0.1	–	–
AVR	0.15	9	45	0.25	1	–	22
Dragon	0.1	0.1	0.05	0.02	0.1	0.1	0.05
THTR	<0.01	0.8	0.4	0.2	0.1	–	0.1

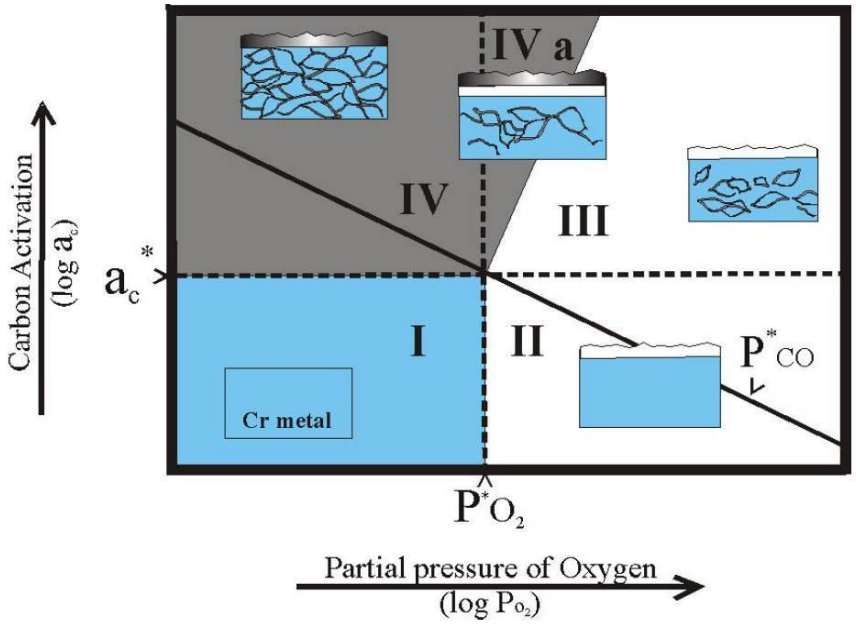

Fig. 2.5: Stability diagram of different corrosion zone depending on oxygen partial pressure (pO_2) and carbon activity (a_c). Zone III is preferred gas environment for materials used in HTGR [2.22].

2.2.2 High temperature oxidation

Since the alloys used in the HTGR are expected to operate in zone III, and therefore, an understanding of the basic principles of high temperature oxidation, particular in this region, is necessary. For alloys exposed to air at high temperatures, the formation of an oxide scale on the surface usually observed. The mechanism of oxidation depends on the nature of the scale (e.g. solid, liquid, or partial evaporation). If solid scales formed, oxidation kinetics also depends on whether the scales are compact or porous. It is well-known that if a compact scale is formed, the rate of oxidation will depend on the solid-state diffusion (e.g. lattice, grain boundary, or short-circuit diffusion) through the compact scale. It will also depend on whether the diffusion is controlled on the metal side or the oxygen side, or if both diffusion processes occur simultaneously, even if the rates are different. As the oxide scale grows, the diffusion distance increases, and therefore, decreases the oxidation rate. A compact scale provides the desired

protective properties, and practically, it is the most important feature of oxidation. To improve the oxidation resistance of alloys, the goal is to improve protective properties of the scales.

To understand oxidation behavior of a compact scale (e.g. Cr_2O_3), the most important contribution has been given by Wagner [2.27] in his theory concerning high temperature parabolic oxidation. The assumptions of his theory are listed below [2.27]:

(1) The oxide layer is a compact, perfectly adherent scale;

(2) The rate-determining step is controlled by migration of ions or electrons across the scale;

(3) Thermodynamic equilibrium is established at both the metal–scale and scale–gas interfaces;

(4) The deviations from stoichiometry of the scale is small, and hence, the position dependence of ionic fluxes is neglected;

(5) Oxygen solubility in the metal may be neglected.

The detailed derivation of the reaction rate can be found elsewhere [2.27]. In evaluation experimental results, the parabolic rate constant is usually expressed in the following equation:

$$x^2 = k_p * t \qquad (2.11)$$

where t is time (sec), and x can be measured in terms of oxide thickness (cm) and k_p is accordingly expressed in units of square centimeter per second. If the weight change is measured, x is expressed in term of gram per unit area and k_p is $g^2/cm^4/sec$.

For high-temperature alloys, selective oxidation occurs due to the oxides of the alloying elements showing large differences in stability. Other factors affecting the occurrence of selective oxidation includes the type of alloying addition, the concentration of the active alloying component, the temperature and on the partial pressure of oxygen. A typical high temperature alloy is Ni-Cr alloys, a simple model alloy for basic understanding at high temperature oxidation. Extensive studies have been conducted on the system [2.28,2.29]. Due to its high chromium concentration, a protective Cr_2O_3 layer is formed on the alloy surface [2.28,2.29].

Several studies have been carried out on the high temperature oxidation of alloy 617 [2.30-2.32]. It was reported [2.31] that for oxidation in air for 1000 hr, the oxide layer typically consists of a continuous, dense Cr_2O_3 film and small amounts of (Ni,Co)O oxide mixture covering the chromia. More recently, Kim et al. [2.32] found that oxidizing alloy 617 in air at 900^oC for 1000 h results in the formation of a double oxide layer: an outer NiO layer and an

inner Cr_2O_3 layer. For alloy 230, in a study by Jian et al. [2.33], multi-stage oxidation kinetics was observed at temperatures ranging from 650 to 850^{o}C and it was found that two oxide phases (Cr_2O_3 and $MnCr_2O_4$) were formed. England et al. [2.34] reported that the selective oxidation of Mn occurred in thin foil of alloy 230. More recently, it was suggested [2.32] that $MnCr_2O_4$ was formed on top of Cr_2O_3 layer for alloy 230 oxidized up to 1000 h at 900^{o}C. These results indicated that the oxidation kinetics and the resulting microstructure of oxide phase for alloy 617 and alloy 230 exposed at high temperatures are complicated. It is necessary to establish a systematic study concerning the oxidation behavior and the resulting microstructure for both alloys.

2.2.3 Growth mechanism of Cr_2O_3 scale during oxidation

Oxidation resistance of Cr-rich alloys is in practice provided by forming a dense, protective layer of Cr_2O_3. Therefore, the growing mechanism has been considerable of interest and much research was conducted. In a study by Caplan et al. [2.35], they found that chromium outward diffusion occurs as the scale is mono-crystal oxide whereas both chromium outward diffusion and oxygen inward diffusion along grain boundaries occurs in polycrystalline Cr_2O_3. Oxidation of pure chromium, Skeldon et al. [2.36] using isotope tracer technique also confirmed the outward diffusion of chromium during initial growth of the oxide and later mechanism changed due to new oxide formed within the outer part of oxide. They also suggested [2.36] that oxygen was transported through grain boundaries but the oxide formation via chromium outward diffusion was predominant. Past studies [2.37,2.38] using oxygen-18 tracer techniques indicated that the diffusion process depends on the oxidation temperature. Those studies reported [2.39] that at 850^{o}C, cation outward diffusion is significant while at 950^{o}C, some inward diffusion of oxygen also occurs, most likely along grain boundaries. In a recent study by Zurek et al. [2.40], the growth of the chromia scale was predominantly by chromium outward diffusion. Those findings indicated that the chromium scale growth mainly results from Cr outward diffusion, while oxygen transport does occur, mainly along grain boundaries and accordingly oxide formation takes place along grain boundaries.

2.2.4 Development of residual stress of the growing oxide scale

Residual stresses in the oxide layer are another issue to be considered. It is known that the presence of residual stress in the scale may cause cracking and/or spallation of the protective oxide layer, thereby decreasing the oxidation resistance of the material. Although the detailed mechanisms of the residual stress generated in the oxide layer during oxidation are not entirely understood, it is believed that several factors may play a role in the development of the residual stresses: those associated with epitaxial stresses [2.41], volume differences between the oxide and the substrate [2.42], point defect stresses, and the formation of new or alternate oxides within a scale [2.43]. Epitaxial stress comes from difference in lattice parameter between the oxide and the substrate. The stress generated seems to play an important role as the scale is very thin. The volume differences between the oxide and the substrate result from the fact that in most cases, the specific volume of the oxide is not the same as that of the metal which is consumed in its formation. The Pilling–Bedworth ratio (PBR) [2.42] was proposed to determine the sign of the stress:

$$PBR = \frac{V_{scale}}{V_{metal}} \tag{2.12}$$

The oxide is expected to be in compression if the PBR is greater than unity. This ratio is also proposed to determine the magnitude of the stress and the likelihood for spallation or non-protection based on the differences in the respective volumes of the oxide and matrix.

For the stress developed in the oxide scale grown on high temperature alloys, the magnitudes of residual stresses were reported to be −1.3 GPa to −2.6 GPa for chromia formed on Ni–30Cr [2.44]. For chromia formed on Haynes alloy 230 under various oxidizing conditions, the residual stresses ranged from −1.2 to −1.8 GPa [2.45]. These results indicated that the stress state is highly compressive.

2.2.5 Metal-gas interaction in simulated HTGR environments

As can be seen from Table 2.2, the oxygen concentration is extremely low and the presence of CO, CO_2, H_2O and CH_4 may cause a carburization/decarburization phenomenon. Therefore,

metal/gas interface reactions in impure helium where carburizing gases are present are important.. A series of paper by Brenner et al. [2.46-2.48], Quadakkers et al. [2.49,2.50] and Christ et al. [2.51] described these reactions and the corrosion behavior of Ni-Cr alloys can be expressed by five competing reactions which occur simultaneously on the metallic surface. Assuming that Cr is the main element that forms oxide and carbides in the alloy:

Oxidation by water vapor and carbon dioxide

$$2Cr_{solution} + 3H_2O \rightarrow Cr_2O_3 + 3H_2 \quad (2.13)$$

$$2Cr_{solution} + 3CO_2 \rightarrow Cr_2O_3 + 3CO \quad (2.14)$$

Decarburization by water vapor and carbon dioxide

$$H_2O + 3C_{solution} \rightarrow CO_{(g)} + H_2 \quad (2.15)$$

Carburization by methane

$$7C_{solution} + 3CH_4 \rightarrow Cr_7C_3 + 6H_2 \quad (2.16)$$

It is noted that water vapor and carbon dioxide can oxidize Cr and promote to form surface Cr_2O_3, leading to a protective layer on the alloy. Also note that methane can thermally crack at high temperature, forming carbides within materials.

Oxidation by CO

$$9Cr_{solution} + 3CO \rightarrow Cr_2O_3 + C_{solution} \quad (2.17)$$

The direction of equation (2.17) depends on the temperature. Cabet et al. [2.52] suggested that there is a critical temperature, T_A, above which the chromia becomes unstable, and equation (2.17) proceeds towards to the left. They also suggested that T_A is a function of the partial pressure of CO, P(CO). Fig. 2.6 shows the stability of chromia based on T_A and P(CO).

On the basis of the equation above and the stability diagram shown in Fig. 2.5, the concentration of H_2O, CH_4, and CO plays an important role in determining the corrosion behavior of the alloys. It is noted that in the reactor systems, where the flow rate could be high, the non-equilibrium thermodynamics should also be considered. In addition, the pressure of the

reactor system may be up to 7 MPa which may affect the calculation of carbon activity and oxygen partial pressure.

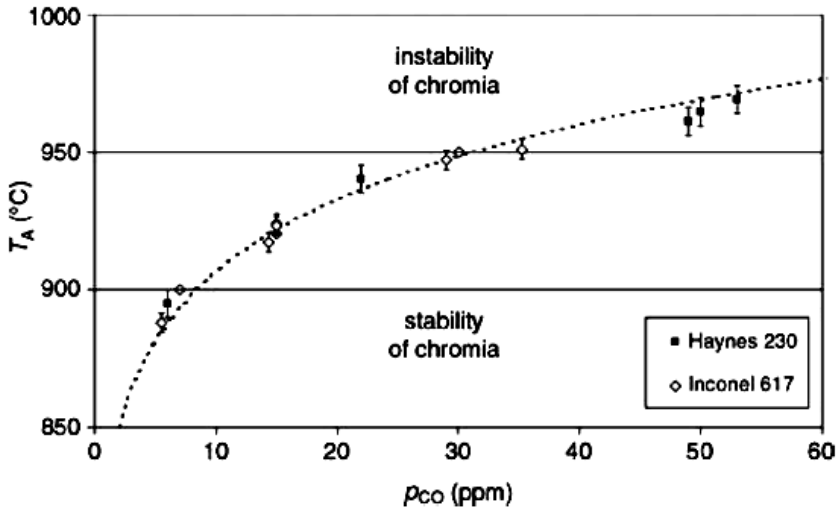

Fig. 2.6: Stability of chromia as a function of critical temperature T_A and partial pressure of CO [2.52].

CHAPTER 3

EXPERIMENTAL APPROACH

3.1 Corrosion Tests

Alloy 617 and alloy 230 were supplied by Haynes International, as 1 inch and 1.5 inch thick plates, which were hot worked and solution treated at 1177^{o}C for 37 min, and 1191^{o}C for 3 hours, respectively. (Heat Number: 861758808 for alloy 617; and 830587801 for alloy 230) The chemical compositions are shown in Table 3.1. Coupons of 10 mm x 15 mm x 1mm were prepared from the as-received material, and were polished down to a 600 grit SiC paper, followed by an ultrasonic cleaning process, which used acetone and ethanol and then dried in a vacuum dryer. After long-term exposure, the weight was measured before and after exposure by a micro-balance with accuracy of 1μg.

High temperature corrosion exposures were carried out in three types of atmospheres. Tables 3.2 and 3.3 shows both short-term and long-term exposure conditions, respectively. The air environment provides oxidation behavior, He+5% H_2 produces a low oxygen partial pressure (low-pO_2) atmosphere, and He+5%H_2+1%CH_4 generates a carburizing environment.

For short-term exposures, the Cahn Thermax 500 Thermogravimetric Analyzer (TGA), manufactured by Thermo Fisher Scientific Inc., was employed to study in-situ corrosion behavior. Fig. 3.1 shows the TGA diagram and a photograph of the system used in the study. The accuracy of the balance was 1μg. The samples were heated in air with a tube furnace at 850, 900, 950 and 1000^{o}C, respectively. The heating rate was 25^{o}C/min. The weight change was monitored over the entire exposure period with measurements every second. The flow rate of each gas was 90 standard cubic centimeter per minute (SCCM).

Long-term exposures were conducted in a high temperature tube furnace, as shown in Fig. 3.2. The specimens were placed in the middle of the furnace where the uniform temperature existed. Prior to the exposures, the furnace was sealed and evacuated via a mechanical pump, and

then the gas used for the corrosive exposure was purged into the furnace. This procedure was repeated three times. The flow rate of the gas was 90 SCCM and the furnace was heated to 950^{o}C with a heating rate of 10^{o}C/min. After a period of exposure time, the furnace was cooled down and then one of the specimens was taken out. The above procedure was repeated until all the experiments were finished. Each specimen was weighted before and after the exposure and then the corresponding weight change can be recorded. The weight was measured by microbalance. The accuracy of the microbalance was 1μg.

Table 3.1: Chemical Composition of alloy 617 and alloy 230 in wt% for thick plate

Alloy	Al	B	C	Co	Cr	Cu	Fe	La
617	1.03	<0.002	0.08	12.2	22.1	0.017	1.104	-
230	0.38	0.004	0.11	0.29	21.7	0.04	1.4	0.014
	Mn	Mo	Ni	P	S	Si	Ti	W
617	0.064	9.46	52.86	0.002	<0.002	0.05	0.39	-
230	0.46	1.75	BAL	0.005	<0.002	0.4	<0.01	13.89

Table 3.2: Experimental conditions for short-term exposures

Materials	Temperature (^{o}C)	Controlled Environments	exposure time
Alloy 617	850, 900, 950, 1000	air, He + 5%H_2 , He + 5%H_2 + 1%CH_4	several hours
Alloy 230			

Table 3.3: Experimental conditions for long-term exposures

Materials	Temperature (^{o}C)	Controlled Environments	exposure time
Alloy 617	850, 950	air, He + 5%H_2	up to 1512 hr
Alloy 230			

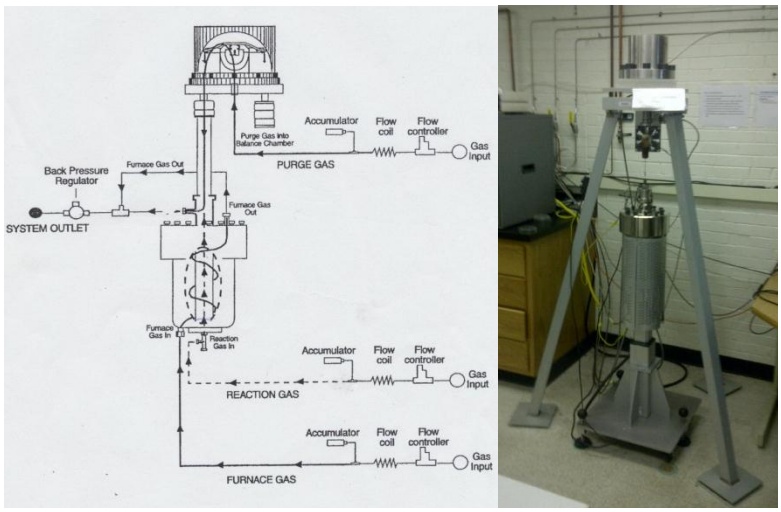

Fig. 3.1: Schematic diagram and a photograph of the TGA used in the short-term exposures.

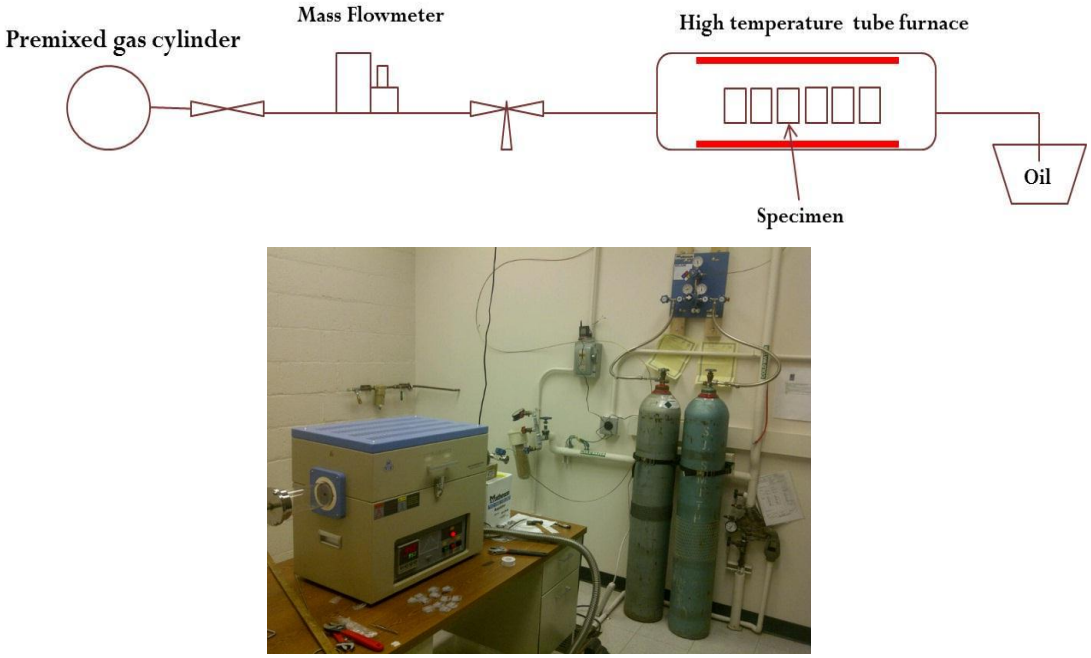

Fig. 3.2: A schematic illustration for long term exposures and a photograph for the experimental setup used in the long-term exposures.

3.2 Creep Tests

Tube specimens of alloy 617 and alloy 230 were produced by Century Tubes Inc. The composition of the two materials is given in the Table 3.4 with a certified test report of heat number: XX58A7UK for alloy 617 and 8305-8-7171 for alloy 230.

The specimens used in the study are compact and rely only on internal pressure. The dimensions of the creep specimen and the photograph of the specimen are shown in Fig.3.3. Using electron beam welding technique, the specimens were sealed by two end caps with a small hole drilled on one of the two end caps. Before pressurizing the specimen, the specimen was pumped down by a mechanical pump. Then the furnace was heated up to the working temperature and then the specimen was put into the middle of the furnace. Then high purity argon gas was used to pressurize the specimen. The use of argon can avoid oxidation of inner wall. A pressure gauge was used to monitor the pressure in the tube. Fig. 3.4 shows the schematic diagram of the system. After a period of time, the specimen was taken out and then the gas inside the specimen was released. The diameter change of the specimen was measured using a laser scanner, the resolution of which is $0.5\,\mu m$. Fig. 3.5 shows the schematic diagram and photograph of the laser instrument used in the present study. Table 3.5 and 3.6 lists the experimental conditions for alloy 617 and alloy 230, respectively. The stresses indicated in Table 3.4 are the mid-wall effective stresses based on von Mises criterion, converted by the following equations [3.1]:

$$\sigma_h = \frac{pR_i^2}{R_0^2 - R_i^2}\left[1 + \frac{R_0^2}{R_m^2}\right] \tag{3.1}$$

$$S = \frac{\sqrt{3}R_0^2}{R_0^2 + R_m^2}\sigma_h \tag{3.2}$$

where R_i : inner radius, R_o: outside radius, R_m: mid-wall radius, p: internal gas pressure, σ_h: mid-wall hoop stress, and S is mid-wall effective stress. The diameter strain can be calculated by the following equations:

$$\varepsilon_{dia} = \frac{\Delta D}{D_0} \tag{3.3}$$

where D_0: original diameter, ΔD: diameter change, and ε_{dia}: diameter strain. To examine the microstructure change during the secondary creep, an interrupted test was conducted for alloy 230 at 950°C under the applied stress of 12 MPa.

Table 3.4: Chemical Composition of alloy 617 and alloy 230 in wt% for tube specimens

Alloy	Al	B	C	Co	Cr	Cu	Fe	P
617	1.04	0.02	0.08	12.46	22.21	0.14	1.55	–
230	0.37	0.03	0.11	0.19	22.39	–	0.94	0.008
	Mn	Mo	Ni	S	Si	Ti	W	La
617	0.07	8.97	53.02	0.01	0.17	0.29	–	–
230	0.5	1.36	BAL	0.02	0.38	0.01	14.26	–

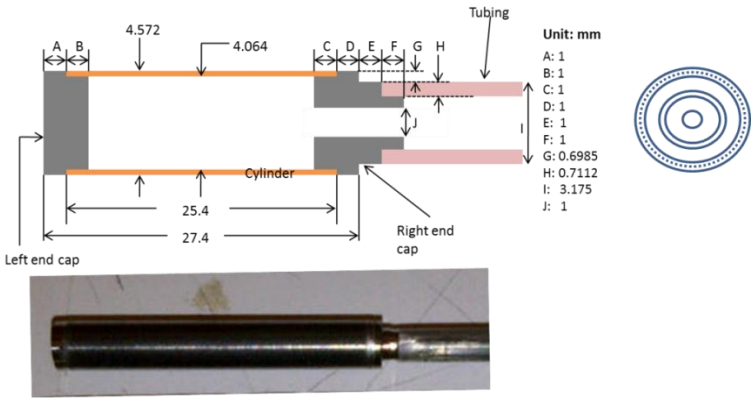

Fig. 3.3: Schematic diagram and photograph of the pressurized creep tube.

Fig. 3.4: The schematic diagram of creep tube testing performed at high temperatures.

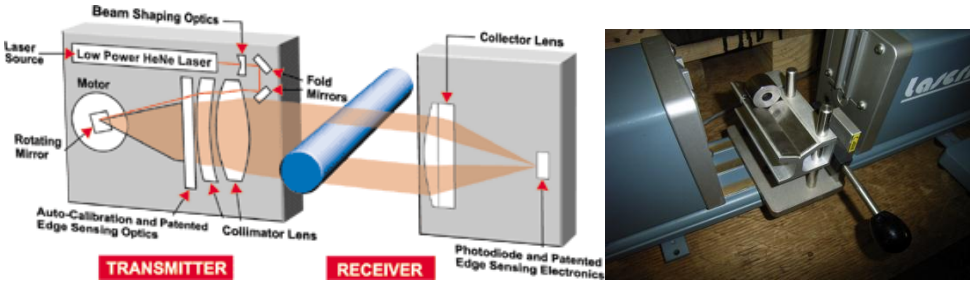

Fig. 3.5: Laser instrument used to measure the diameter change of the tube specimen. The resolution is 0.5 μm. [3.2]

Table 3.5: Experimental conditions of alloy 617 for creep testing

Temperature (^{o}C)	Internal pressure (MPa)	Stress, S (MPa)	creep rupture time
950	4.38, 3.15, 2.46, 2.05, 1.37	32 ,23, 18, 15, 10	up to 1000 hr
850	7.52, 6.16, 4.79, 3.42	55, 45, 35, 25	

Table 3.6: Experimental conditions of alloy 230 for creep testing

Temperature (^{o}C)	Internal pressure (MPa)	Stress, S (MPa)	creep rupture time
950	3.15, 2.46, 2.05, 1.6	23, 18, 15, 12	up to 1000 hr
850	6.16, 5.47, 5.13, 4.79	45, 40, 37.5, 35	

3.3 Material Characterization

To characterize the corroded layer, microstructural analysis was carried out in the Frederick Seitz Materials Research Laboratory (FS-MRL). For corrosion tests, phase identification of the oxide scale grown on the substrate was characterized by X-ray diffraction (XRD) and Grain incident X-ray diffraction (GIXRD) with theta-2 theta scan and an incident angle of 2° 4° and 6° (X'Pert MRD Pro, PANalytical), respectively. Surface morphology was characterized by scanning electron microscopy (JEOL 7000F SEM). Cross-sectional view of the oxide was

examined by focus ion beam (FIB, FEI Strata™ DB235), which is a dual beam system combing a scanning electron microscope (SEM) and a focused ion beam (FIB) with gallium metal ion beam source for cutting. The compositional depth profiles of the oxide scale/substrate specimens were determined by Auger electron spectroscopy (AES, model PHI 660 from Physical Electronics). The residual stresses of the Cr_2O_3 and the substrate were determined by modified sin2φ method using a four-circle diffractometer with psi-goniometer geometry [3.3]. In order to increase the diffraction volume of the oxide scale, an incidence grazing angle of 2° was used for the Cr_2O_3 oxide phase and the substrate. The (116) peak of the Cr_2O_3 was used for the residual stress measurement because it provided sufficient intensity for precise determination of the peak position. For the substrate, the diffraction peak of (220) was used. Using this method, the residual stresses of the substrate near the scale/substrate interface can be obtained. One additional specimen exposed at 950^{o}C in the reducing environment was surrounded by a quartz tube of 15 mm diameter. The quartz tube was treated with 1.5 mL concentration of HNO_3 for a full week. Then the solution was filtered and diluted to 10 mL with water, and analyzed using inductively coupled plasma mass spectrometry (ICP-ME) with detection limit of 10 parts per trillion (ppt). The analysis provided a determination of the residual elements deposited on the quartz tube which were released from the alloy during exposure. In order to obtain the oxygen partial pressure in the He + 5% H_2 environment, a LINDBERG high-temperature tube furnace coupled with a zirconia oxygen gauge (15% CaO-doped ZrO_2) was used. The procedures for the oxygen partial pressure measurements were described elsewhere [3.4]. The specimens exposed to the carburizing environment were cut, polished and etched using 15 ml HCl, 10 ml acetic and 10 ml HNO_3. Using SEM, carburization depth can be determined. To examine the composition of surface carbides produced in the carburizing environment, X-ray diffraction and X-ray photoelectron spectroscopy (XPS) was used.

For creep tests, cross-sectional surface was cut using a low-speed diamond saw machine, and then polished and etched using 15 ml HCl, 10 ml acetic and 10 ml HNO_3. The etching time for alloy 617 and for alloy 230 was about 180 and 270 sec, respectively. The specimen surface was examined by SEM. Before the creep tests, as-received cross-sectional view and side view (longitudinal direction) of metallic surface for both alloys was also examined. This is shown in Fig. 3.6 and 3.7 for alloy 617 and alloy 230, respectively.

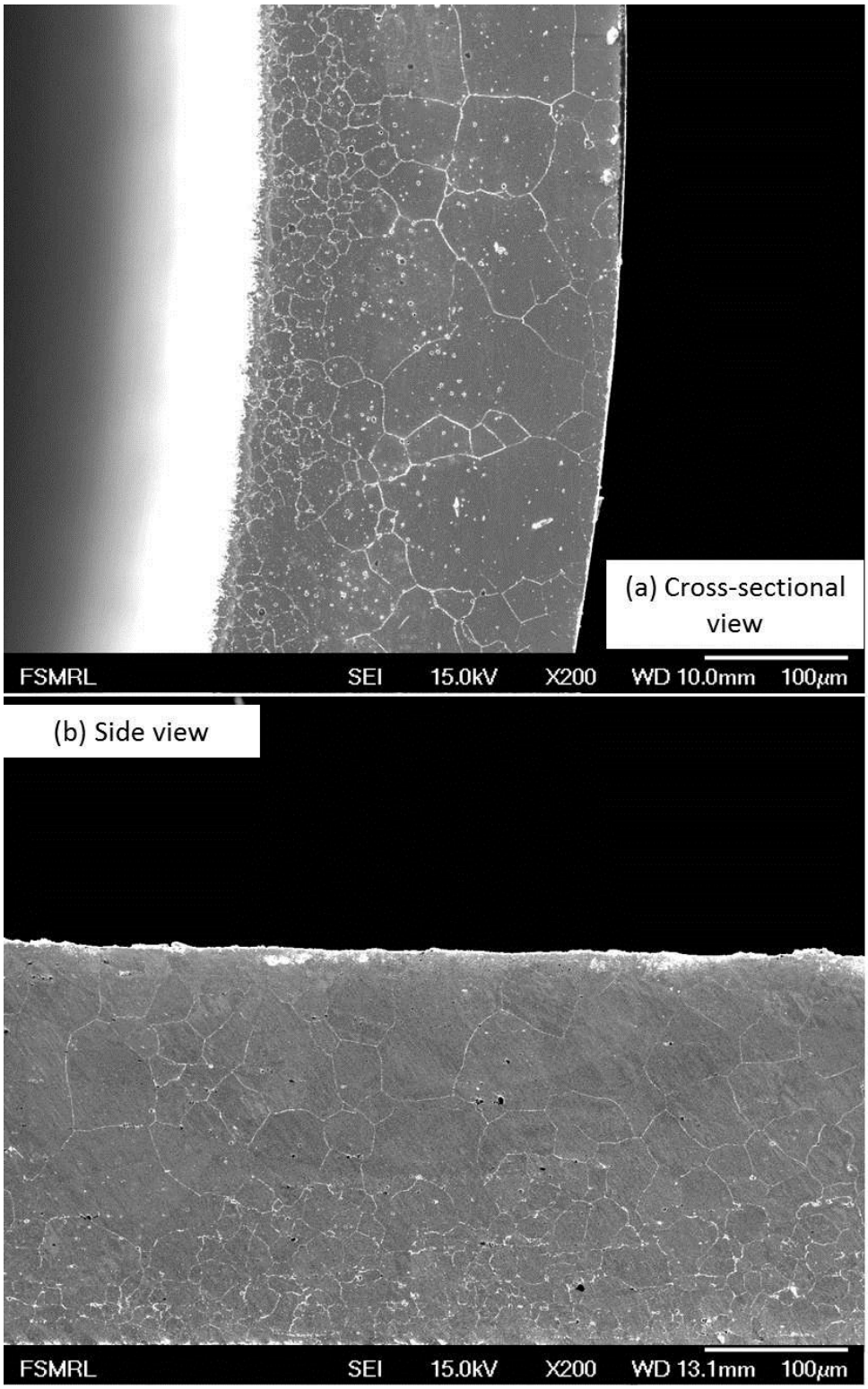

Fig. 3.6 Microstructures of as-received alloy 617 with (a) cross-sectional view and (b) side view.

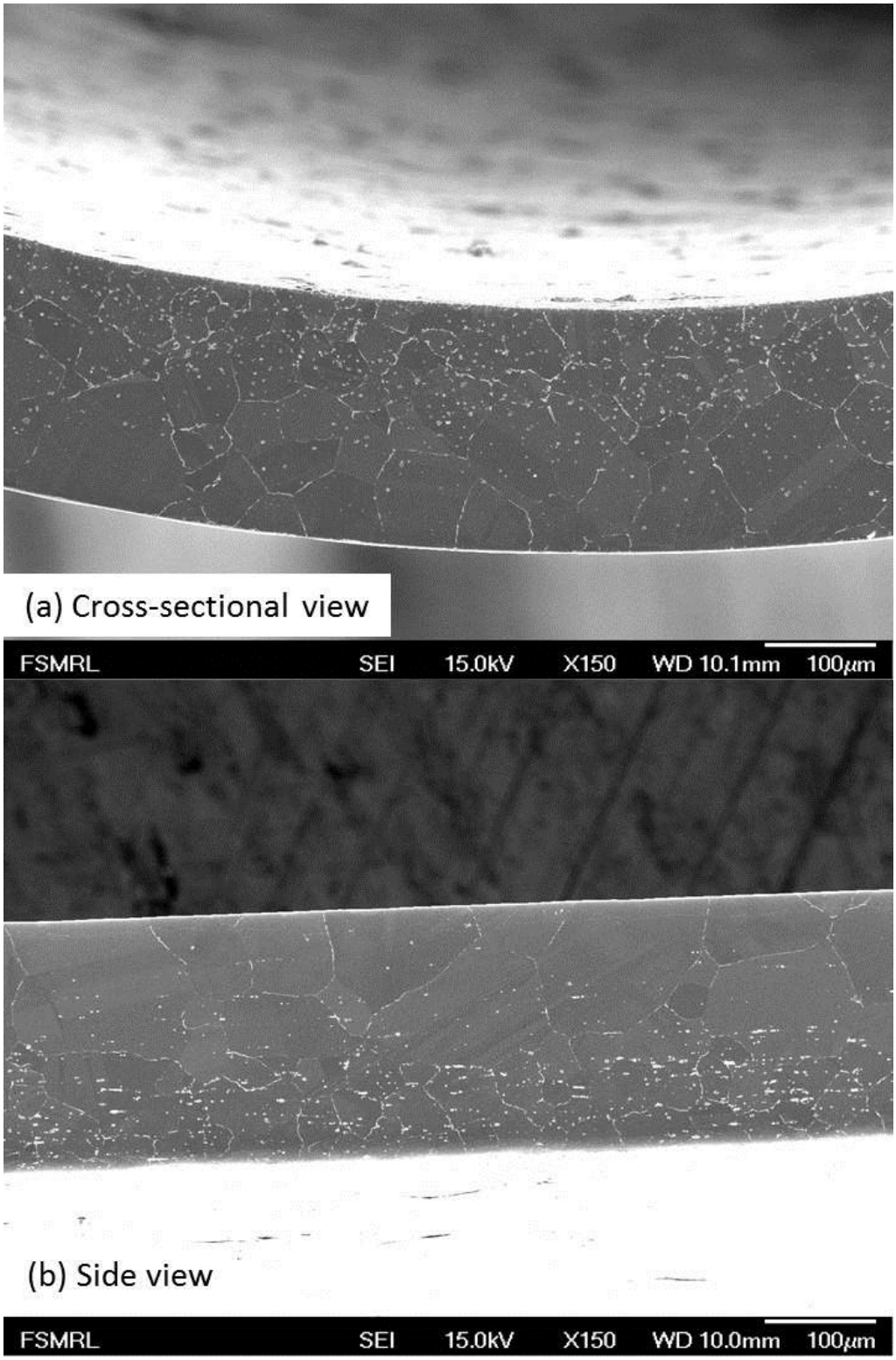

Fig. 3.7 Microstructures of as-received alloy 230 with (a) cross-sectional view and (b) side view.

CHAPTER 4

RESULTS

4.1 Corrosion Behavior of alloy 617 and alloy 230

4.1.1 Short-term oxidation behavior of alloy 617

The GIXRD results for the specimens oxidized at 850, 900, 950 and 1000^{o}C are shown in Fig. 4.1. It can be seen that the preliminary oxidation process was the development of an oxide scale comprised of chromia, Cr_2O_3, which matches the JCPDS file 38-1479. The surface composition of chromium and oxygen determined by XPS indicates that the ratio of O/Cr is 1.5, which is also characteristic of Cr_2O_3 and consistent with the GIXRD. A typical AES compositional depth profile is displayed in Fig. 4.2. It indicates that the compositions within the Cr_2O_3 are uniformly distributed through the thickness of the film. Fig. 4.3 (a)-(d) shows the cross-sectional view of the oxide layer prepared by FIB and viewed by SEM. The scale thickness values are summarized in Table 4.1 and show that the scale thickness increases with increasing oxidation temperature. The measured residual stresses of the scales and the underlying substrates for all specimens are listed in Table 4.1. It can be seen that the total residual stresses are compressive, with a stress range of -255.7 to -550.9 MPa. Residual stresses of alloy 617 decreases from 433.4 to 94 MPa with increasing oxidation temperatures.

The dependence of weight gain on the oxidation time at 850, 900, 950 and 1000^{o}C is shown in Fig. 4.4. It was found that two linear relationships are observed for all the specimens, suggesting that a two-stage oxidation process exists, and each stage follows a parabolic law of oxidation. The slope of each straight line represents the experimentally obtained parabolic rate constant k, governed by the following equation:

$$(\Delta W/A)^2 = k*t \qquad (4.1)$$

where ΔW is the weight change, A is the surface area of the specimen, k is the parabolic rate constant, and t is the oxidation time in seconds. Table 4.2 lists the rate constants for the two stages at all the temperatures. The rate constant can be described by Arrhenius equation

$$k = k_o \exp(-Q/RT) \qquad (4.2)$$

where k_o is the pre-exponential factor, Q is the activation energy, R is the gas constant, and T is temperature in Kelvin. The activation energy Q can be obtained by rearranging the eq. (4.2):

$$\log k = \log k_o - (Q/2.303R)(1/T) \qquad (4.3)$$

Fig. 4.5 shows a linear relationship between log k and 1/T for oxidation in each stage at various temperatures. The activation energy calculated based on the slope of the plot was also listed in Table 4.2. Fig.4.6 shows transition time for oxidation from the stage I to the stage II. It can be seen that the transition time decreases as the oxidation temperature increases.

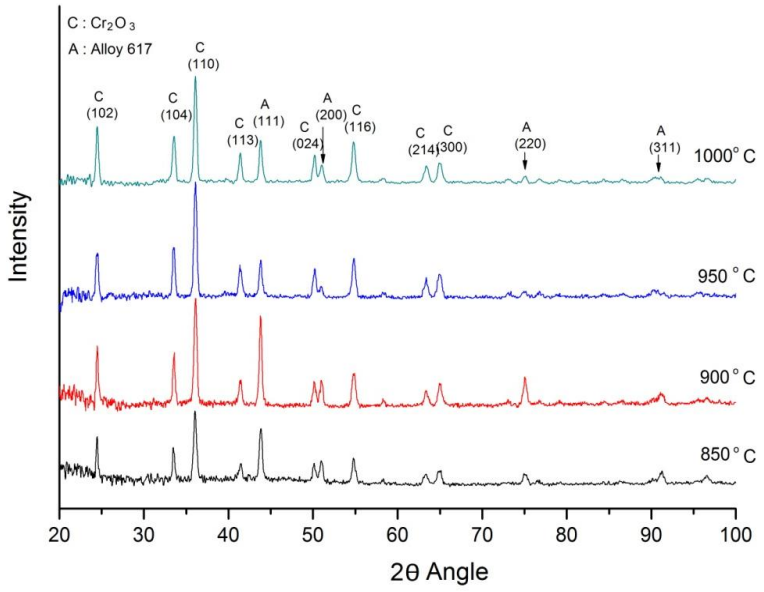

Fig. 4.1: Grazing incident X-ray diffraction of alloy 617 oxidized at four temperatures: 850, 900, 950 and 1000°C.

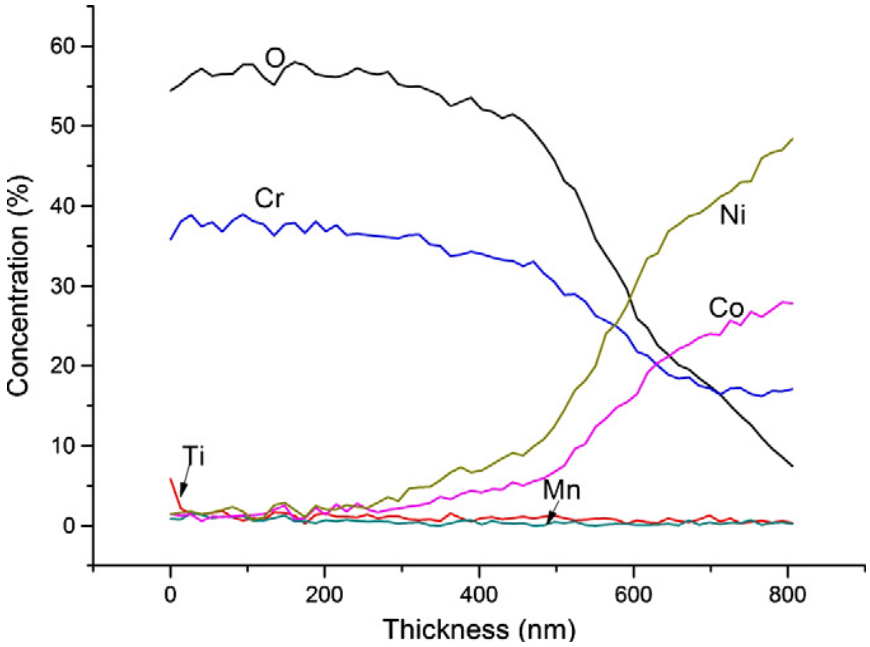

Fig. 4.2: The AES compositional depth profiles of the oxide layer on alloy 617 at oxidation temperature of 900^{o}C.

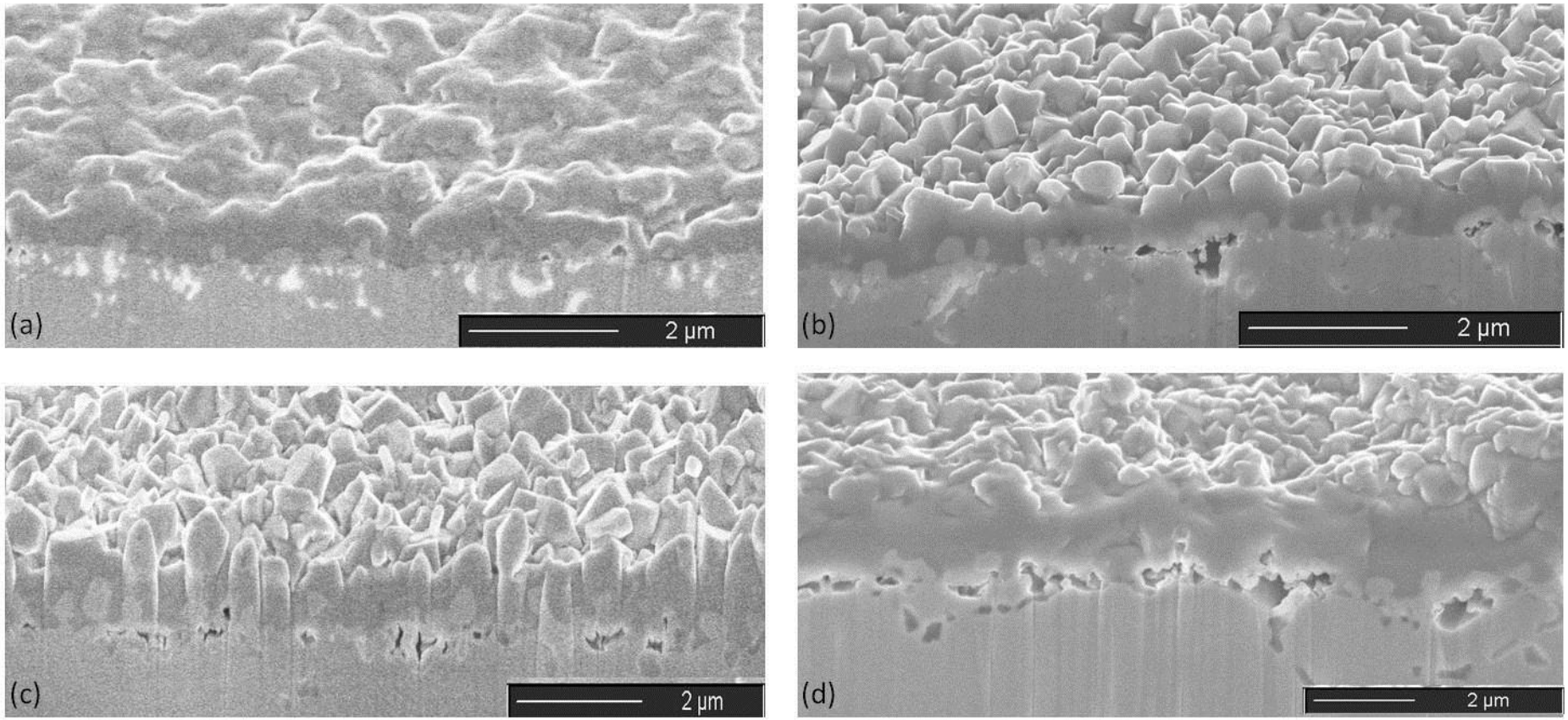

Fig. 4.3: A typical SEM image of Cr_2O_3 grown on alloy 617 at (a) 850 (b) 900 (c) 950 (d) 1000^{o}C.

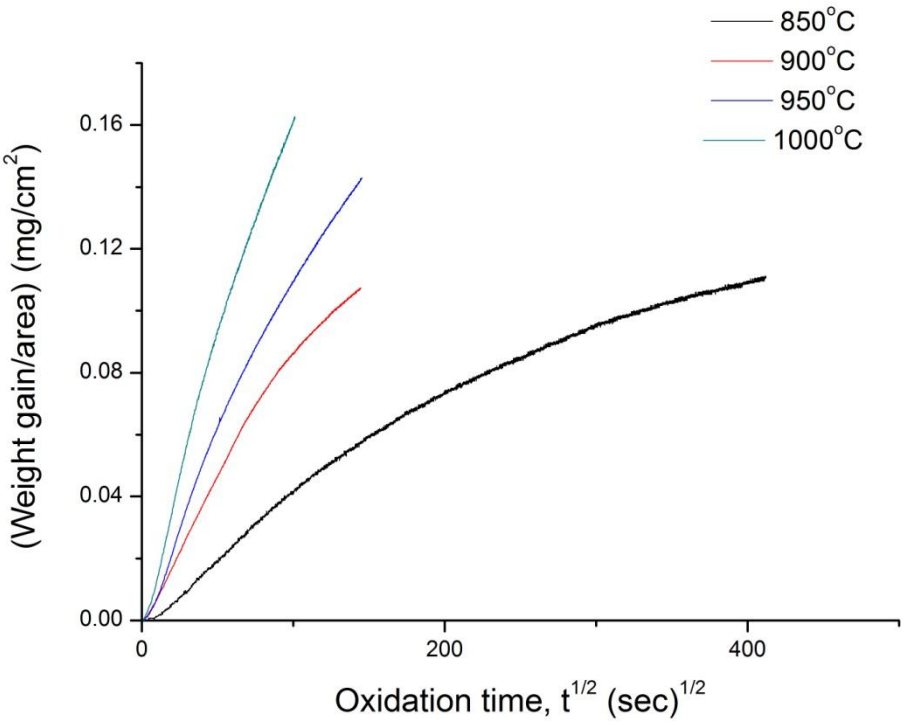

Fig. 4.4: Weight gain as a function of time for alloy 617 oxidized at 850, 900, 950 and 1000°C.

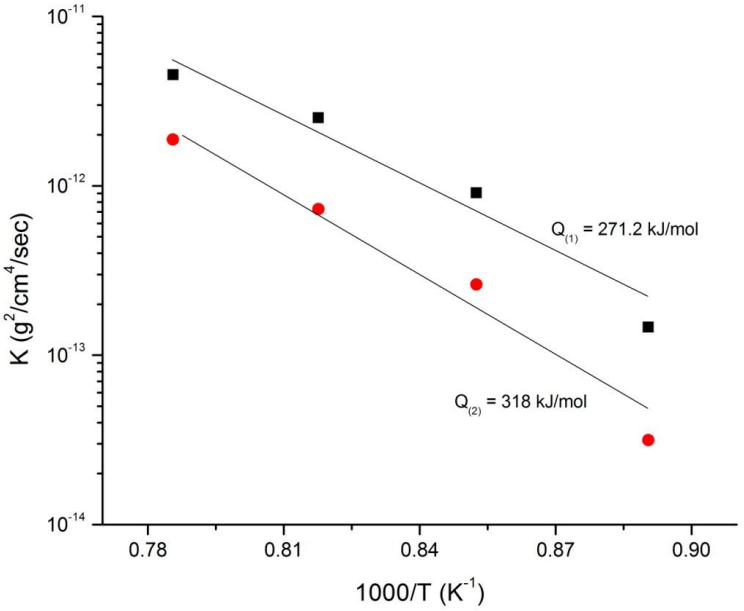

Fig. 4.5: The parabolic rate constant of alloy 617 as a function of temperature from 850 to 1000°C

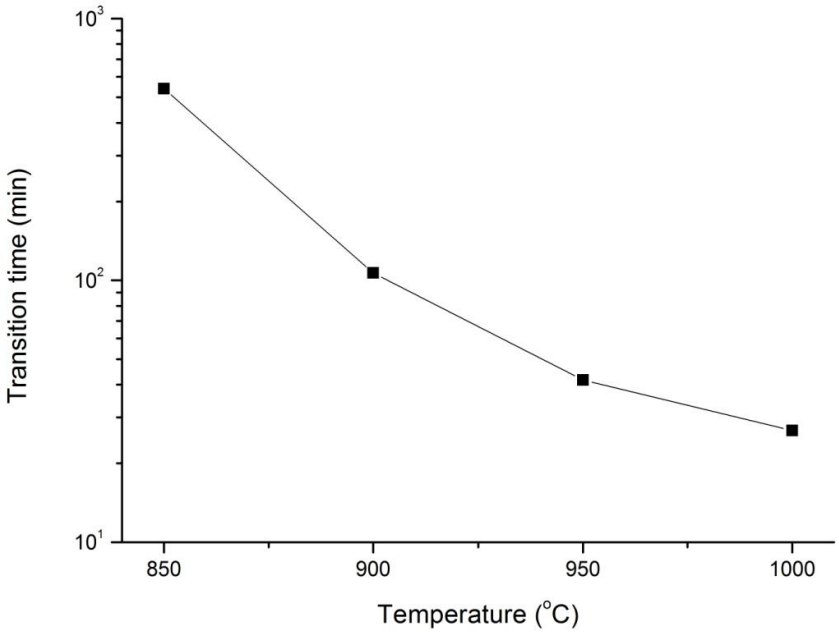

Fig. 4.6: The time necessary for alloy 617 from stage I oxidation to stage II oxidation.

Table 4.1: Summary of experimental results of alloy 617 oxidized at high temperatures.

Temperature (^{o}C)	Oxidation time (hr)	thickness (μm)	Oxide phase identification	Total residual stress of Cr_2O_3 (MPa)	Intrinsic residual stress of Cr_2O_3 (MPa)	Residual stress of alloy 617 (MPa)
850	6	0.35	Cr_2O_3	-424.7	806.8	433.4
900	6	0.6	Cr_2O_3	-255.7	1050.5	165.6
950	6	0.82	Cr_2O_3	-550.9	829.8	157.6
1000	3	0.98	Cr_2O_3	-473.9	981.5	94

Table 4.2: Summary of parabolic rate constants (K) and activation energies (Q) for the two stages at oxidation temperature of 850,900,950 and 1000^{o}C

parabolic rate constant ($g^2/cm^4/sec$)	850^{o}C	900^{o}C	950^{o}C	1000^{o}C	Q (kJ/mol)
$K_{(1)}$	$1.47x10^{-13}$	$9.08x10^{-13}$	$2.52x10^{-12}$	$4.54x10^{-12}$	271.2
$K_{(2)}$	$3.15x10^{-14}$	$2.61x10^{-13}$	$7.28x10^{-13}$	$1.88*10^{-12}$	318

4.1.2 Short-term oxidation behavior of alloy 230

Fig. 4.7 depicts the XRD patterns for all specimens. Since there are few diffractions peaks in the spectra, GIXRD patterns were used for phase identification (Fig.4.8). The results of GIXRD revealed that the oxide phases observed were Cr_2O_3, and spinel-type $MnCr_2O_4$ using JCPDS file no. 38-1479 and 75-1614, respectively. As shown in Fig. 4.7 and 4.8, the diffraction peaks becomes more distinct as the oxidation temperature increases. The fraction of $MnCr_2O_4$ can be calculated as follows:

$$\frac{\sum I_{MnCr_2O_4}}{\sum I_{MnCr_2O_4} + \sum I_{Cr_2O_3}} \qquad (4.4)$$

where $\sum I_{MnCr_2O_4}$ and $\sum I_{Cr_2O_3}$ are integrated peak intensity of $MnCr_2O_4$ and Cr_2O_3 from XRD. The ratio of $MnCr_2O_4$ is listed in Table 4.3. It can be seen that the dominant oxide phase is Cr_2O_3. In addition, the $MnCr_2O_4$ fraction is found to be nearly constant across all of the exposure temperatures. The microstructures of the scales were displayed in Fig. 4.9 (a)-(d), showing a dense with good adhesion oxide layer grown on the substrate.

Fig. 4.10 shows the dependence of weight gain on the oxidation time at 850, 900, 950 and 1000^{o}C. Two linear relationships are exhibited for all the specimens. This suggests that during the incipient oxidation, a two-stage oxidation process exists, and each stage follows a parabolic law of oxidation. The oxidation rate and the parabolic rate constants for the two stages are listed in Table 4.4 for each exposure temperature. Fig. 4.11 shows a linear relationship between log k and 1/T for oxidation in each stage at various temperatures. The activation energy for the stage I and stage II are 246.5 and 212.1 kJ/mol, respectively. Figure 4.12 shows transition times between the two stages of oxidation for all of the oxidized specimens. It can be seen that the transition time decreases significantly from 850 to 900^{o}C. As the temperature increases from 900 to 950^{o}C, the transition time decrease slowly. At 1000^{o}C, no significant variation can be observed. Note also that the oxidation rate decreases in the stage II compared to stage I for all conditions.

The measured residual stresses of the scale and the underlying substrate for all specimens are listed in Table 4.3. It is noted that the total (measured) residual stresses of Cr_2O_3 is compressive, whereas that of alloy 230 is tensile.

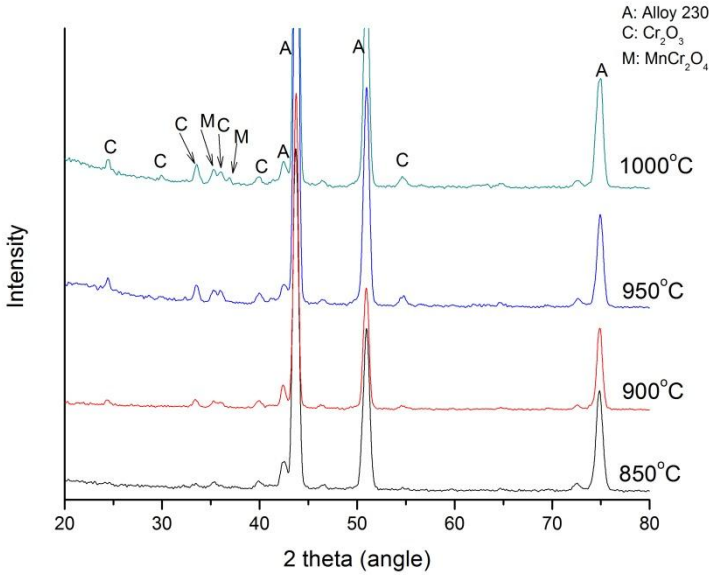

Fig. 4.7: The XRD patterns for the specimens oxidized at 850, 900, 950 and 1000°C.

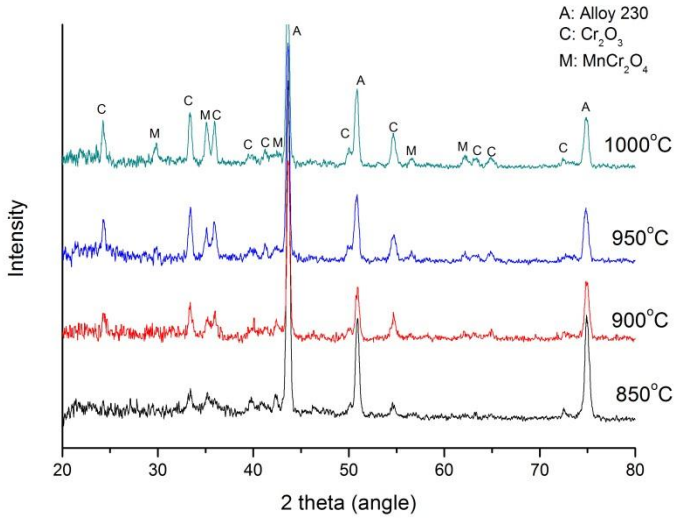

Fig. 4.8: The GIXRD patterns for the specimens oxidized at 850, 900, 950 and 1000°C.

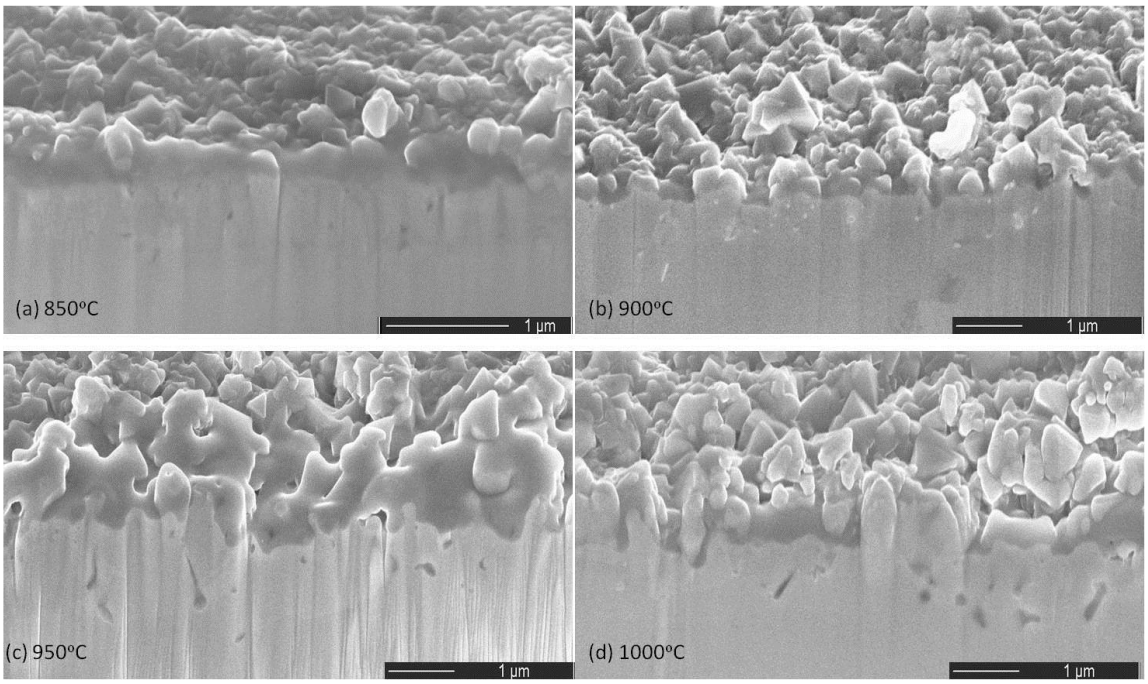

Fig. 4.9: A typical SEM image of the oxide layer grown on alloy 230 at (a) 850 (b) 900 (c) 950 (d) 1000°C.

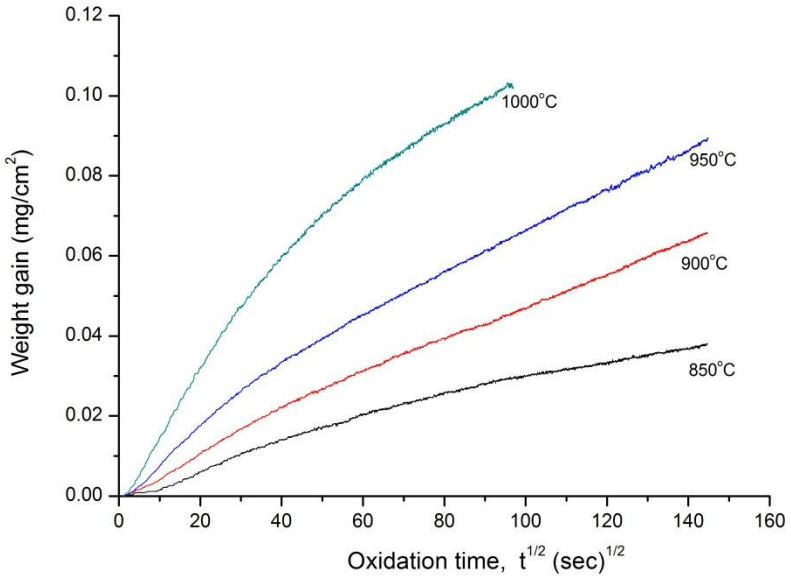

Fig. 4.10: Weight gain as a function of oxidation time for alloy 230 oxidized at 850, 900, 950 and 1000°C.

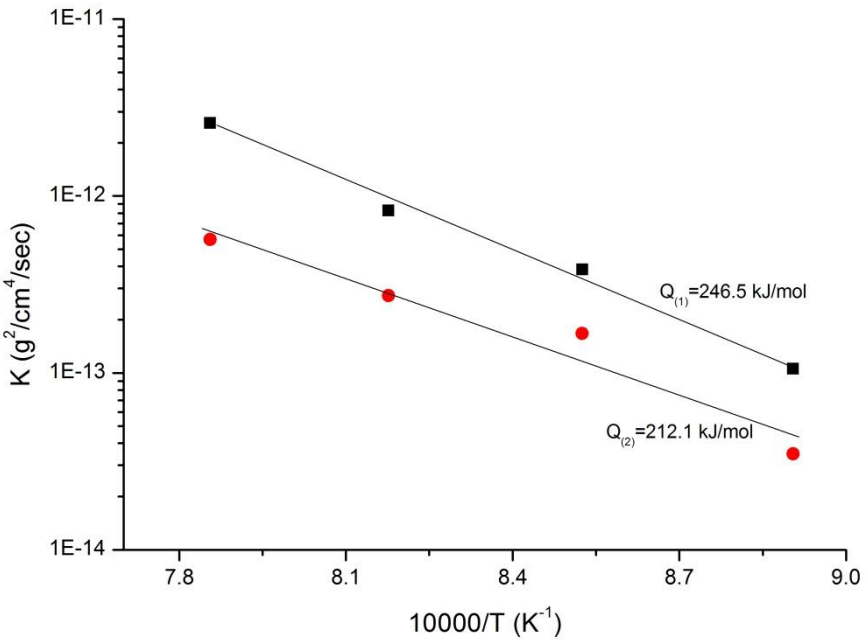

Fig. 4.11: The parabolic rate constant as s function of oxidation temperature from 850 to 1000°C

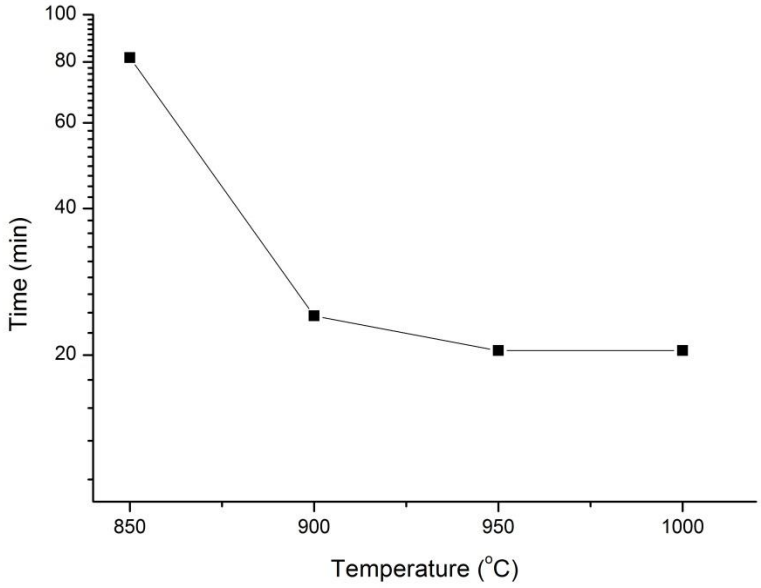

Fig. 4.12: Transition time between stage I oxidation and stage II oxidation as a function of temperatures.

Table 4.3: Summary of experimental results of alloy 230 oxidized at high temperatures.

Temperature (^{o}C)	Oxidation time (hr)	thickness (μm)	XRD phase ratio $MnCr_2O_4$ (%)	Total residual stress of Cr_2O_3 (MPa)	Intrinsic residual stress of Cr_2O_3 (MPa)	Residual stress of alloy 230 (MPa)
850	6	0.22	16.9	-514.6	684.9	866.0
900	6	0.3	15.6	-147.6	1124.5	587.3
950	6	0.55	14.3	-127.3	1217.5	573.2
1000	3	0.76	18.1	-109.1	1308.4	381.1

Table 4.4: Summary of parabolic rate constants (K) and activation energies (Q) for the two oxidation stages

Oxidation behavior	Parabolic rate constant ($g^2/cm^4/sec$)	850^{o}C	900^{o}C	950^{o}C	1000^{o}C	Q (kJ/mol)
Stage I	$K_{(1)}$	1.06×10^{-13}	3.84×10^{-13}	8.29×10^{-13}	2.59×10^{-12}	246.5
Stage II	$K_{(2)}$	3.48×10^{-14}	1.67×10^{-13}	2.73×10^{-13}	5.67×10^{-13}	212.1

4.1.3 Long-term oxidation behavior of alloy 617 and alloy 230

Fig. 4.13 (a) shows the weight gain as a function of exposure time in air up to 1512 hours for alloy 617. At 950^{o}C, the discontinuous course of the curve indicates that spallation of oxidation scale occurred during the isothermal annealing in the experiment. It can be seen that after 1224 h exposure, significant spallation of the oxide scale was observed. For alloy 617 exposed at 850^{o}C, the relatively continuous course of the curve was obtained, showing that the growth of oxide scale is relatively stable and no significant spallation of the oxide scale was observed. Fig. 4.13 (b) shows the weight gain as a function of exposure time in air up to 1512 hours for alloy 230. For both temperatures, the weight gradually and stably increased and no significant spallation was observed. Table 4.5 summarizes the oxidation rate constants at the two temperatures for both alloys.

Oxide phases grown on alloy 617, identified by XRD, were shown in Fig. 4.14 (a) and (b) for exposure temperature of 950 and 850^{o}C, respectively. At 850^{o}C, the phase, which is present after 1512 h exposure, was Cr_2O_3 only. As for oxidation at 950^{o}C, the oxide phase initially is Cr_2O_3, followed by the appearance of spinel phases, $NiCr_2O_4$, around 360 h exposure time. As the annealing time increases, the diffraction peaks of $NiCr_2O_4$ become more distinct. For oxide phases grown on alloy 230, results of XRD show that the two phases are present, Cr_2O_3 and $MnCr_2O_4$ (Fig. 4.15(a) and (b)). These are consistent to that obtained in the TGA experiments under the same temperatures.

Fig. 4.16 (a)-(d) depicts evolution of surface morphology of alloy 617 at 950^{o}C. After 24 h exposure, only Cr_2O_3 formed. The results of energy-dispersive x-ray spectroscopy (EDS), shown in Fig. 4.16 (e) and (f), demonstrated the chemical compositions of large and smaller particles. As the exposure time increased to 360 h, the dominated oxide scale (Cr_2O_3) along with the appearance of small particles ($NiCr_2O_4$) was observed. With increasing the exposure time (720 h), significant amount of $NiCr_2O_4$ formed on Cr_2O_3. After 1512 h exposure, the surface area occupied by $NiCr_2O_4$ is approximately equal to that by Cr_2O_3. Evolution of surface morphology of alloy 230 at 950^{o}C is shown in Fig. 4.17. The surface is covered with small crystals after 24 h exposure. As the exposure increased to 360 h, a structure with larger and smaller grains is observed. With increasing exposure time from 720 h to 1512 h, it can be seen that large grains are significantly covered by the small grains.

Table 4.5: Long-term oxidation rate constant for alloy 617 and alloy 230 at 850 and 950°C

Long-term oxidation rate constant ($g^2/cm^4/sec$)	850°C	950°C
Alloy 617	$1.61 * 10^{-13}$	$8.18 * 10^{-13}$
Alloy230	$1.42 * 10^{-14}$	$2.15 * 10^{-13}$

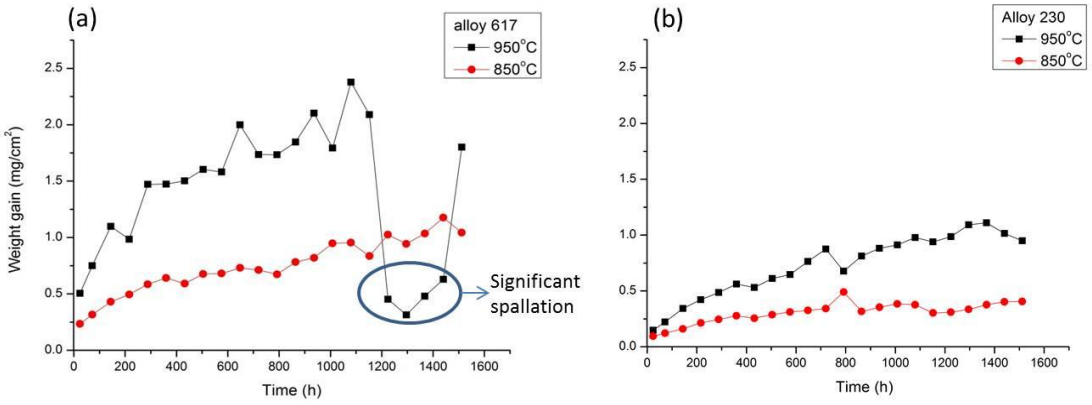

Fig. 4.13: Weight gain as a function of exposure time in air at 850 and 950°C for (a) alloy 617 and (b) alloy 230.

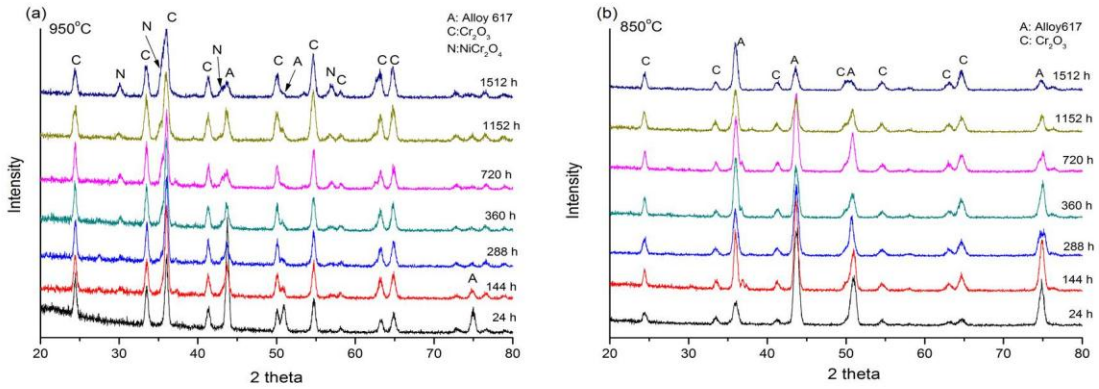

Fig. 4.14: Evolution of oxide phase after long-term exposure to air at 950°C for (a) alloy 617 and (b) alloy 230.

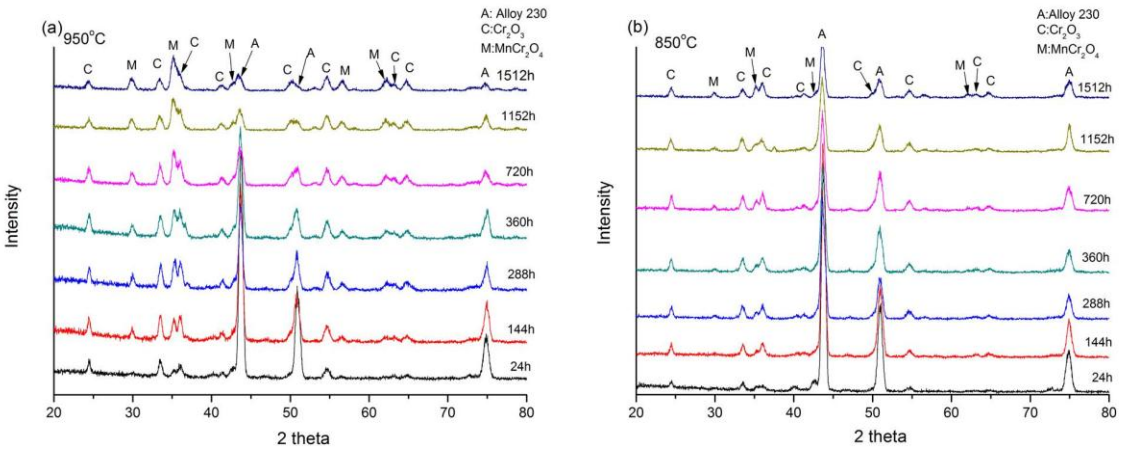

Fig. 4.15: Phase identification by XRD in air for alloy 230 at (a) 950 and (b) 850°C

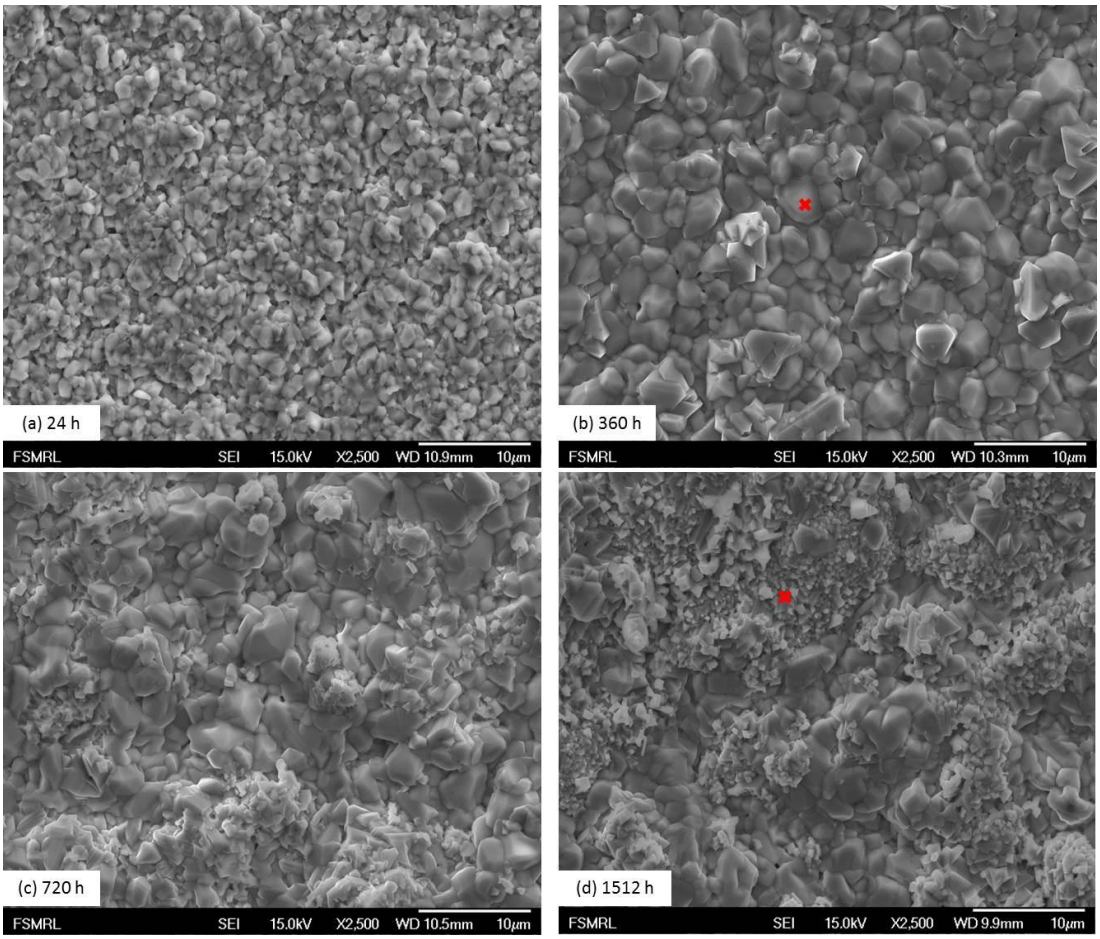

Fig. 4.16: Surface morphology of alloy 617 after exposure of (a) 24 h, (b) 360 h, (c) 720 h (d) 1512 h in air at 950°C. Note that the larger particle is Cr_2O_3.EDS analysis of surface morphology of (e) 360 h and (f) 1512 h marked by the cross in (b) and (d), respectively. Note that the larger particle is Cr_2O_3 while the small particles is $NiCr_2O_4$

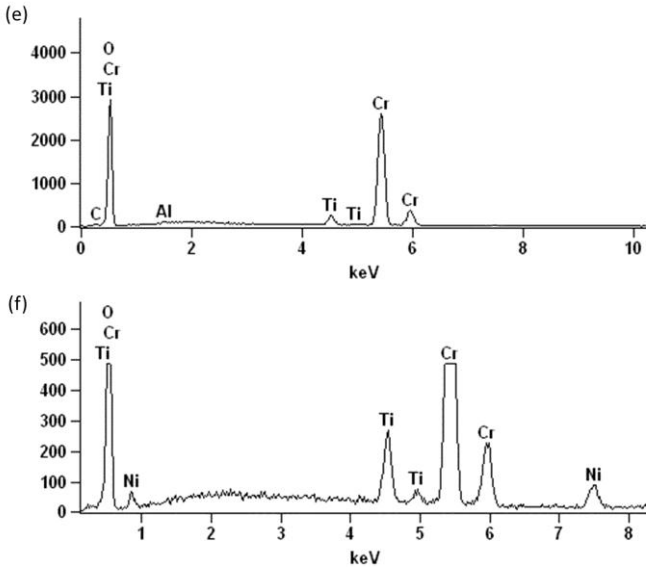

Fig. 4.16 (cont.)

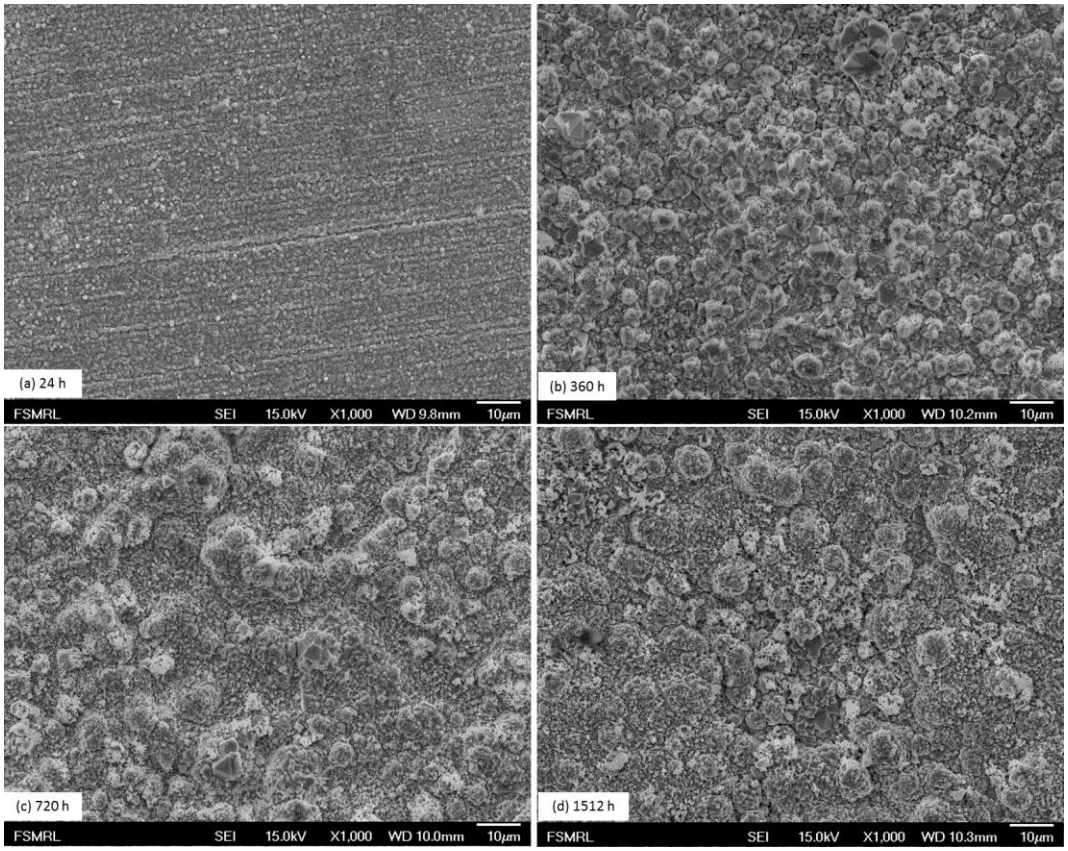

Fig. 4.17: Surface morphology of alloy 230 after exposure of (a) 24 h, (b) 360 h, (c) 720 h (d) 1512 h in air at 950^{o}C.

4.1.4 Short-term corrosion behavior of alloy 617 and alloy 230 under a He+ 5% H_2 atmosphere

Fig. 4.18 (a) and (b) shows the weight change vs. time exposed to the He + 5% H_2 mixed gases (a reducing environment) for alloy 617 and alloy 230, respectively. It can be seen that for alloy 617, the weight initially decreased and then increased at 850 and 900^{o}C. At 950^{o}C, the weight decreased and stabilized around 60 min and then increased. At 1000^{o}C, the weight graduate decreased with time. As for alloy 203 exposed to such environment, the weight initially decreased and stabilized at 850 and 900^{o}C. At higher temperatures, the weight decreases. It is observed that the decreasing rate increases with increasing temperature. Fig. 4.19 (a) depicts the oxide phase of alloy 617. The oxide phase for alloy 617 is Cr_2O_3, the same as the results obtained in the air environment. The oxide phases for alloy 230 are Cr_2O_3 + $MnCr_2O_4$, as suggested by Fig. 4.19 (b). The oxide phases are identical to that observed in air environment. These results suggests that the He + 5% H_2, which produces lower oxygen partial pressure, did not influence the oxide phases that were observed in the air environments. Fig. 4.20 (a)-(d) and Fig. 4.21 (a)-(d) shows cross-sectional view of oxide grown on alloy 617 and alloy 230, respectively. Fig. 4.21 (e) and (f) shows the surface morphology and the corresponding compositions of the surface oxide. The chemical analysis by EDS indicates a strong chromium peak along with small manganese peaks, suggesting the oxide phases mainly consists of Cr_2O_3 and $MnCr_2O_4$, which is consistent of GIXRD results. Signals of aluminum and silicon with small intensity may arise from the formation of Al_2O_3 and SiO_2. It is found that unnegligible intensity from nickel element was also detected on the surface oxide

Residual stress measurements of the oxide scale for the two alloys were performed, as shown in Fig. 4.22 (a) and (b). It can be seen that, during the growth of the oxide at high temperatures, the stress state for both alloys is tensile in the He + 5% H_2 environment. The variation of the stress developed on the oxide grown on alloy 617 is not significant, ranging from 576 to 709 MPa. As for alloy 230, the stress ranged from 624 to 921 MPa.

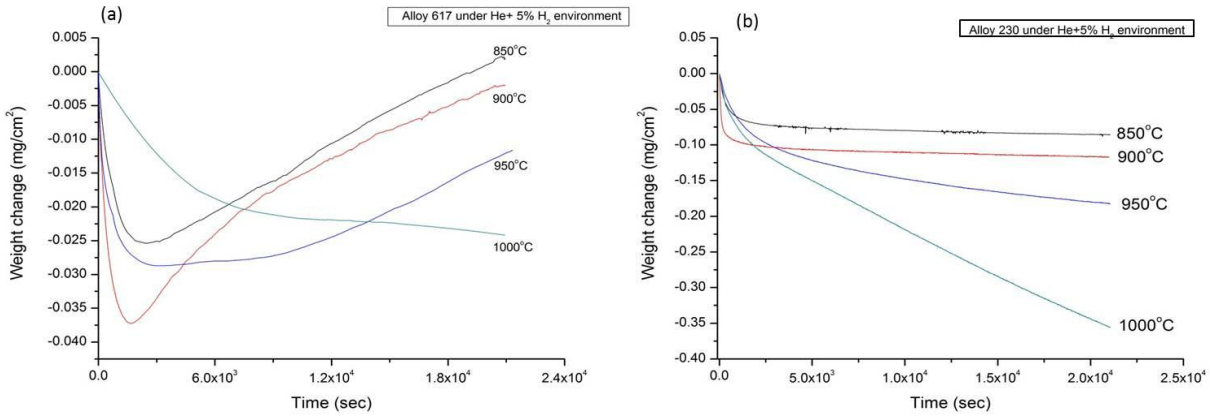

Fig. 4.18: Weight change as a function of. time exposed to the He + 5% H_2 environment for (a) alloy 617 and (b) alloy 230 from 850 to 1000°C

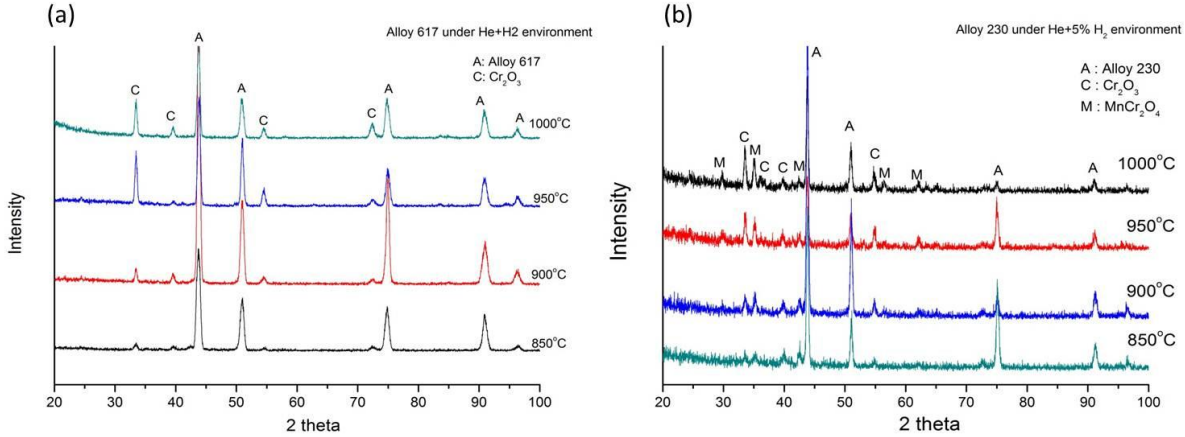

Fig. 4.19: Phase identification by XRD for (a) alloy 617 (b) alloy 230 under reducing environment

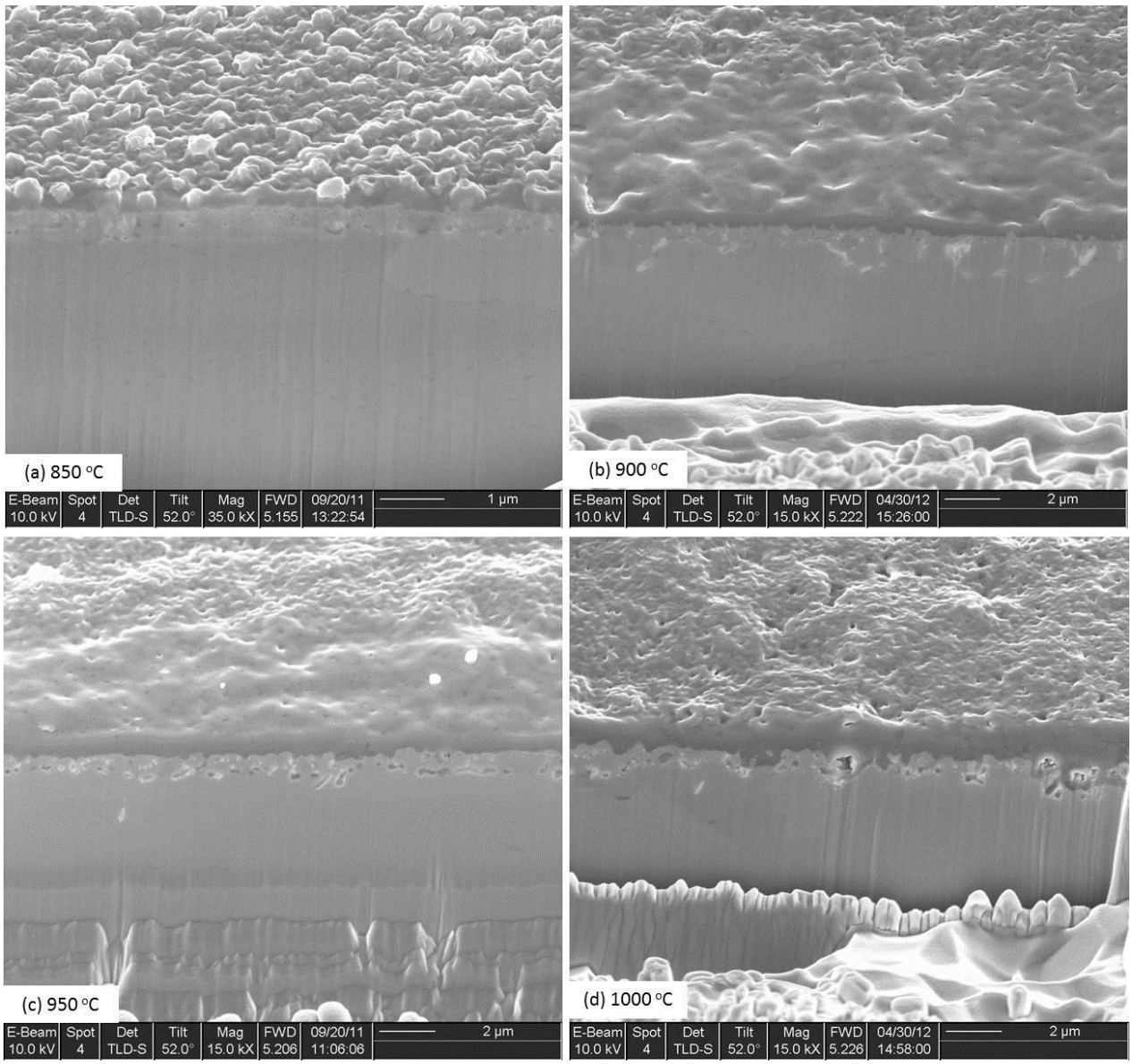

Fig. 4.20: A cross-sectional SEM image of the oxide layer grown on alloy 617 at (a) 850 (b) 900 (c) 950 (d) 1000^{o}C.

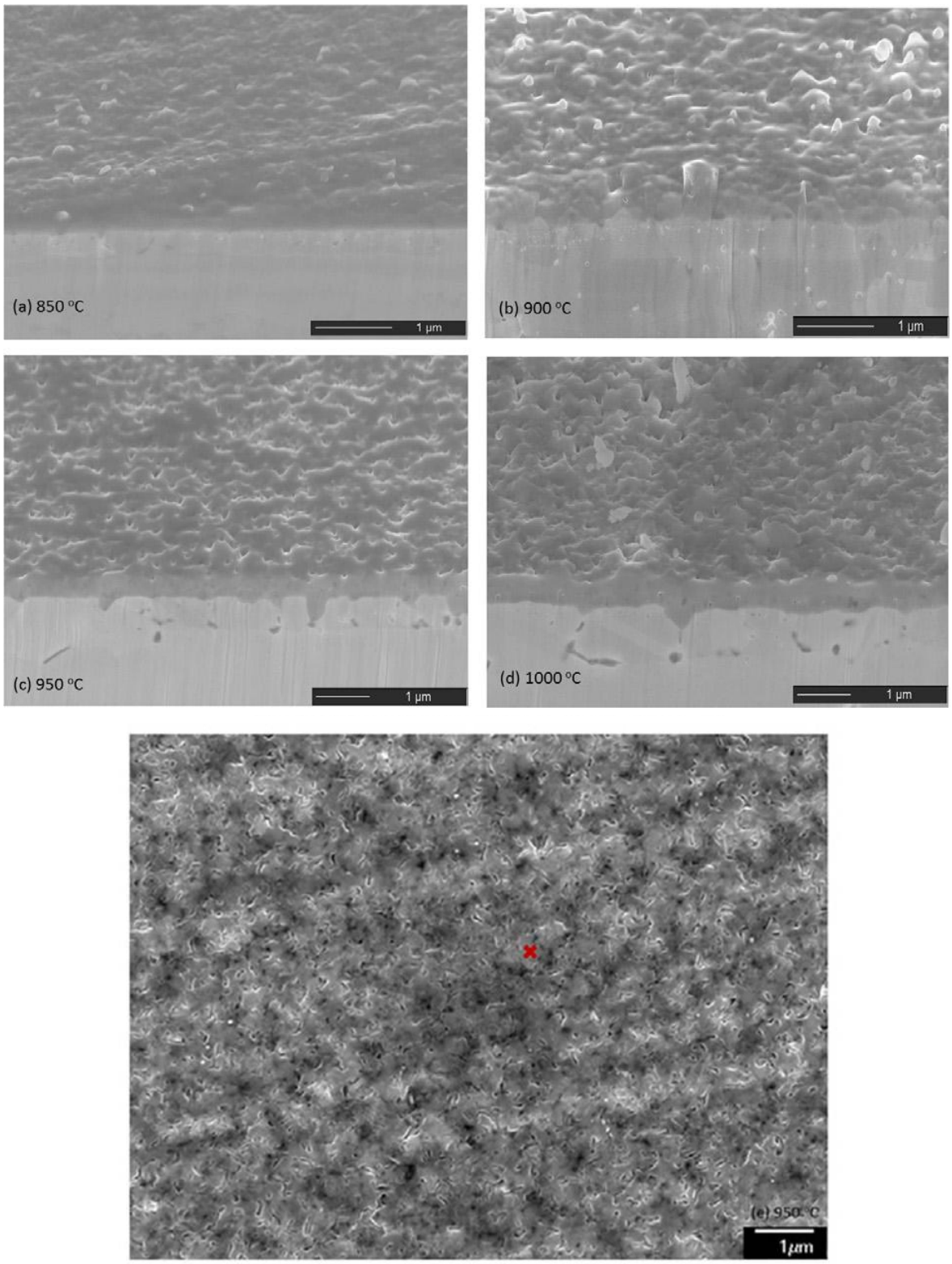

Fig. 4.21: A cross-sectional SEM image of the oxide layer grown on alloy 230 at (a) 850 (b) 900 (c) 950 (d) 1000^{o}C, and surface morphology of the oxide at (e) 950^{o}C. (f) A typical EDS analysis of the surface oxide marked by the cross.

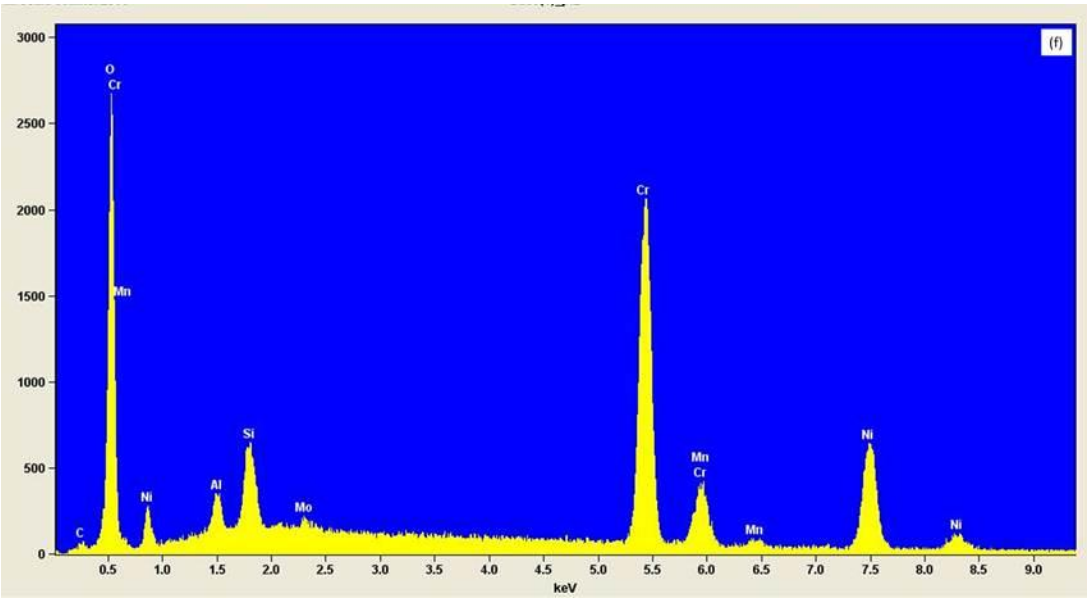

Fig. 4.21 (cont.)

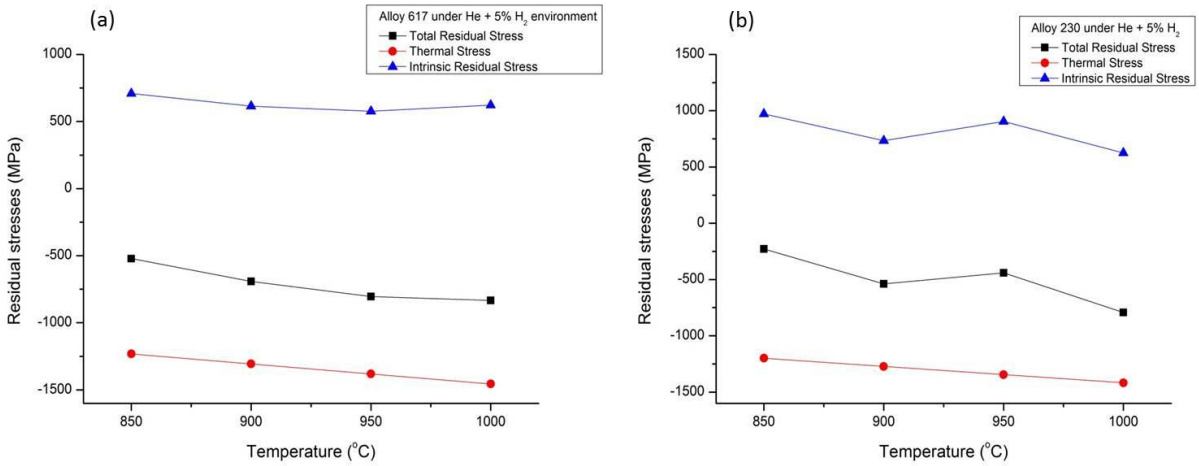

Fig. 4.22: Residual stress as a function of exposure temperature for the oxide grown on (a) alloy 617 and (b) alloy 230.

4.1.5 Long-term corrosion behavior of alloy 617 and alloy 230 under a He+ 5% H_2 environment

The weight change after long-term exposure of the He + 5% H_2 environment is shown in Fig. 4.23 (a) and (b) for alloy 617 and alloy 230, respectively. The results showed that both the alloys increased in weight. The weight increase in alloy 617 is more significant than that in alloy 230. It can be seen that the two curves follows the parabolic rate law after long-term exposure. Oxide phases grown on alloy 617 and alloy 230, identified by XRD, were shown in Fig. 4.24 (a) and (b), respectively. For alloy 617, the oxide phase initially is Cr_2O_3, followed by the significant appearance of two phases, Cr_2O_3 + $MnCr_2O_4$, around exposure time of 144 h. As the annealing time increases, the diffraction peaks of $MnCr_2O_4$ becomes more distinct. For oxide phases grown on alloy 230, results of XRD show that the two phases are present, Cr_2O_3 and $MnCr_2O_4$. These are consistent with that obtained in the TGA experiments under the same temperatures. Fig. 4.25 (a) and (b) showed the residual stresses measurements for alloy 617 and 230, respectively. The intrinsic stresses range from 687 to 840 MPa for alloy 617. As for alloy 230, the intrinsic stresses range from 580 to 895 MPa. It is noted that that the intrinsic residual stress are tensile.

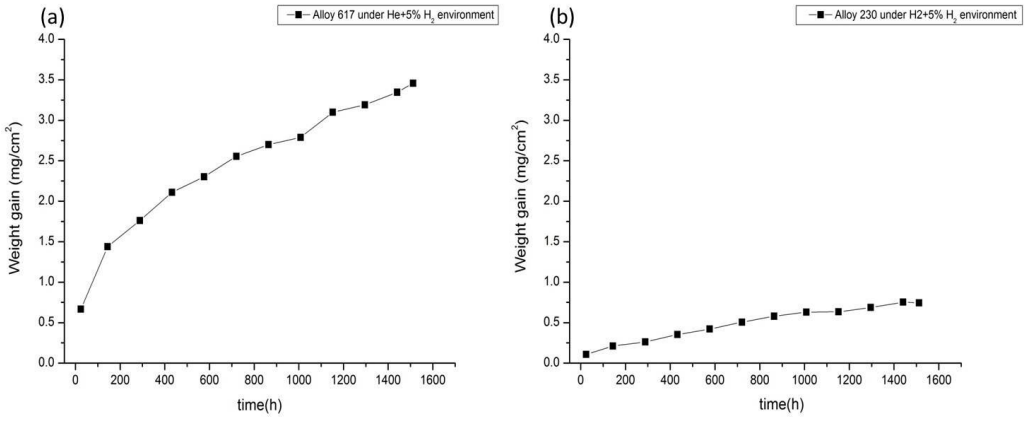

Fig. 4.23: Weight gain as a function of exposure time in He + 5% H_2 atmosphere at 950^{o}C for (a) alloy 617 and (b) alloy 230.

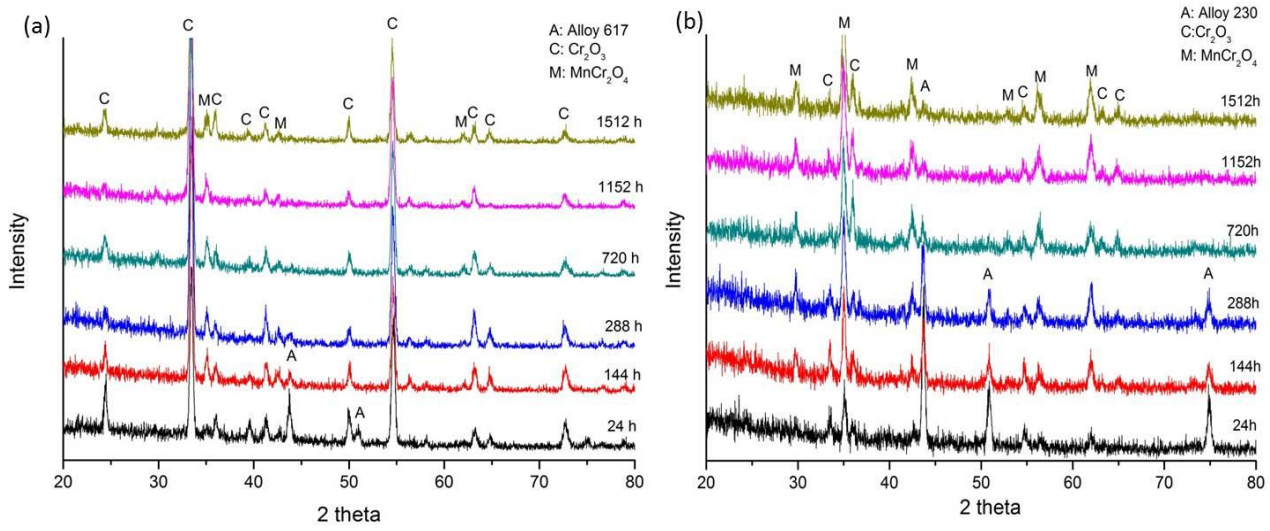

Fig. 4.24: Evolution of oxide phase after long-term exposure to He + 5% H_2 atmosphere at 950^{o}C for (a) alloy 617 and (b) alloy 230.

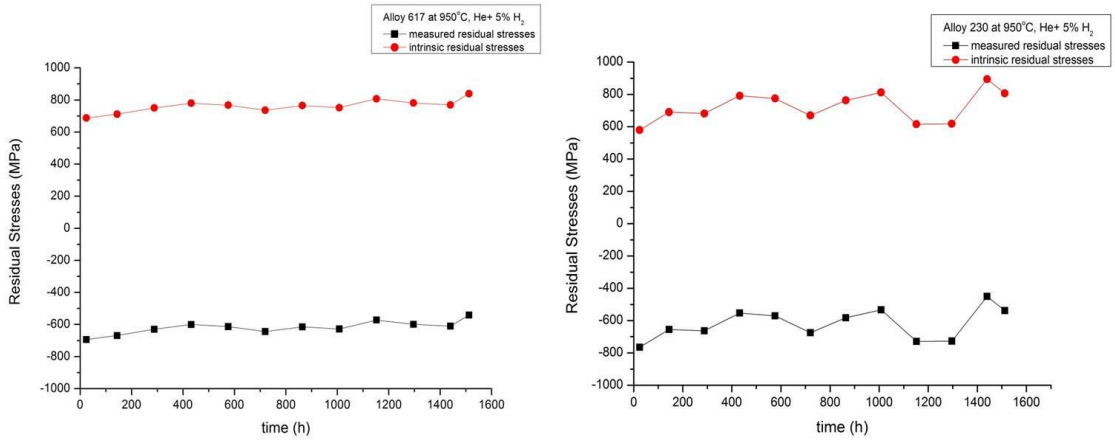

Fig. 4.25: Residual stresses as a function of time for the oxide grown on (a) alloy 617 and (b) alloy 230.

4.1.6 Carburization behavior of alloy 617 and alloy 230 under a He+ 5% H_2 + 1% CH_4 environment

Fig. 4.26 showed the weight change of alloy 617 at four exposure temperatures under the He +5% H_2 + 1% CH_4 environment (carbonaceous atmosphere). It can be seen that the loss of the weight decreases initially, followed by the increase in weight. Fig. 4.27 showed that carbides, identified as Cr_3C_2 by XRD (ICCD # 00-035-0804), are present in alloy 617. Fig. 4.28 shows the cross-sectional view of carburation zone of alloy 617. With increasing exposure temperature, the depth of the carburation zone increases. As for alloy 230, the weight increases with increasing exposure temperatures as shown in Fig. 4.29. Results of XRD (Fig. 4.30) showed that carbides, Cr_3C_2, are present in alloy 230 (ICCD # 00-035-0804). Fig. 4.31 shows the cross-sectional view of carburation zone of alloy 230. It can be seen that plate-like carbides are formed. With increasing exposure temperature, the depth of the carburation zone increases. These results suggest that at high temperatures, thermally cracking of CH_4 and deposition of carbon on the two alloys occurred. Therefore, the carburization phenomenon was observed in both alloys.

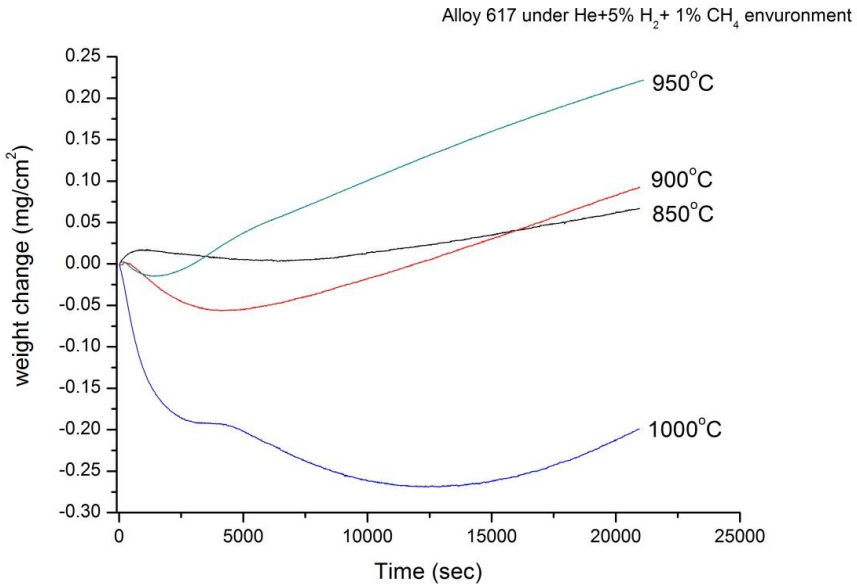

Fig. 4.26: Weight change as a function of exposure time in carbonaceous atmosphere from 850 to 1000°C for alloy 617.

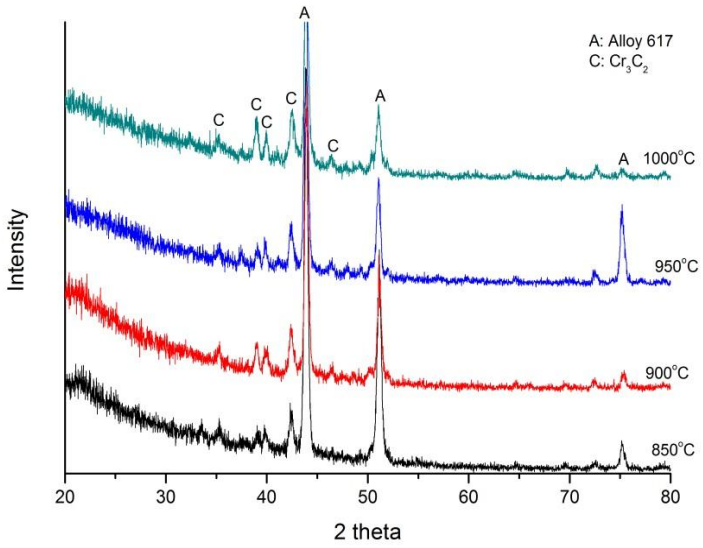

Fig. 4.27: Phase identification by XRD for alloy 617 from 850 to 1000^{o}C under carbonaceous environment.

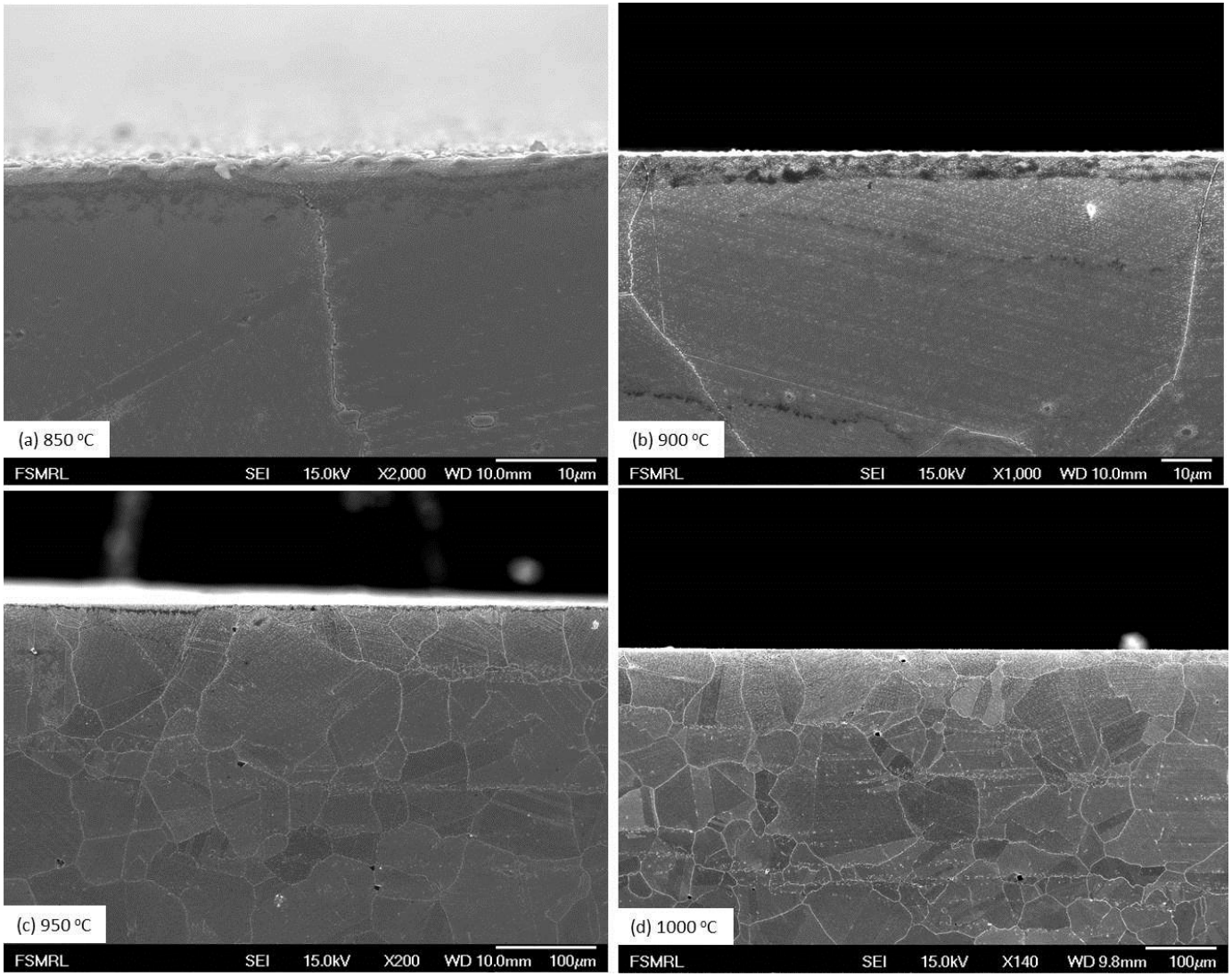

Fig. 4.28: Cross-sectional view of alloy 617 exposed to carbonaceous environment

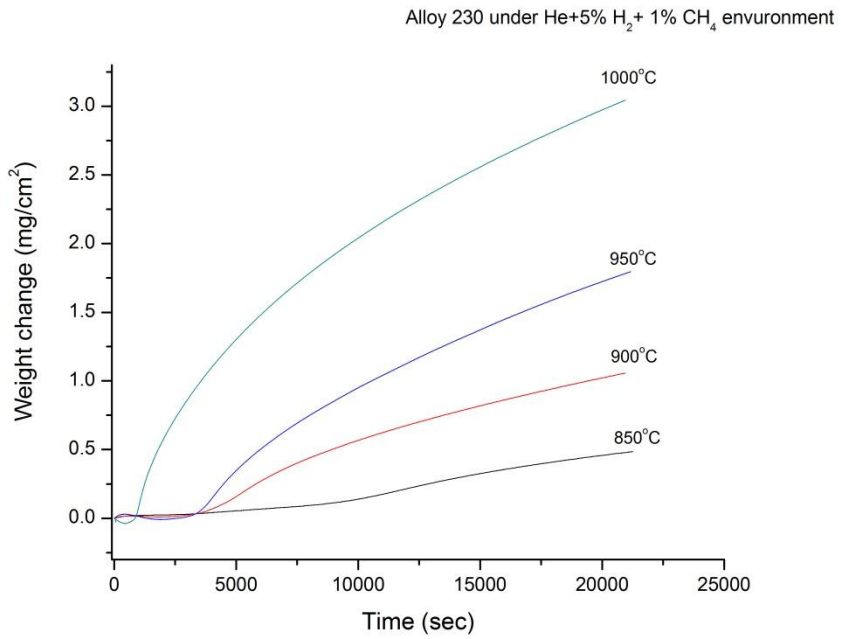

Fig. 4.29: Weight change as a function of exposure time in carbonaceous atmosphere from 850 to 1000°C for alloy 230.

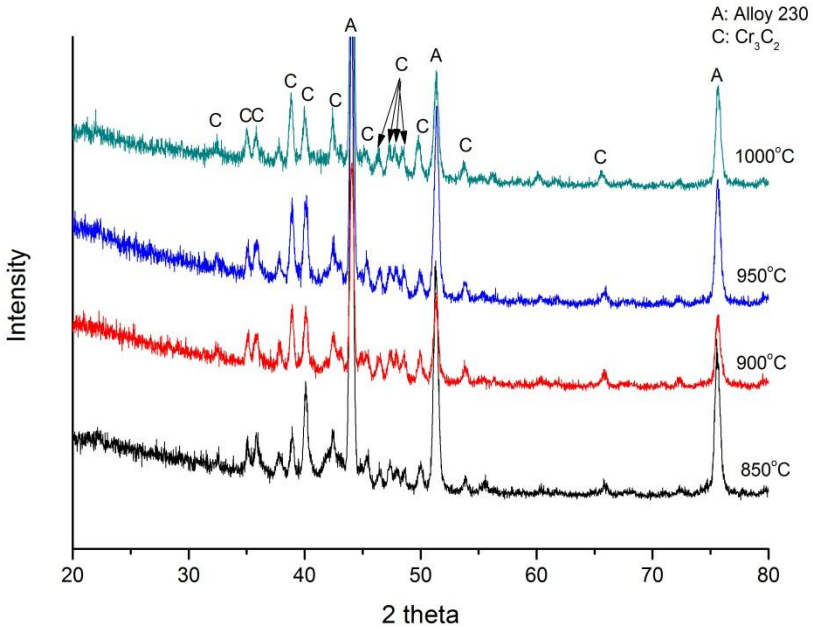

Fig. 4.30: Phase identification by XRD for alloy 230 from 850 to 1000°C under the carbonaceous environment.

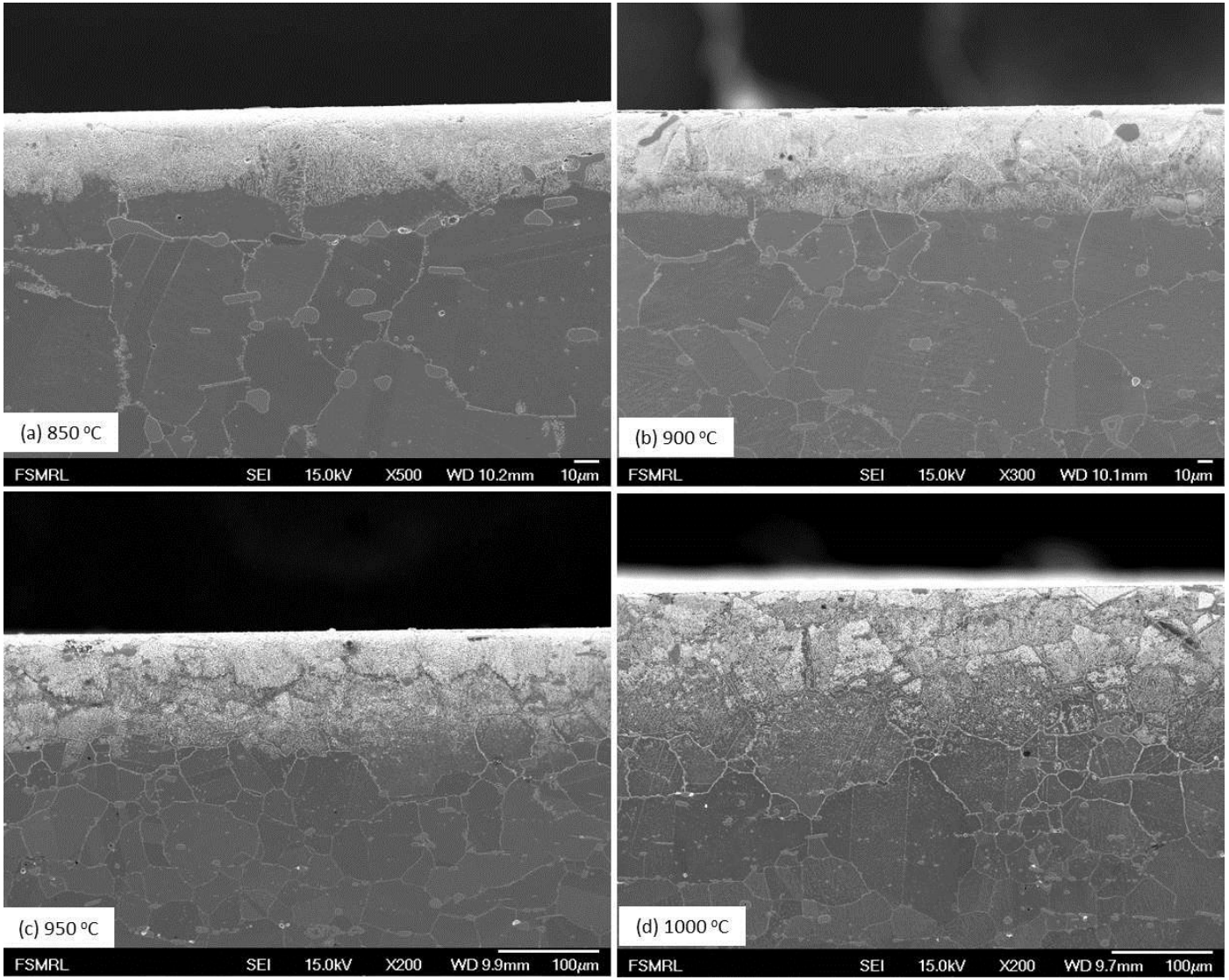

Fig. 4.31: Cross-sectional view of alloy 230 exposed to the carbonaceous environment.

4.2 Biaxial thermal creep

4.2.1 Biaxial creep behavior of alloy 617

The biaxial creep behavior of alloy 617 at 850 and 950^{o}C are plotted in Fig. 4.32 and 4.33, respectively. It can be seen that as the applied stress decreases, the rupture lifetime increases. In addition, the curves shows that a large tertiary part of creep deformation with insignificant exhibition of secondary creep regime. To illustrate the change in creep rate during the test, the creep strain-time curves were differentiated to obtain the creep strain rate using finite difference formula:

$$\dot{\varepsilon}(\bar{t}_n) = \frac{\varepsilon_{n+1} - \varepsilon_n}{t_{n+1} - t_n} \tag{4.5}$$

$$\bar{t}_n = \frac{t_{n+1} + t_n}{2} \tag{4.6}$$

where ε_{n+1} and ε_n represent the effective strain at the two consecutive exposure time t_{n+1} and t_n, respectively, and $\bar{t}_n$ is the average time between the two time intervals. The creep strain rate is plotted as a function of the average strain on a semi-log scale and shown in Fig. 4.34 (a) – (d) and Fig. 4.35 (a) – (e)at 850 and 950^{o}C, respectively. Alloy 617 exhibited a decreasing creep rate followed by a steady state creep rate and later increasing creep rate with increasing creep exposure time. It is noted that as higher stress applied, the steady state creep rate, stage II, is not a significant part of the deformation rates (Fig. 4.34 (a) and Fig. 4.35 (a)). As the applied stress decreases, the steady state creep becomes more distinct. Fig. 4.36 (a)-(e).and Fig. 4.37 (a)-(d) show the cross-section view of SEM images near fracture surface at 950 and 850^{o}C. Intergranular fracture was observed for all specimens.

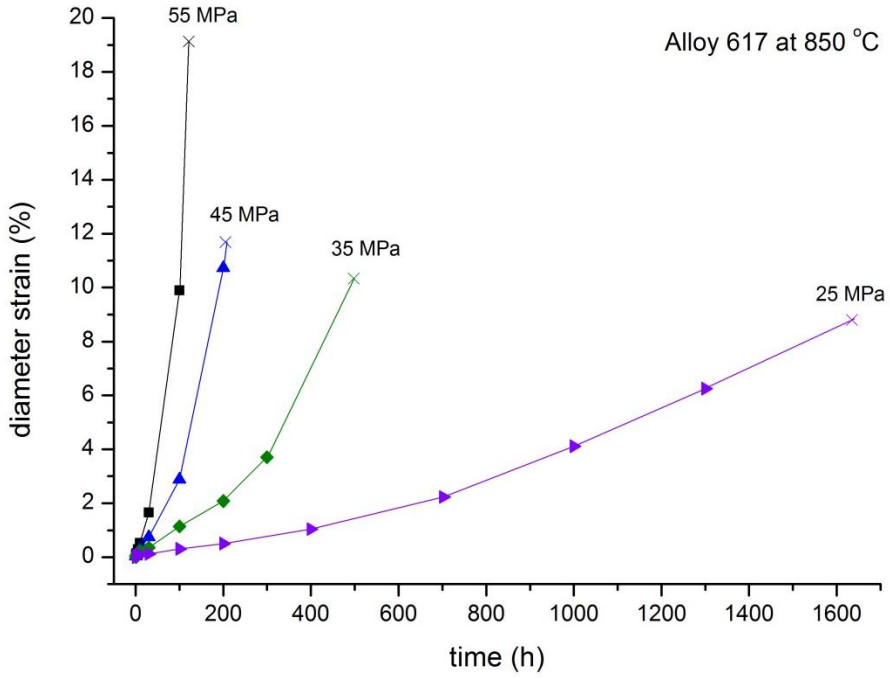

Fig. 4.32: Diameter strain vs. creep exposure time for alloy 617 at 850°C

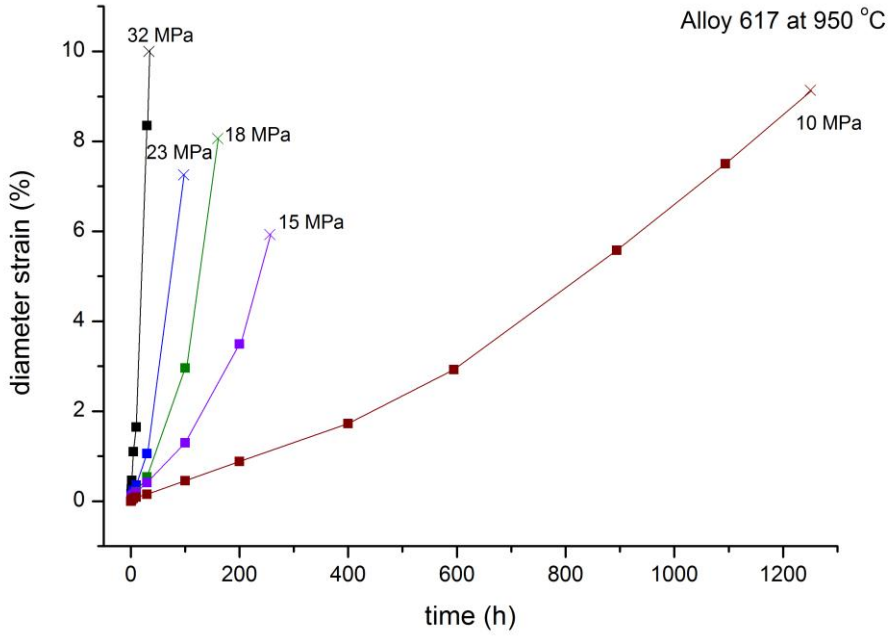

Fig. 4.33: Diameter strain vs. creep exposure time for alloy 617 at 950°C

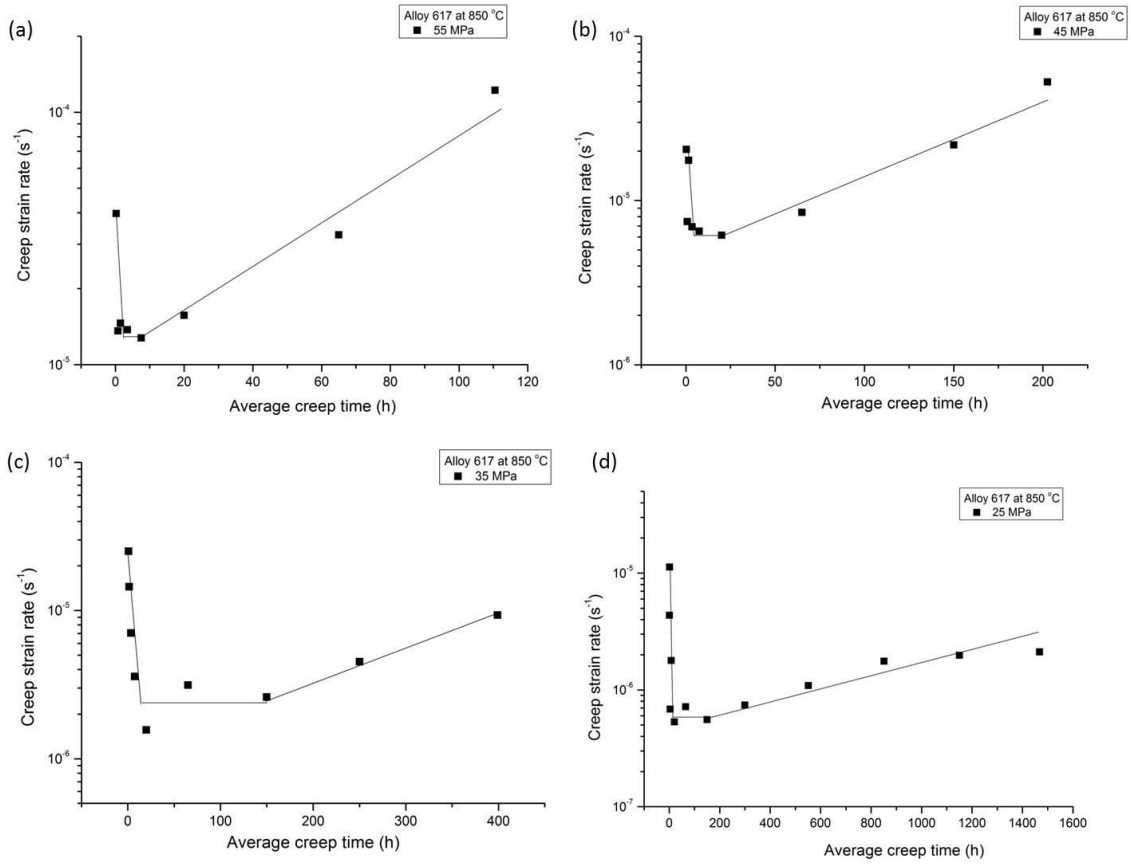

Fig. 4.34: Creep strain rate vs. average creep time for alloy 617 with applied stress of (a) 55 (b) 45 (c) 35 (d) 25 MPa at 850^{o}C

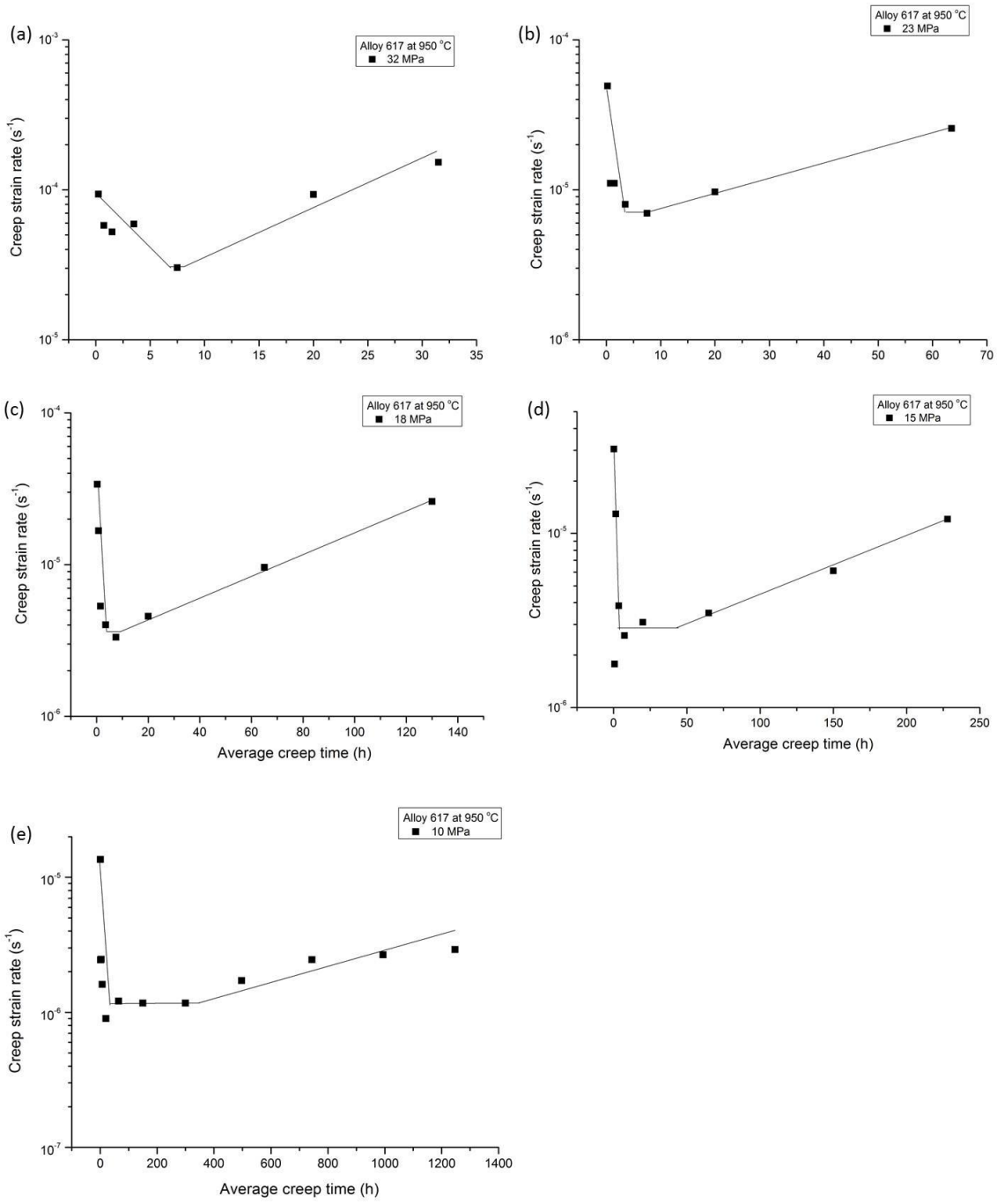

Fig. 4.35: Creep strain rate vs. average creep time for alloy 617 with applied stress of (a) 32 (b) 23 (c) 18 (d) 15 (e) 10 MPa at 950^{o}C

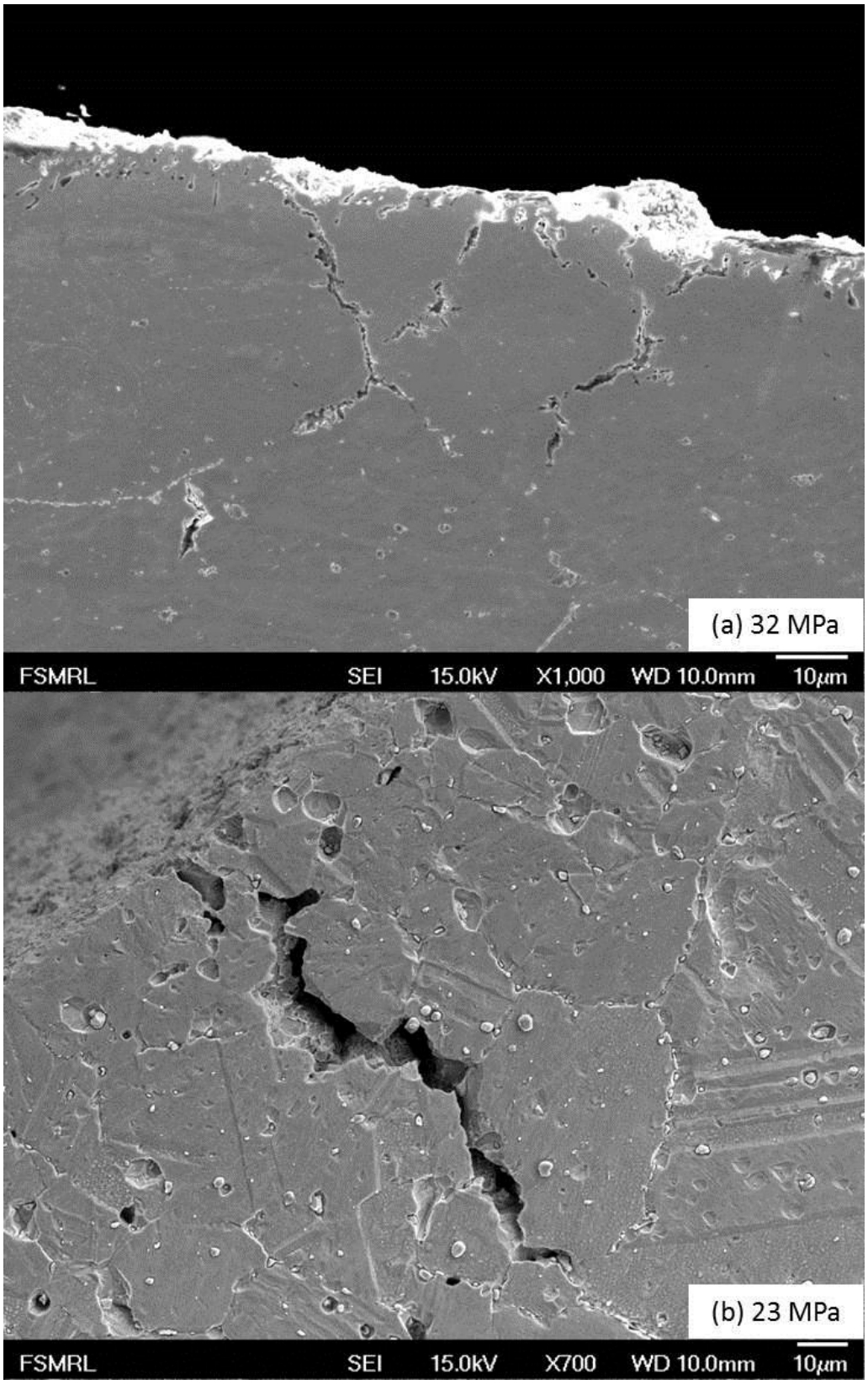

Fig. 4.36: Cross-sectional view of pressurized creep tubes near fracture surface under the applied stresses of (a) 32, (b) 23, (c) 18, (d) 15 (e) 10 MPa at 950^{o}C for alloy 617

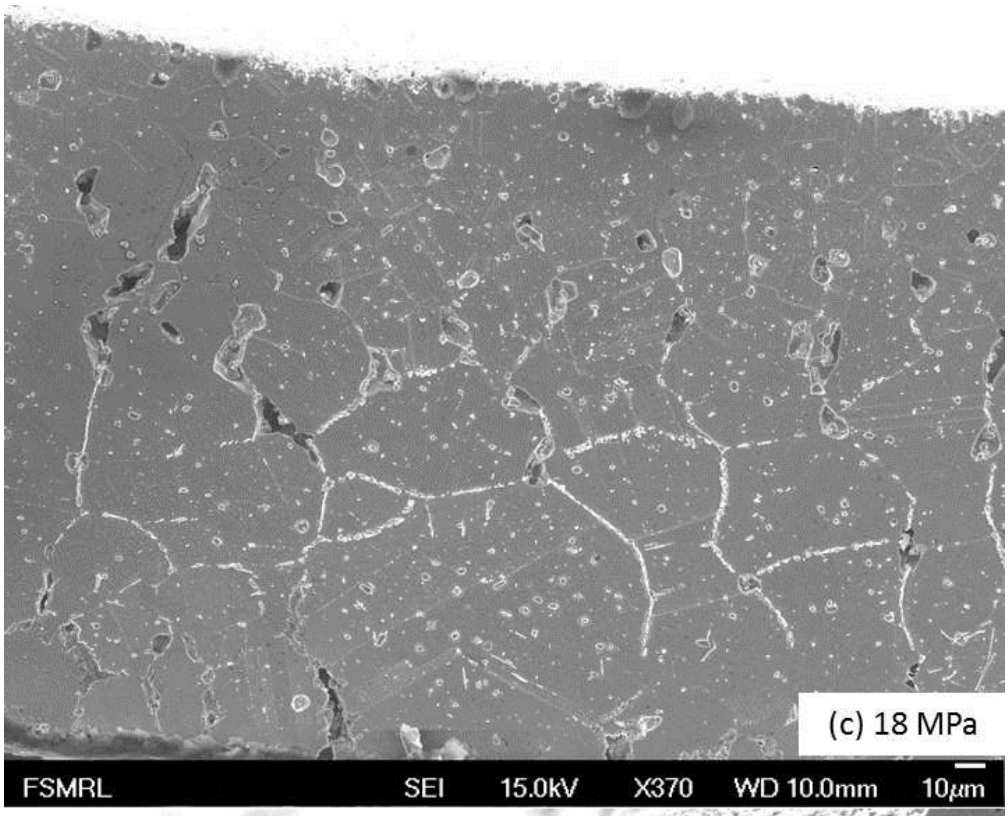
(c) 18 MPa
FSMRL SEI 15.0kV X370 WD 10.0mm 10μm

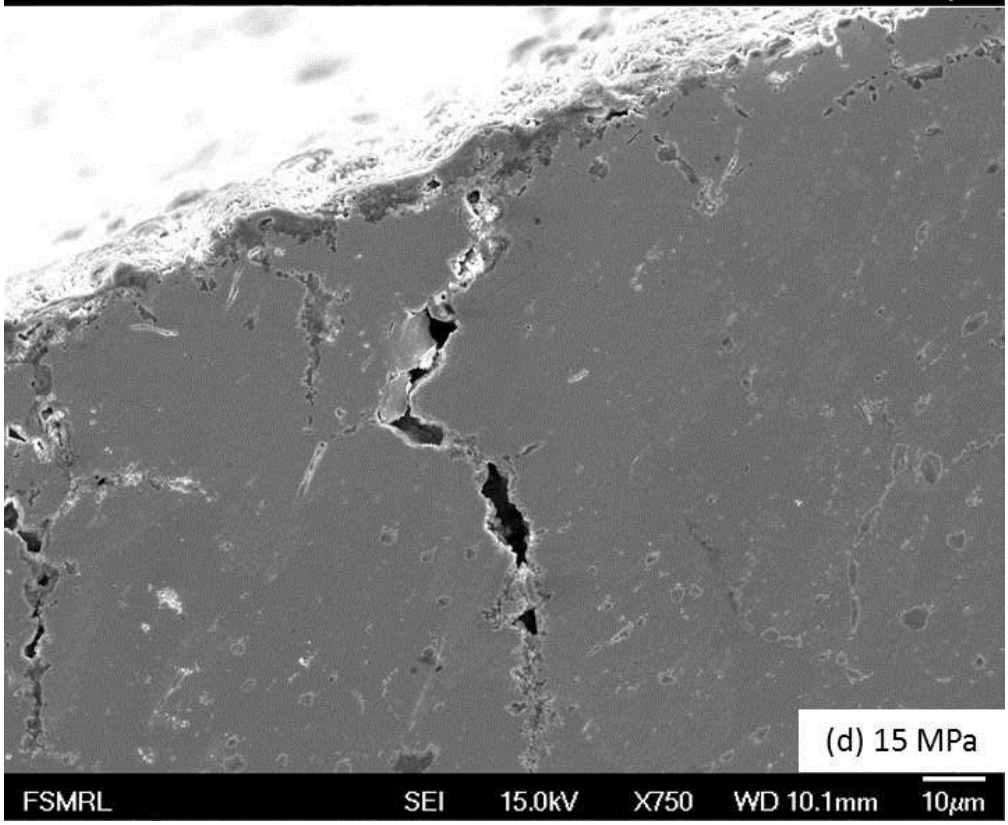
(d) 15 MPa
FSMRL SEI 15.0kV X750 WD 10.1mm 10μm

Fig. 4.36 (cont.)

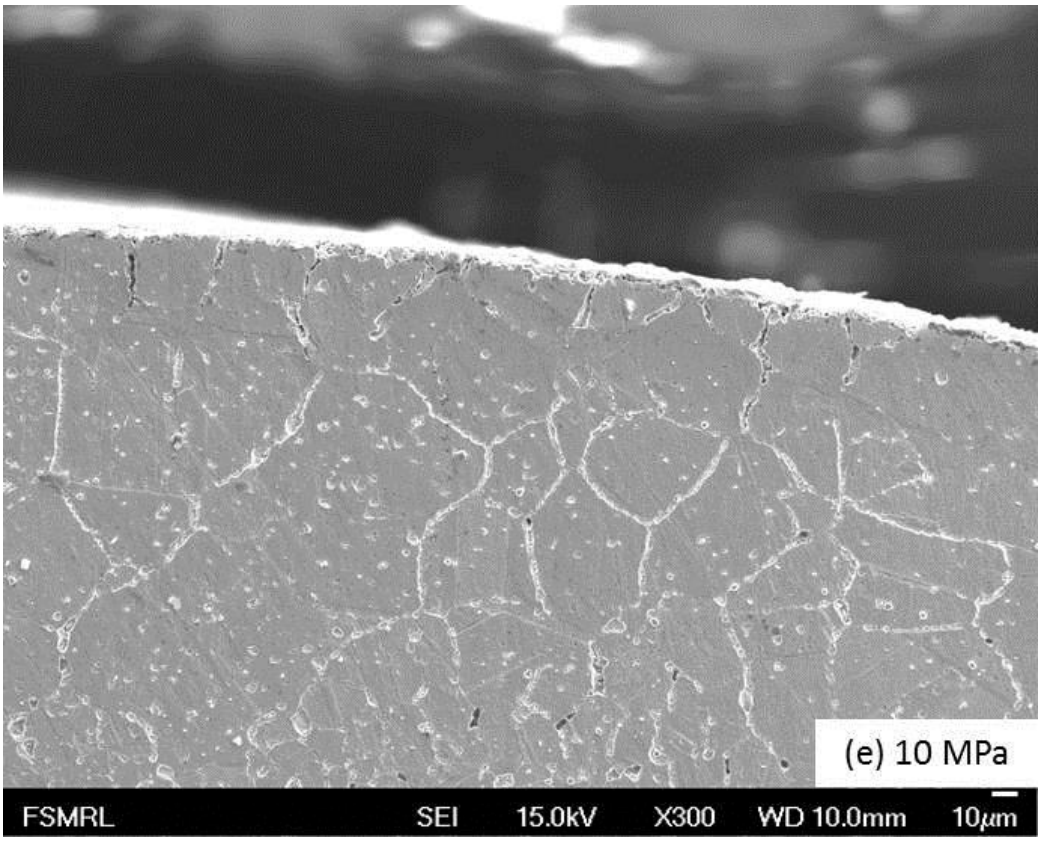

Fig. 4.36 (cont.)

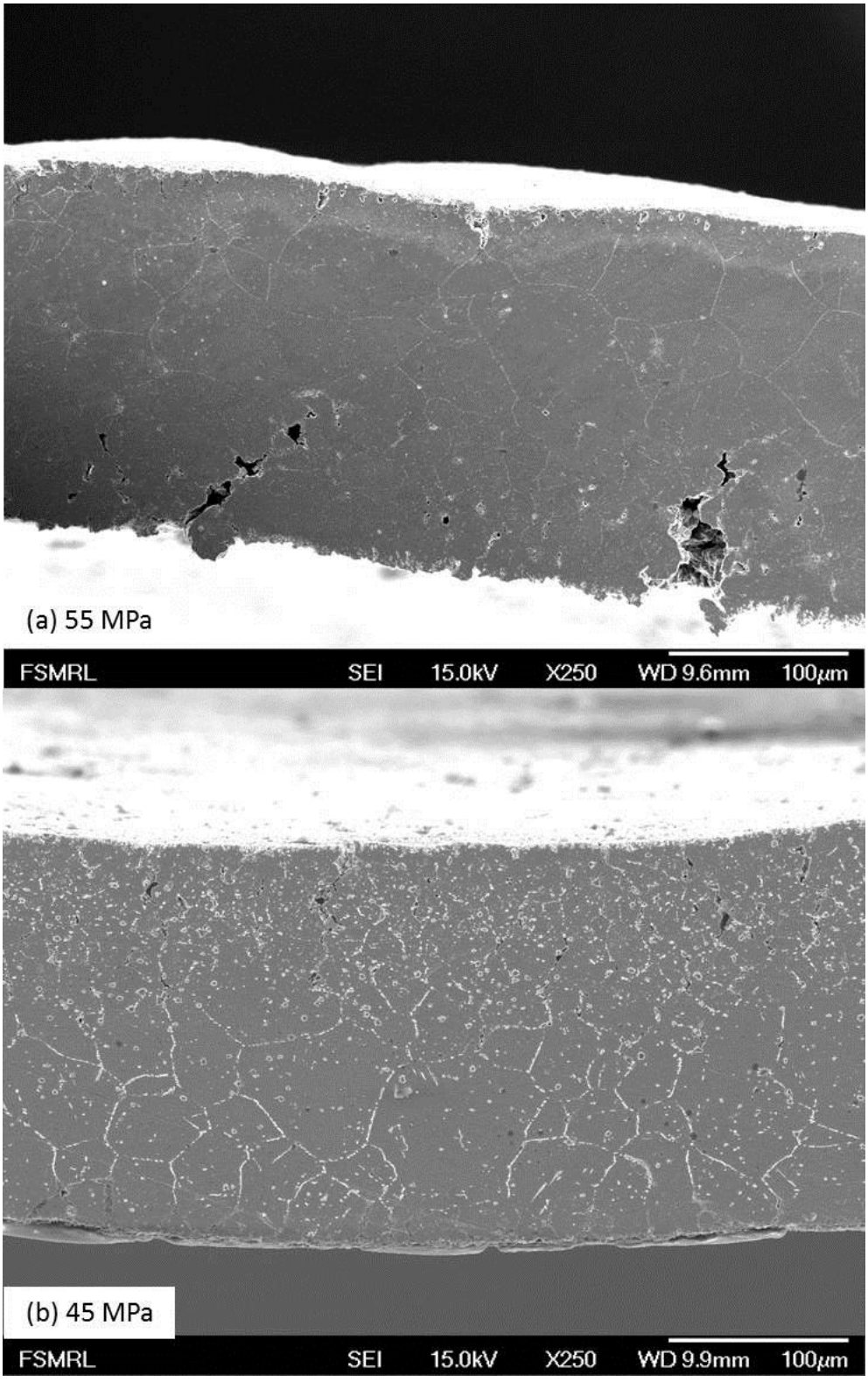

Fig. 4.37: Cross-sectional view of pressurized creep tubes near fracture surface under the applied stresses of (a) 55, (b) 45, (c) 35, (d) 25 (e) 10 MPa at 950^{o}C for alloy 617

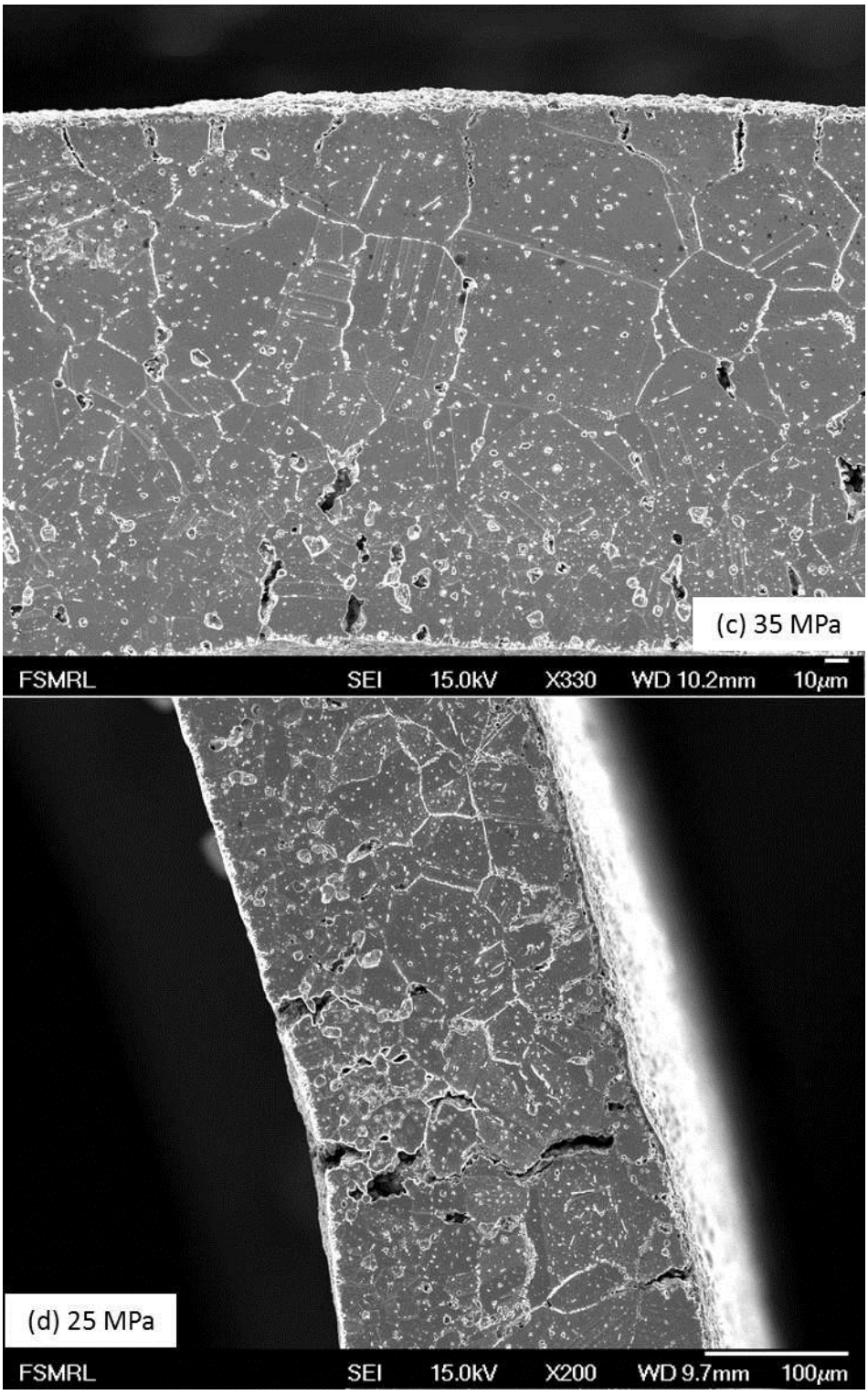
(c) 35 MPa
FSMRL SEI 15.0kV X330 WD 10.2mm 10μm
(d) 25 MPa
FSMRL SEI 15.0kV X200 WD 9.7mm 100μm

Fig. 4.37 (cont.)

4.2.2 Biaxial creep behavior of alloy 230

The biaxial creep behavior of alloy 230 at 850 and 950°C are plotted in Fig. 4.38 and 4.39, respectively. As the applied stress decreases, the rupture lifetime increases. In addition, at higher stresses applied, alloy 230 shows a large tertiary part of creep deformation with an insignificant secondary creep regime. At lower stresses, the appearance of secondary creep regime becomes more distinct (e.g. 35 MPa at 850°C). The creep strain-time curves were differentiated to obtain the creep strain rate using equation 4.5 and 4.6. The creep strain rate is plotted as a function of the average strain on a semi-log scale and shown in Fig. 4.40 (a)–(d) and Fig. 4.41 (a)–(e)at 850 and 950°C, respectively. Alloy 230 exhibited a decreasing creep rate followed by a steady state creep rate and later increasing creep rate with increasing creep exposure time. Fig. 4.42 (a) – (d) and Fig. 4.43 (a) – (d) shows the cross-section view of SEM images near fracture surface at 850 and 950°C. It can be seen that intergranular fracture was observed for all specimen testing conditions.

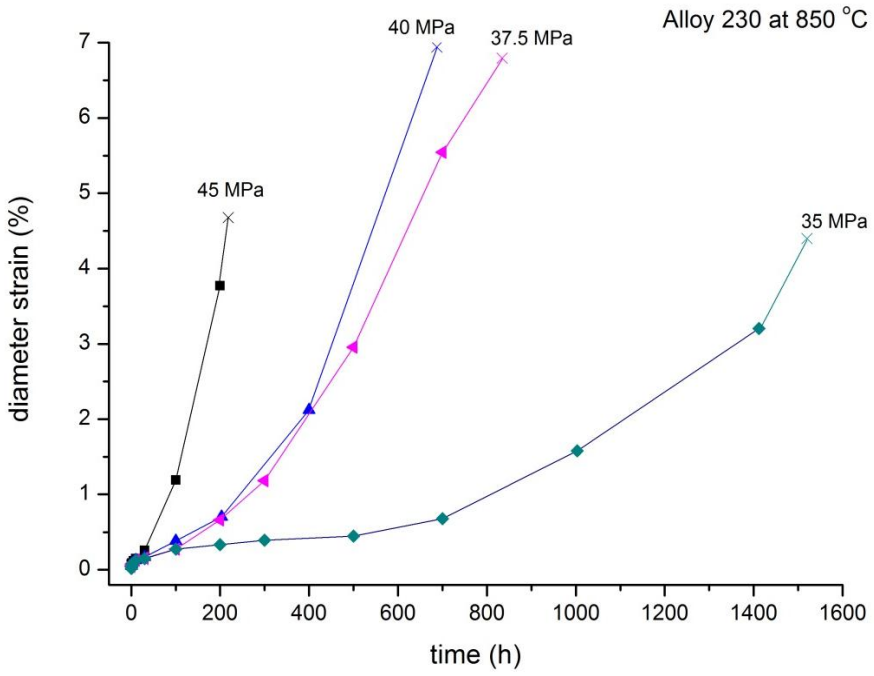

Fig. 4.38: Diameter strain vs. creep exposure time for alloy 230at 850°C

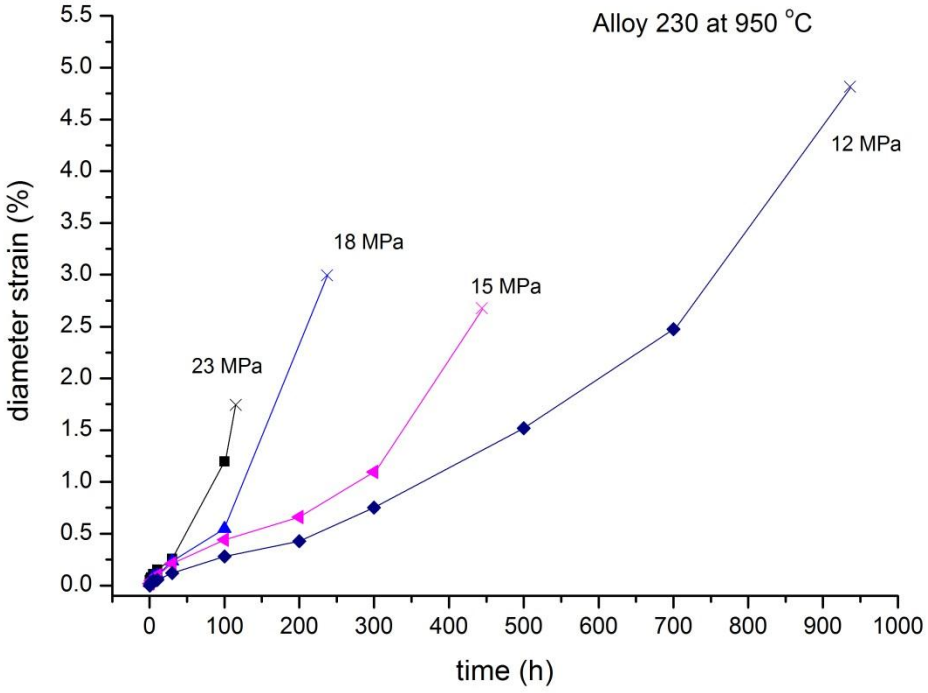

Fig. 4.39: Diameter strain vs. creep exposure time for alloy 230at 950°C

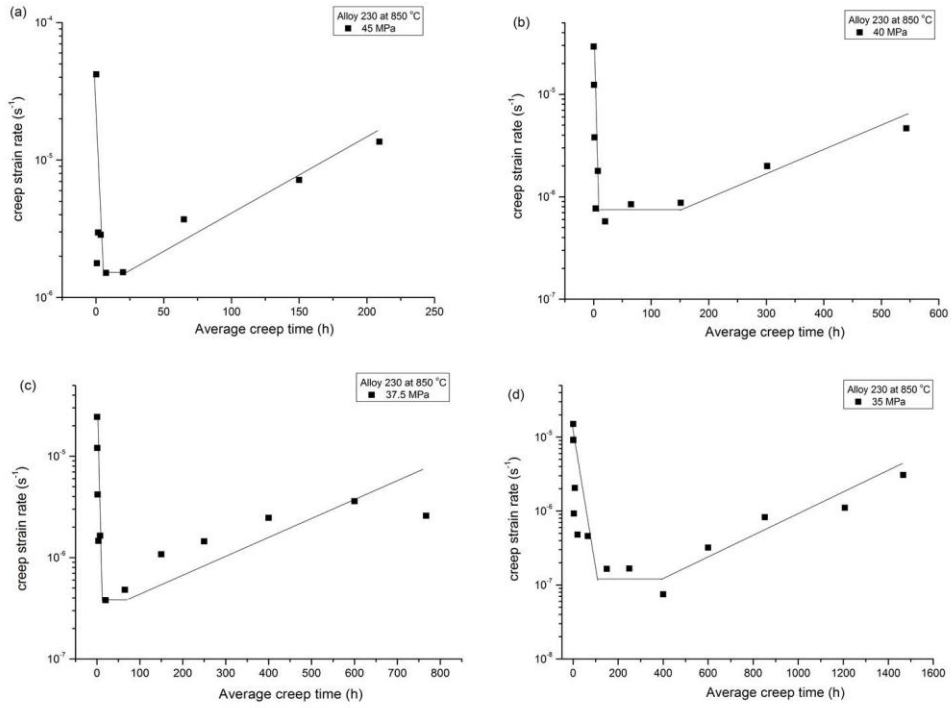

Fig. 4.40: Creep strain rate vs. average creep time for alloy 230 with applied stress of (a) 45 (b) 40 (c) 37.5 (d) 35 MPa at 850°C

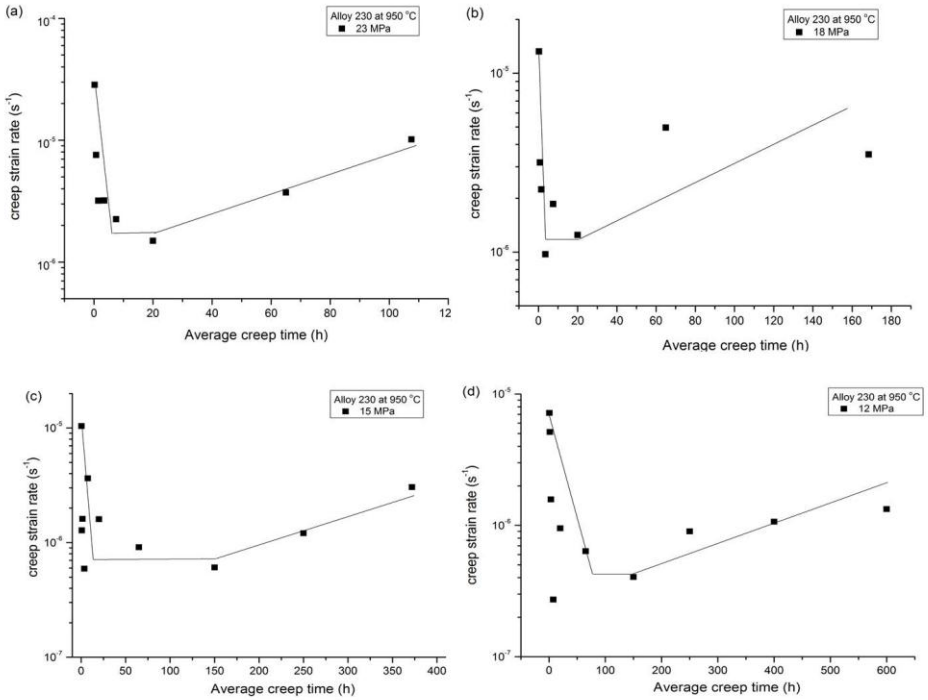

Fig. 4.41: Creep strain rate vs. average creep time for alloy 230 with applied stress of (a) 23 (b) 18 (c) 15 (d) 12 MPa at 950^{o}C

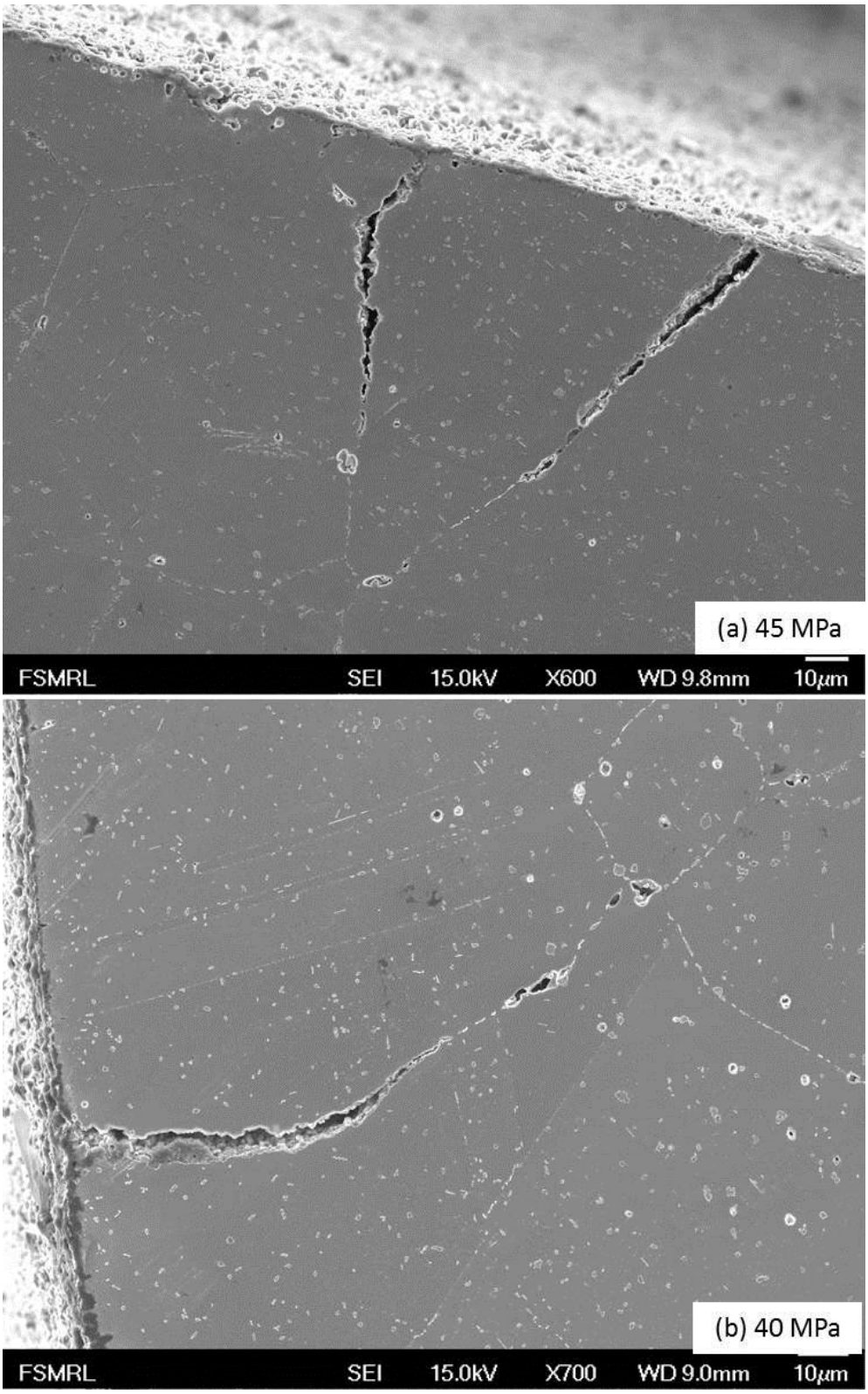

Fig. 4.42: Cross-sectional view of pressurized creep tubes near fracture surface under the applied stresses of (a) 45, (b) 40, (c) 37.5, (d) 35 MPa at 850^{o}C for alloy 230

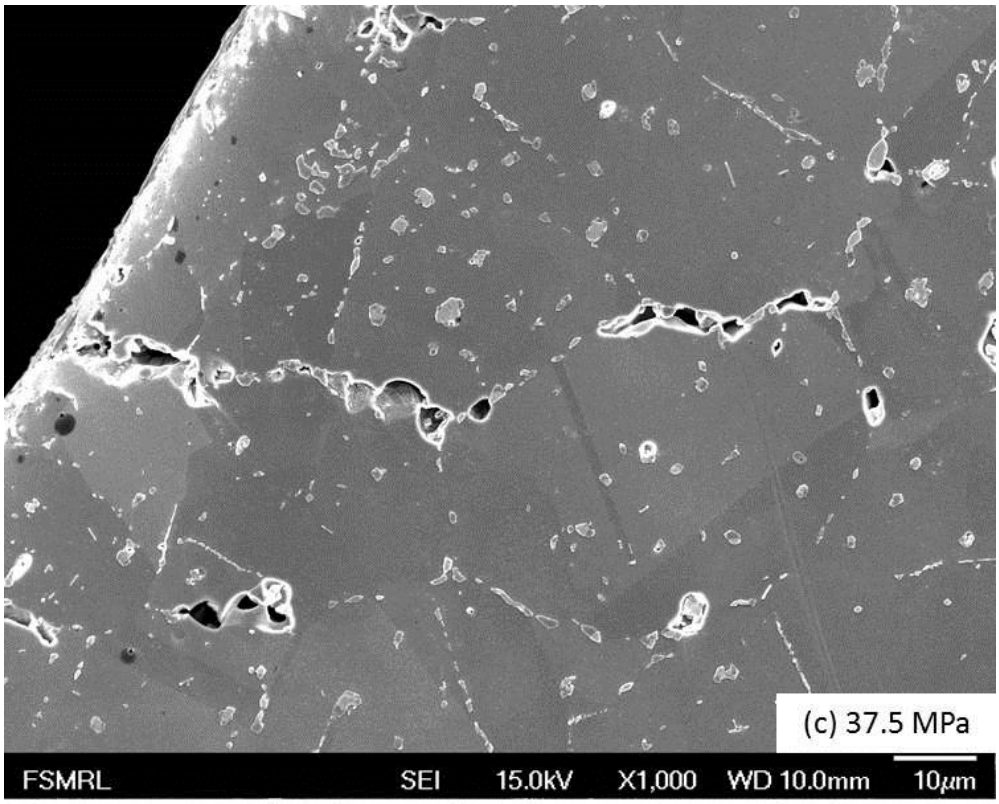
(c) 37.5 MPa
FSMRL SEI 15.0kV X1,000 WD 10.0mm 10μm

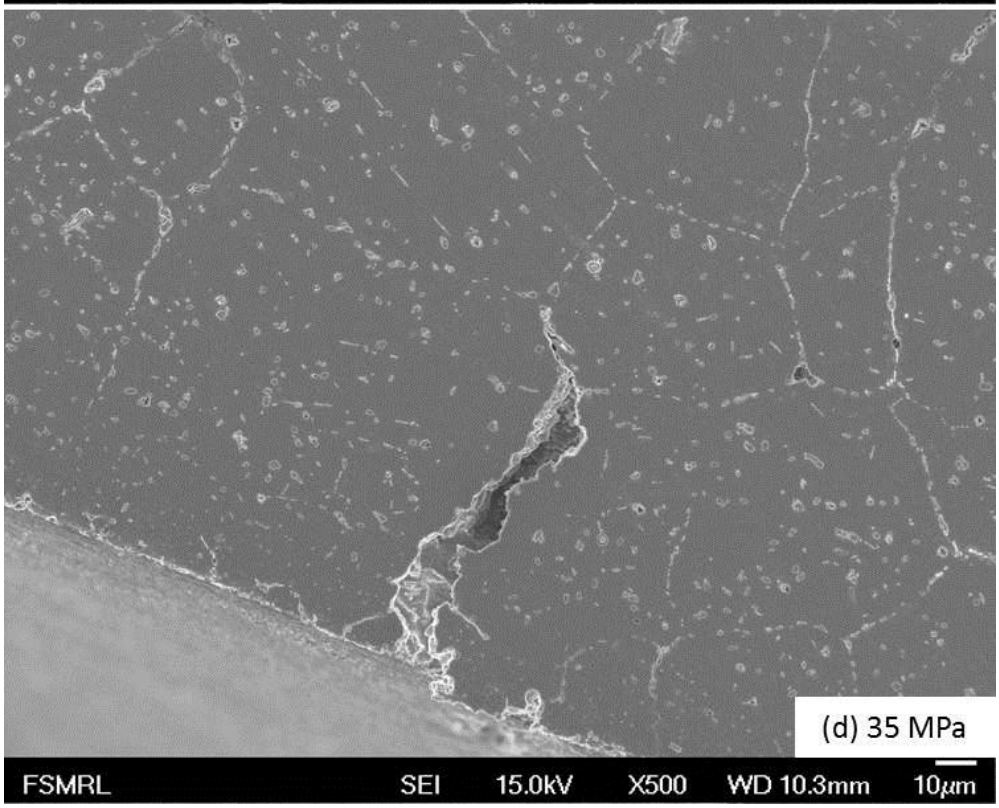
(d) 35 MPa
FSMRL SEI 15.0kV X500 WD 10.3mm 10μm

Fig. 4.42 (cont.)

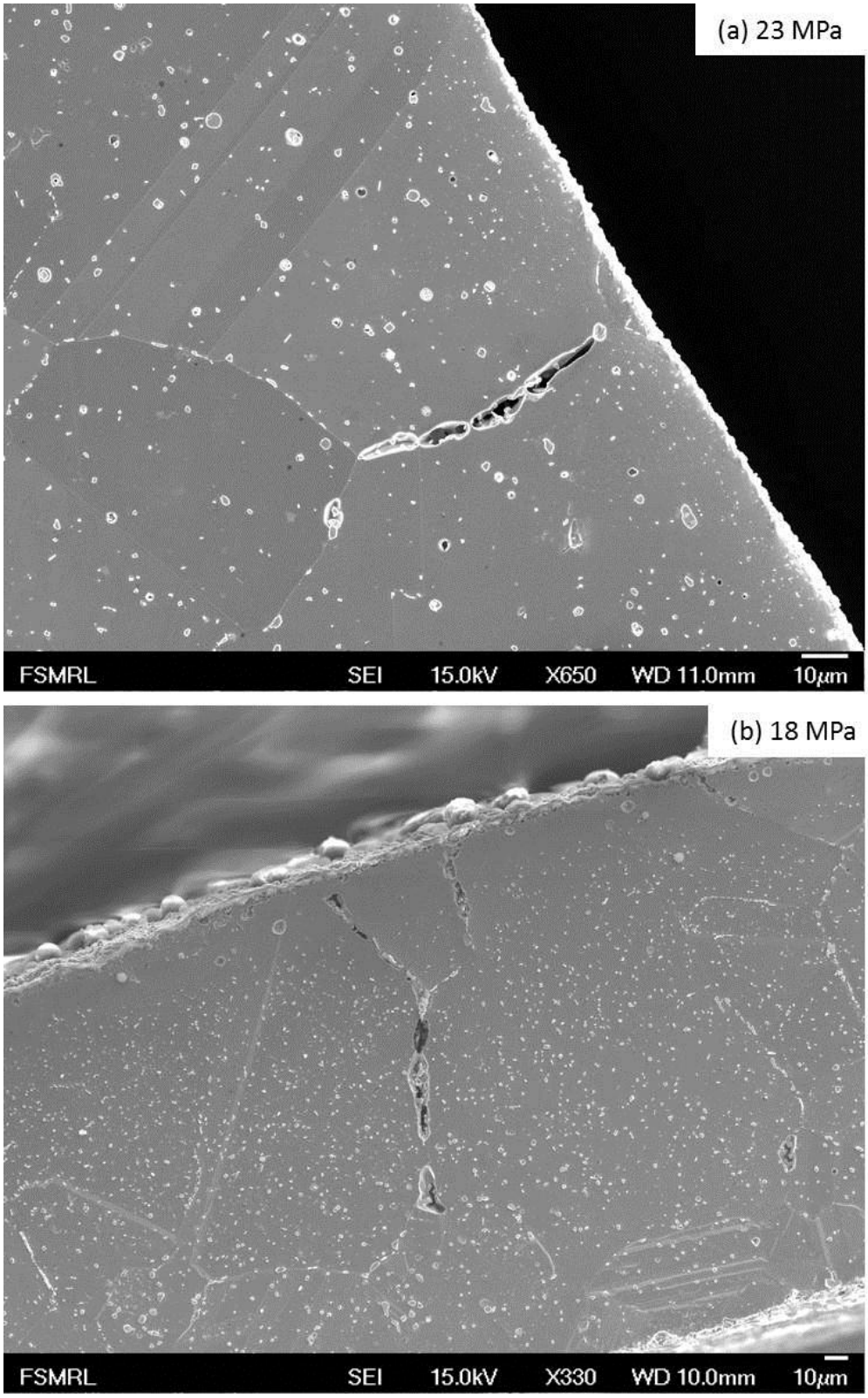

Fig. 4.43: Cross-sectional view of pressurized creep tubes near fracture surface under the applied stresses of (a) 23, (b) 18, (c) 15, (d) 12 MPa at 950^{o}C for alloy 230

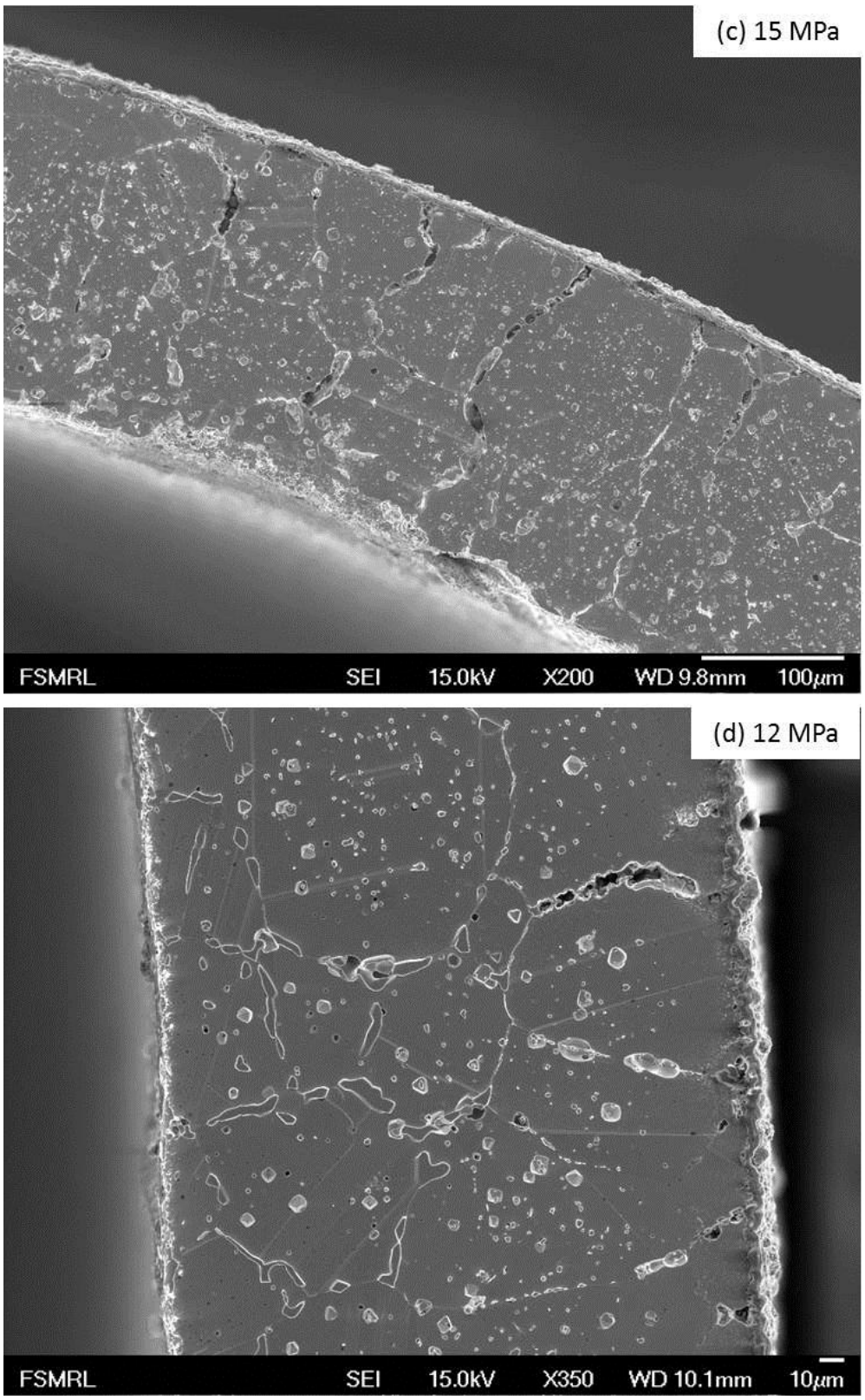
(c) 15 MPa
FSMRL SEI 15.0kV X200 WD 9.8mm 100μm
(d) 12 MPa
FSMRL SEI 15.0kV X350 WD 10.1mm 10μm

Fig. 4.43 (cont.)

CHAPTER 5

DISCUSSION

5.1 Short-term oxidation behavior of alloy 617

After the short-term oxidation tests, the oxide scale grown on alloy 617 is Cr_2O_3, which is indicated in Fig. 4.1. Previous studies [5.1,5.2] reported that not only Cr_2O_3 but also other oxides (e.g. NiO and $NiCr_2O_4$) were formed during the oxidation of alloy 617. However, Cr_2O_3 is the only oxide phase found during the incipient stage of oxidation of alloy 617. This suggests that the other oxides formed only during prolonged high temperature oxidation. In the long-term exposure, it is also found that the $NiCr_2O_4$ was formed on alloy 617.

It has been suggested in the literature [5.3] that the transport of Cr through Cr_2O_3 is controlling factor for the oxidation reaction where the reaction with oxygen occurs at the scale/gas interface. From the depth profile of the scale shown in Fig. 4.2, the oxygen levels indicate that the oxidation reaction occurs at or near the metal surface layer. To a first approximation, the diffusion distances of chromium and oxygen through a Cr_2O_3 layer can be approximated:

$$d \sim 2\sqrt{Dt} \qquad (5.1)$$

where d is the diffusion distance of the element, D is the diffusion coefficient of the diffusing elements in the Cr_2O_3, and t is oxidation time. For the specimen oxidized at 900^{o}C, $D_{Cr} = 8 \times 10^{-16}$ ($cm^2\ s^{-1}$) [16], $D_o = 8.1 \times 10^{-18}$ ($cm^2\ s^{-1}$) [17], and t = 3600 (s) can be used to approximate the diffusion lengths. The diffusion lengths of Cr and O are d_{Cr} = 83.1 nm and d_O = 8.3 nm, respectively. These calculated diffusion distances are significant smaller than the thickness of the scale obtained in the present study. The result suggests that the scale/gas may not be the location of the oxidation reaction. To further understand the region in which the oxidation reaction likely occurs, the morphology of the surface features of the scale are necessary. Fig. 5.1 displays the

surface morphology of the Cr_2O_3 tilted 30^o with respect to the surface normal. It clearly shows that many Cr_2O_3 crystals that are stacked together during the growth of the scale. The growing surface crystals are not continuously distributed to form a dense monolithic scale. It is noteworthy that there are small openings or pores between the crystals as they grow, indicating that the interface where the crystals contact one another contain small pores. This implies that, as two crystallites with their own facets grow together, the interfacial regions are not continuous and provide an active pathway for Cr and O transport. These results suggest that the occurrence of Cr–O oxidation reaction may be beneath the scale/gas interface during the growth of the scale.

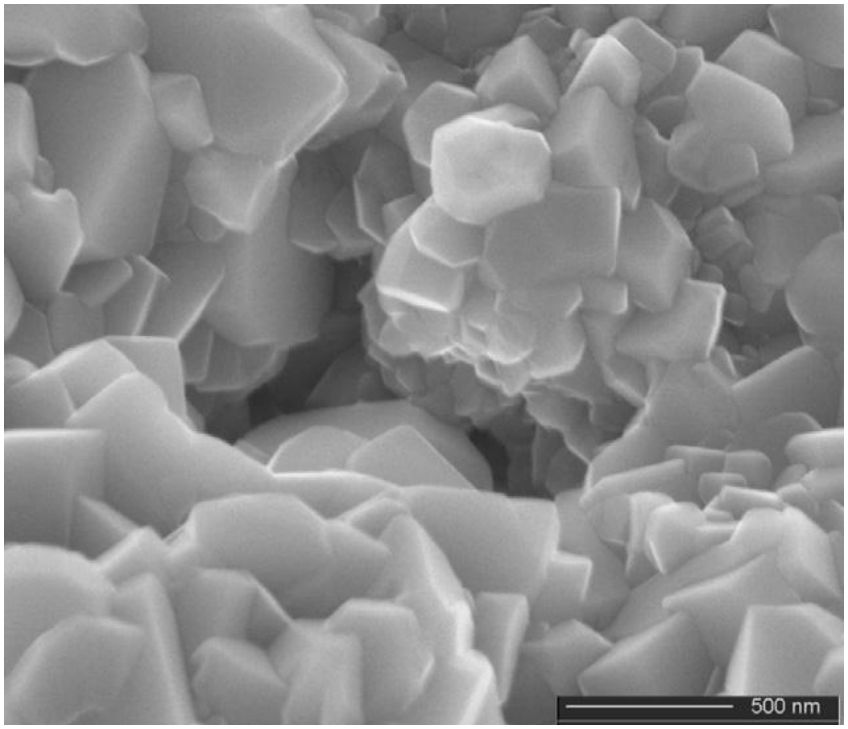

Fig. 5.1: Surface morphology of Cr_2O_3 grown at the temperature of 900^oC.

It was also found that concentration gradients for elemental nickel and cobalt are present within the chromia. The oxidation of chromium is dictated by the reaction of $2Cr_{(s)} + 3/2O_{2(g)} = Cr_2O_{3(s)}$. The standard free energies of formation of Cr_2O_3 at 850 and 1000^oC are given by [5.6]:

$$\Delta G^0_{Cr_2O_3}(1123K) = -830,530(J/mol) \qquad (5.2)$$

and

$$\Delta G^0_{Cr_2O_3}(1273K) = -791,830(J/mol) \quad (5.3)$$

Similarly, the oxidation of nickel and cobalt is dictated by the reaction of $Ni_{(s)} + 1/2O_{2(g)} = NiO_{(s)}$ and of $Co_{(s)} + 1/2O_{2(g)} = CoO_{(s)}$, respectively. The standard free energies of formation of NiO and CoO at the two temperatures are given by [5.6]:

$$\Delta G^0_{NiO}(1123K) = -139,680(J/mol) \quad (5.4)$$

and

$$\Delta G^0_{NiO}(1273K) = -127,030(J/mol) \quad (5.5)$$

and

$$\Delta G^0_{CoO}(1123K) = -154,490(J/mol) \quad (5.6)$$

and

$$\Delta G^0_{CoO}(1273K) = -143,890(J/mol) \quad (5.7)$$

It can be seen that Cr_2O_3 is thermodynamically stable with respect to the other two oxide phases and should be preferred as long as sufficient Cr is present to support the oxidation reaction. Therefore, no NiO or CoO formation is expected in the oxide, consistent with the GIXRD results.

The residual stress measurements show that the stress states are compressive. The measured residual stress originates from two sources: the intrinsic stress (grown-in stress) and the extrinsic stress (thermal stress). The thermal stress is due to the difference in thermal expansion coefficient between the scale and the substrate material, and can be formulated as [5.7]

$$\sigma_{th} = \frac{E}{1-\nu}(\alpha_{scale} - \alpha_{substrate})\Delta T \quad (5.8)$$

where E is the Young's modulus, m is the Poisson's ratio, α_{scale} and α_{alloy} are the thermal expansion coefficients of the scale and the substrate, respectively, and T is the temperature difference between the oxidation temperature and the temperature at which the stress is measured. In the present case, $E_{Cr_2O_3}$ = 138 GPa [5.8], $\nu_{Cr_2O_3}$ = 0.29 [5.9], $\alpha_{Cr_2O_3}$ =9.55x 10^{-6} K^{-1} [5.10], and

$\alpha_{alloy617}$ = 16.3x 10^{-6} K^{-1} [5.11] were used. Since the measurements were performed at 25°C, the calculated thermal stresses are -1.23, -1.31, -1.38 and -1.45 GPa for the specimens oxidized at 850, 900, 950 and 1000°C, respectively. The dash line plotted in Fig. 5.2 connects individual stress levels, which were calculated by subtracting the thermal stresses from the total residual stresses at the corresponding temperatures. The intrinsic stress states in the Cr_2O_3 scale were found to be tensile. Several models have been proposed [5.12,5.13] that attribute tensile stress observed in the beginning stages of polycrystalline film growth to crystallite coalescence. In the Nix–Clemens model [5.13], the change in free energy during crystallite coalescence due to the decrease in surface energy and the grain boundary energy is balanced by elastic strain energy.

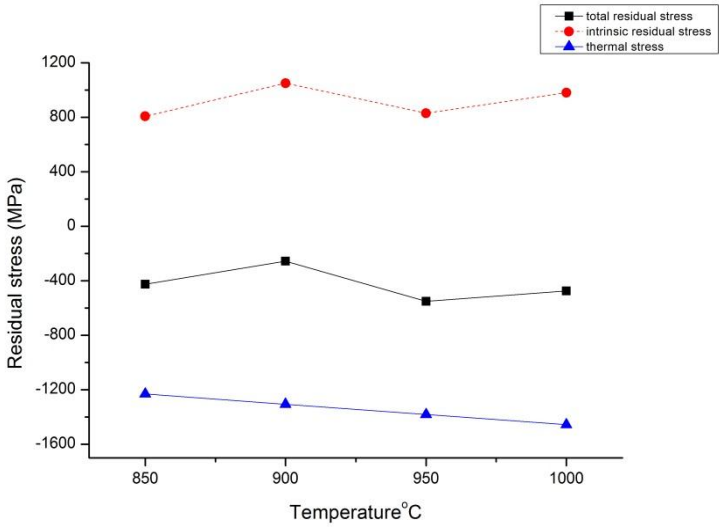

Fig. 5.2: The variation of total residual stress and the intrinsic residual stress of the Cr_2O_3 as a function of oxidation temperature. Note that the intrinsic residual stress is tensile.

In the present case, as shown in Fig. 5.2 and suggested in the above model, it is likely that during the incipient stage of oxidation, the grown-in tensile stresses may be associated with the point of crystallite coalescence, where the isolated crystallites grow and contact with each other to form a continuous scale. It is noted that the residual stresses of the alloy 617 at the scale/substrate interface decrease, as shown in Fig. 5.3. As shown in Fig. 4.3(a), it is observed that for the specimen oxidized at 850°C, the scale remains attached to the substrate with few voids or pores. However, Fig. 4.3 (b–d) shows that the amount of voids or pores increased with increasing oxidation temperature. These pores or voids may lead to the decrease in residual stress

of alloy 617 observed in the present study. The formation of the voids or pores may be associated with the Cr diffusion zone from which there is a flow of mass. The Cr near the substrate surface reacting with oxygen atoms are supplied by the flow of Cr within the substrate. It is likely that, due to the difference in diffusion rate of Cr in Cr_2O_3 and in the substrate, the loss of Cr near scale/substrate interface might not be fully compensated with the flow of Cr within the substrate, thereby leaving the pores or voids inside the substrate.

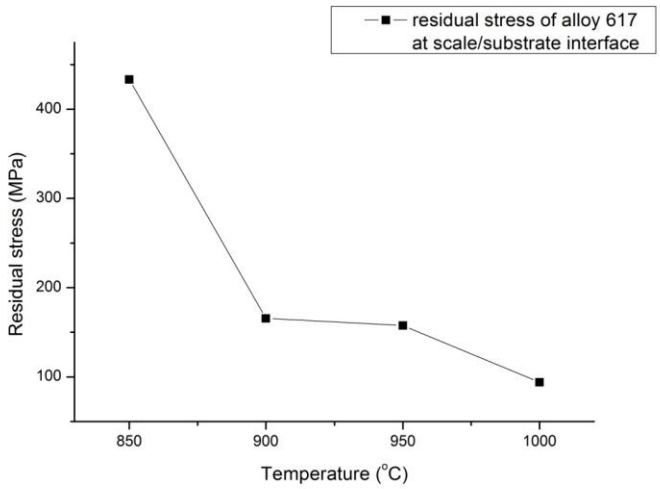

Fig. 5.3: The variation of residual stress of alloy 617 measured at scale/substrate interface.

Oxidation kinetics represented by the weight gain shows that a two-stage oxidation process exists, and each stage follows a parabolic law of oxidation. The activation energy of the first and second stages are 271.2 and 318 (KJ/mol), respectively. According to Wagner's theory, the high-temperature parabolic oxidation rate signifies that the oxidation rate of the alloy is determined by the diffusion of ions migrating through a dense oxide layer. It was reported that the activation energy for chromium ions in chromia ranges from 240 kJ/mol [5.14] to 280 kJ/mol [5.15]. In the present study, the activation energy for the first stage is around 271.2 kJ/mol, in good agreement with the activation energy reported above. In the stage II oxidation, the activation energy changed from 271.2 kJ/mol to 318 kJ/mol. The activation energy for the stage II oxidation is in reasonable agreement with that for the chromium ions in Fe–Cr–Ni alloys (309 ± 11 kJ/mol) [5.16]. Therefore, it implies that, during the first stage of oxidation, transport of the surface chromium ions through incipient chromia controls the oxide formation process. The second stage

of oxidation is then controlled by additional chromium ions diffusing out of the substrate through the Cr-depleted layer to meet the oxide scale boundary.

5.2 Short-term oxidation behavior of alloy 230

Fig. 4.8 shows that there are two oxide phases in the scale grown on alloy 230. To examine the distribution of the two oxide phases, compositional depth profiles of the oxidized specimens were acquired using AES. Two representative AES spectra are shown in Fig. 5.4 (a) and (b). The results indicated that Cr and Mn are distributed nearly uniformly throughout the oxide scales following oxidation. The microstructures of the scales, shown in Fig. 4.9(a)–(d), show a homogeneous oxide layer grown on the substrate. No significant distinction can be made for the separation of the two oxide phases. The results of GIXRD, AES and the microstructure suggest that the two oxide phases mix randomly with each other and are uniformly distributed throughout the scale. It is noted that for all specimens, the scale grown on the substrate is dense and maintains good adhesion at the interface over the entire temperature range (Fig. 4.9(a)–(d)). This should provide good oxidation resistance for alloy 230 over this range of application temperatures.

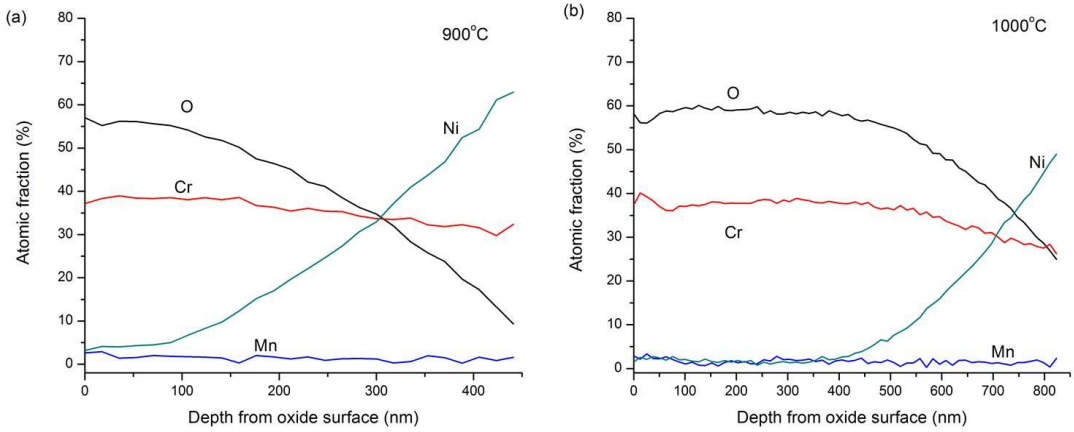

Fig. 5.4: Typical AES compositional depth profiles of the oxide layer grown at (a) 900 ◦C and (b) 1000°C.

The amount of Mn measured by AES ranged from 1.9 to 3.3 at% for all the specimens. The results obtained by XRD and XPS were used to further confirm the atomic concentrations of Mn.

Using XRD, the concentration of Mn can be determined by the fraction of $MnCr_2O_4$ divided by the atomic ratio of Mn with respect to the Cr and O in the $MnCr_2O_4$. The calculations show that the amount of Mn ranges from 2.0 to 2.6 at%. It is assumed that all $MnCr_2O_4$ is present as crystalline phase in the calculation. Using XPS, the concentration of Mn can be calculated by the deconvolution of the Cr $2p_{1/2}$ and $2p_{3/2}$ peaks with respect to the different binding energies of Cr in Cr_2O_3 and $MnCr_2O_4$. The ratio of $MnCr_2O_4$ in the oxide can be obtained, and then divided by the atomic ratio of Mn in $MnCr_2O_4$. The results showed that the concentration of Mn is between 2.6 and 3.4 at%. In this analysis, it is assumed that all Mn atoms are bonded in the spinel-type phase. Therefore, the concentration of Mn for all the oxidized specimens should fall within the interval of 1.9 to 3.4 at% based on the consistency of measurements using three independent experimental analyses.

Oxidation kinetics shows that the activation energy of the first and second stage are 246.5 and 212.1 (KJ/mol), respectively. According to Wagner's theory, a parabolic oxidation rate indicates that diffusion of ions passing through a dense oxide layer is a rate-determining step, and the rate constant is related to the mobility or diffusion coefficients of ions. As stated previous, it was reported that the activation energy for chromium ions in chromia is 240 kJ/mol [5.14]. In the present study, it was found that the activation energy at the first stage is 246.5 kJ/mol, which is in good agreement with the data given above. Based on thermodynamics, it has been shown [5.17] that the free energy of formation of $MnCr_2O_4$ is more negative than that of Cr_2O_3. Therefore, $MnCr_2O_4$ is more stable phase than Cr_2O_3. In the present work, however, the activation energy obtained (246.5 kJ/mol) for the first stage close to the published data (240 kJ/mol) may imply that the oxidation kinetics of the first stage is mainly controlled by formation of Cr_2O_3. This may be attributed to the Mn content (0.46 wt%), which is much lower than Cr content (21.7 wt%). The small concentration of Mn or an insignificant growth of $MnCr_2O_4$ at the very beginning stages of oxidation may not be able to influence the resulting oxidation kinetics. During the second stage, due to higher diffusivity of the Mn ions compared with that of the Cr ions in Cr_2O_3 [5.4], more Mn ions were provided from the substrate and more $MnCr_2O_4$ could form. It is likely that the presence of the two phases (Cr_2O_3 and $MnCr_2O_4$) may be the main cause of the lower activation energy of 212.1 kJ/mol and the reduction of the oxidation rate in the second stage.

In summary, Fig. 5.5 schematically illustrates the formation of a mixed oxide layer morphology of Haynes 230 during incipient oxidation. At the oxidation stage I, the main oxidation reaction is formation of Cr_2O_3, supported by the activation energy and insufficient Mn content on the surface. As the oxidizing specimens pass through the transition period (Fig. 4.12), the growth of $MnCr_2O4$ phase becomes significance, and the $MnCr_2O_4$ is uniformly distributed within the oxide layer.

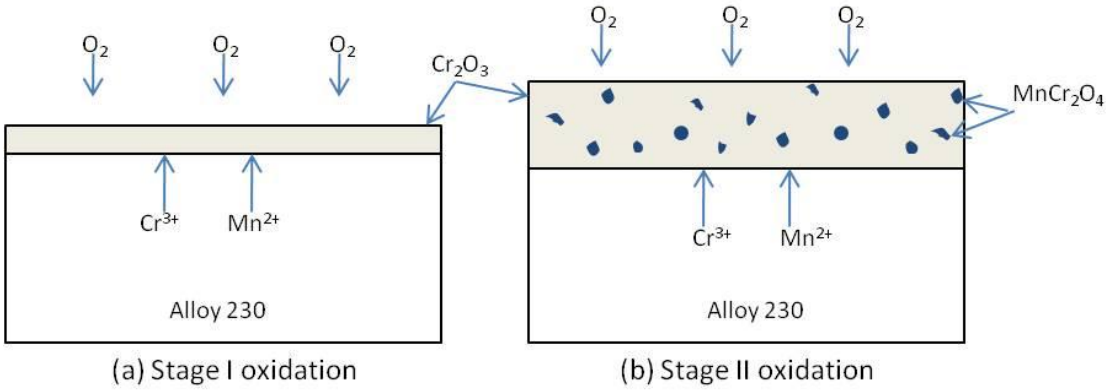

Fig. 5.5: Schematic illustration of oxidation behavior of alloy 230.

Residual stresses measurements showed that the measured residual stress is compressive. Similar to the discussion of the residual stress development in section 5.1, the intrinsic residual stress of the scale grown on the substrate can be calculated by subtracting the thermal stress from the measured stresses. The intrinsic stresses for all the specimens are highly tensile, ranging from 648.9 to 1308.4 MPa, as shown in Fig. 5.6. The intrinsic tensile residual stress can be explained via crystal growth based on energy considerations, which is discussed in section 5.1. Furthermore, it is noted that the intrinsic residual stress increased with increasing oxidation temperature (Fig. 5.6). This increase may be a result of the greater grain boundary area at higher oxidation rate. Fig. 5.7 depicts that the total residual stresses of alloy 230 near the scale/substrate interface and the total residual stresses of the chromia. The stress state of alloy 230 is tensile, whereas the stress state of chromia is compressive. Both the oxide and the substrate show a decrease in the magnitude of the stresses with increasing oxidation temperatures. This may be an indication of the increase in rate at which the substrate can accommodate residual stresses through stress relaxation processes as the temperature increases.

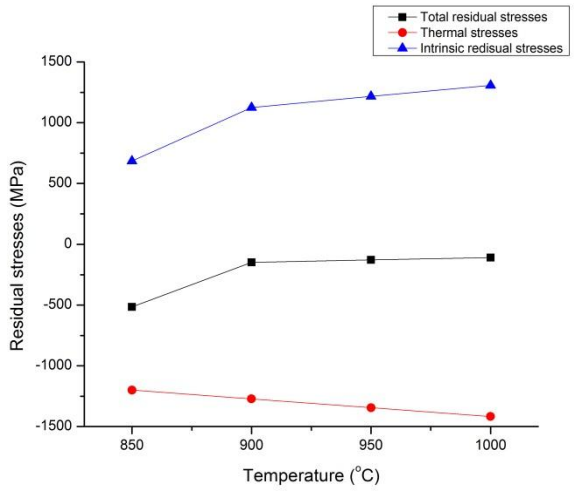

Fig. 5.6: The variation of total residual stress, thermal stress and the intrinsic residual stress of the Cr_2O_3 as a function of oxidation temperature.

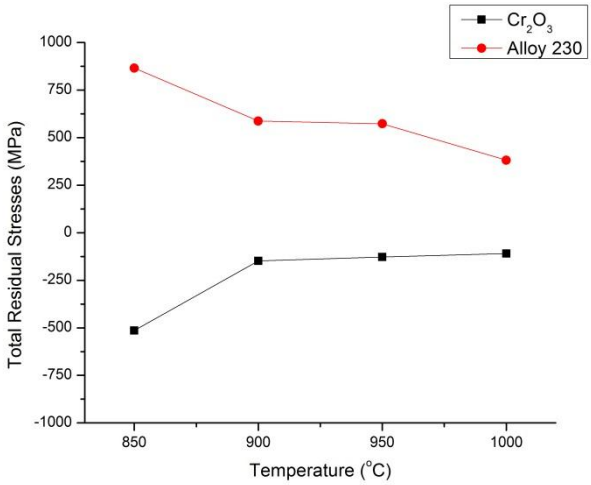

Fig. 5.7: The total residual stresses of Cr_2O_3 and alloy 230 as a function of oxidation temperatures.

5.3 Long-term oxidation behavior of alloy 617 and alloy 230 at 950^{o}C

After long-term exposure in the air environment, the surface oxide scale of alloy 617 at 950^{o}C shows that the oxide phase was initially chromia. After 360 h exposure, the appearance of diffraction peak of $NiCr_2O_4$, which is a spinel phase, becomes distinct and two oxide phases (Cr_2O_3 + $NiCr_2O_4$) are present thereafter. This is evidenced by X-ray diffraction (Fig.4.14(a)). In addition, Table 4.5 indicates that the rate constant ($K = 8.18 \times 10^{-13}$) is higher than that obtained in the second stage from TGA results ($K_{(2)} = 7.28 \times 10^{-13}$) at the same exposure temperature.

The formation of Cr_2O_3 grown on high temperature alloys has been generally observed as the chromium content of the alloys is high enough (usually ≥ 20 wt%). The growth rate of the Cr_2O_3 is related to the diffusion of Cr from the alloy to the oxide scale. In the present study, the initial oxidation was controlled by chromium uphill diffusion (Fig. 4.2). With increasing exposure time, the formation of Cr_2O_3 requires continuous supply of chromium diffusing from the substrate. Therefore, the outward diffusion of Cr may cause local depletion of chromium in the alloy near the oxide scale, as suggested in Fig. 4.2. After the long-term exposure, it is likely that the Cr-depleted region is developed and the diffusion of chromium from the substrate across the Cr-depleted regime cannot promptly reach the scale/alloy surface to preferentially react with oxygen to form Cr_2O_3. Therefore, the Ni element that exists in the Cr-depleted region may participate in the oxidation reaction forming the $NiCr_2O_4$ in the present case. Furthermore, it has been observed [5.18] that for the Ni-30%Cr alloy exposed to air at high temperatures, the oxide phase was solely Cr_2O_3. As for Ni-20%Cr alloy, formation of NiO, $NiCr_2O_4$ and Cr_2O_3 were observed [5.18]. This indicates that chromium content in Ni-Cr base alloys affects the formation of oxide phases within the scale. It was also suggested that the local concentration of Cr of alloy 617 affects the formation of oxide phases [5.1]. It is noted that the oxidation rate ($K = 8.18 \times 10^{-13}$) after long-term exposure is higher than that obtained in short-term testing ($K_{(2)} = 7.28 \times 10^{-13}$). This could be attributed to the formation of $NiCr_2O_4$ where oxygen can react with Ni leading to the weight increase.

It was reported [2.33] that after 1000 h exposure in air at 900^{o}C, multiple layers of oxide was observed with NiO on the outermost surface and isolated $NiCr_2O_4$ below and relatively thick

Cr_2O_3 beneath Ni-containing layers. To investigate the relative position of Cr_2O_3 and $NiCr_2O_4$, the results of GIXRD was used with different incident angles. Fig. 5.8 shows that the results of GIXRD with an incident angle of 2, 4 and 6 degree for the specimen oxidized after 360 h exposure. It can be seen that the diffraction peaks of Cr_2O_3 and $NiCr_2O_4$ are present with an incident angle of 2 degrees, which suggests that the two phases are present in the very shallow layer of the oxide scale. With increasing incident angle, the relative integrated intensities of Cr_2O_3 and $NiCr_2O_4$ are increased. This suggests that the formation of $NiCr_2O_4$ is distributed throughout the Cr2O3 oxide scale in the present study. From Fig. 4.2, it is noted that there is a diffusion zone of nickel and chromium where nickel element are present in the Cr_2O_3. This also implies the readily formation of $NiCr_2O_4$ as long as the chromium concentration is low enough.

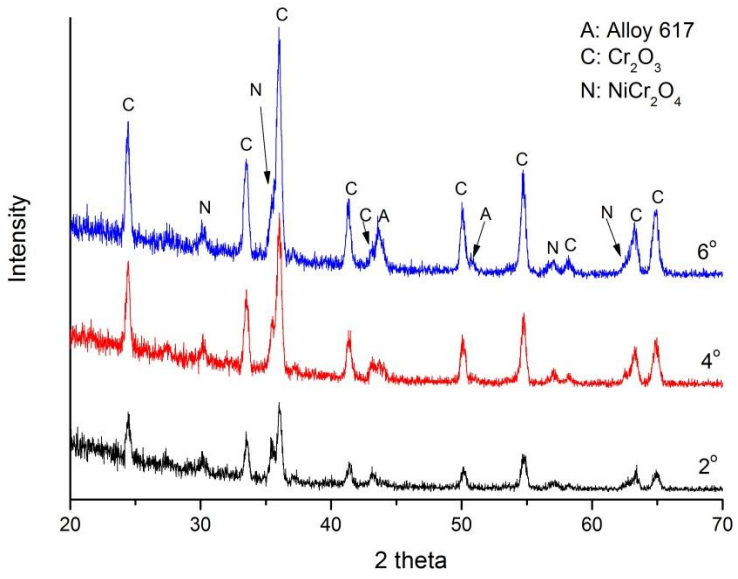

Fig. 5.8: X-ray diffraction of oxide scale with incident angle of 2^o, 4^o, and 6^o for alloy 617 after 360 h exposure.

As for alloy 230 exposed to the same condition, the oxidation rate is significant lower than that of alloy 617. The may be attributed to the rapid formation of $MnCr_2O_4$, which is discussed in section 5.2. Contrast to the oxidation behavior of alloy 617 at 950^oC, alloy 230 exhibits relatively continuous weight gain at 950^oC and there is no significant spallation observed after 1512 h exposure. The linear fitting of the oxidation rate constant is shown in Fig. 5.9. The correlation

coefficient (R^2) of the fitting is 95.3 %, which indicates that parabolic law is strictly obeyed. The phase ratio of $MnCr_2O_4$ over the entire oxide scale can be calculated using equation (4.4). Fig. 5.10 shows that the ratio of $MnCr_2O_4$ initially increases significantly up to an oxidation time of 720 h and then reaches a nearly constant value thereafter.

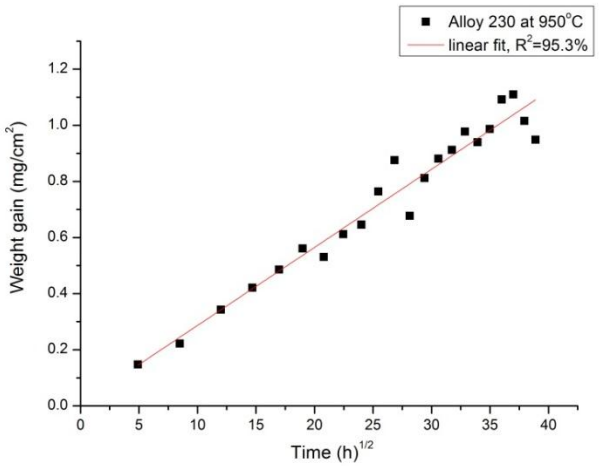

Fig. 5.9: Weight gain as a function of time for alloy 230 oxidized at 950°C. The correlation coefficient is 95.3%.

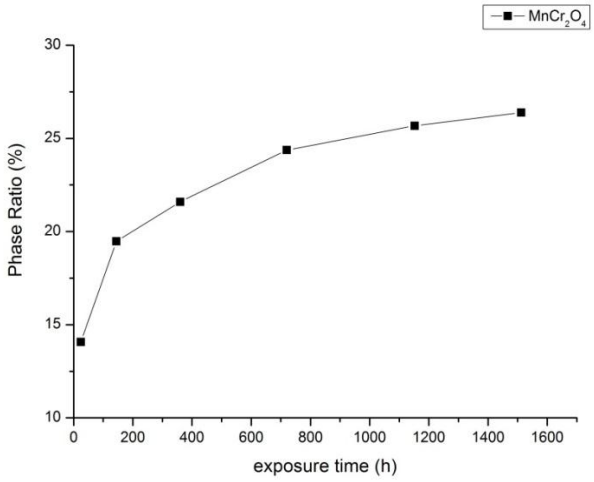

Fig. 5.10: $MnCr_2O_4$ phase ratio in oxide scale for alloy 230 at 950°C

5.4 Short-term corrosion behavior of alloy 617 and alloy 230 under a He + 5% H_2 environment

The measured oxygen partial pressures at 850 and 950°C are 2 x 10^{-21} and 6 x 10^{-19} atm in the low-pO_2 gas, which is summarized in Table 5.1. Table 5.1 also shows that the equilibrium partial pressures for the formation of $NiCr_2O_4$, $MnCr_2O_4$ and Cr_2O_3, indicating that these phases are thermodynamically stable in the environment.

Table 5.1: Equilibrium oxygen partial pressure for formation of Cr_2O_3, $MnCr_2O_4$ and $NiCr_2O_4$ and measured oxygen partial pressure

Temperature (°C)	Equilibrium Po_2 for Cr_2O_3 formation (atm)	Equilibrium Po_2 for $MnCr_2O_4$ formation (atm)	Equilibrium Po_2 for $NiCr_2O_4$ formation (atm)	Measured Po_2 (atm)
950	$1*10^{-23}$	$2.8*10^{-24}$	$9.3*10^{-21}$	$6*10^{-19}$
850	$1.6*10^{-26}$	$4*10^{-27}$	$2.6*10^{-23}$	$2*10^{-21}$

For alloy 617 exposed to the low-pO_2 gas, the weigh change from 850 to 950°C initially decreases and finally increases, whereas at 1000°C, the weight initially decreases and levels off (Fig.4.18 (a)). From the XRD results shown in Fig. 4.19 (a), Cr_2O_3 scale still formed on the alloy 617, suggesting that a dynamic reaction concerning the loss of the elements from the substrate and uptake of oxygen from the atmosphere was established during the incipient exposure. It can be seen that after 6 h exposure, the weight increased again for the 850 to 950°C exposures and the weight of alloy 617 at 1000 °C no longer decreased. Cross-sectional views of the microstructures cut from FIB (Fig. 4.20) show that a layer of Cr_2O_3 was grown on the alloy 617. The oxide layer was formed rapidly, which may act as a barrier to avoid the loss of the elements from the substrate. This is reflected by the weight increase.

For the alloy 230 exposed to the environment, at 850 and 900°C, the decrease in the weight is significant initially and then reaches a stable region where the loss of weight is very small. The weight loss increases to a greater extent as the temperature increases from 950 to 1000°C, compared with the stable region at 850 and 900°C (Fig.4.18 (b)). Figure 5.11 shows the amount

of weight loss at the four temperatures after 6 h exposure. It suggests that the rate of weight loss increases as the temperature increases. It was reported [5.19] that the decrease in the weight may be attributed to the loss of carbon or other decarburization phenomena. However, the result of ICP-ME shows that the solution contained nickel of 1.86 μg/L from the quartz tube holder. This demonstrates that the weight loss results from not only loss of carbon but also loss of nickel in the present study. The likely mechanism for the loss of nickel can be determined by plotting the vapor pressure of nickel vs. temperature, which is shown in Fig. 5.12. The data are plotted along with vapor pressures for elemental Cr and W. The trends in the vapor pressures suggest that the loss of nickel increases as the temperature increases. Table 5.1 shows the Cr_2O_3 and $MnCr_2O_4$ are thermodynamically stable in these environments. It should also be noted that NiO is not thermodynamically stable at these oxygen partial pressures.

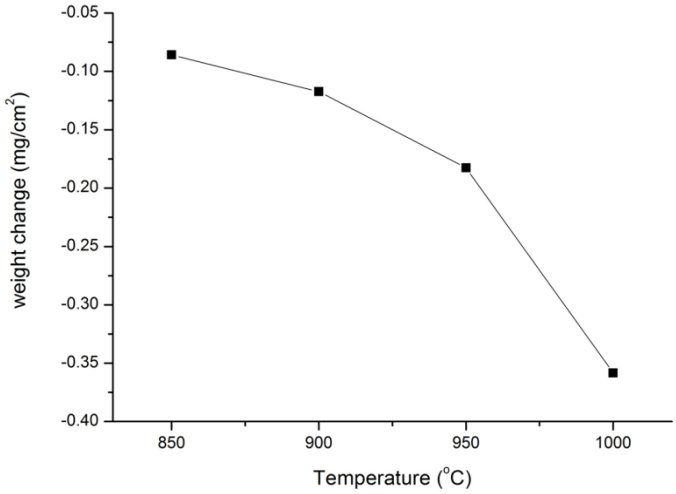

Fig. 5.11: The amount of weight loss after 6 hours exposure from 850 to 1000^{o}C.

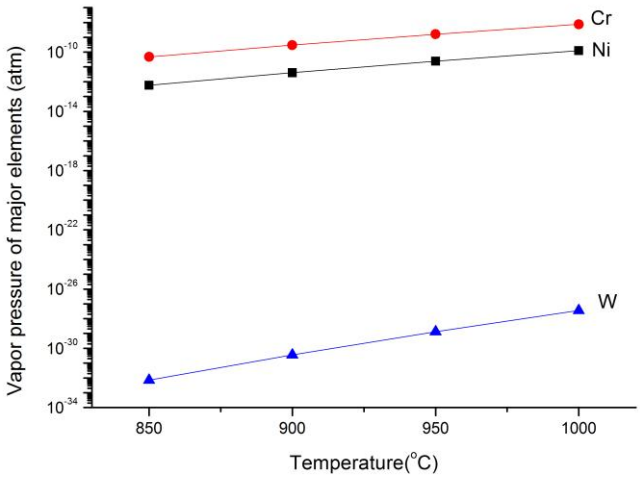

Fig. 5.12: Vapor pressure of major elements in alloy 230 for the entire exposure temperature.

Figure 4.21 (a)-(d) shows the cross-sectional view of microstructures of the scales. A homogeneous oxide layer grown on the alloy 230 was observed. The scale maintains good adhesion at the interface over the entire temperature range. It is noted that the thickness of the scale increases with increasing exposure temperature. Figure 4.21 (e) shows a typical surface morphology of the oxide at 950^{o}C, demonstrating that there are small slits or openings between the growing surface crystals under these oxidation conditions. The two contrasting results are found in the present study. On the one hand, the results of TGA show that the weight decreases during the entire exposure period at all four temperatures, and the rate of the weight loss increases with increasing exposure temperature. On the other hand, the GIXRD results and the measurements of the oxygen partial pressure suggest that the two oxide phases, Cr_2O_3 and $MnCr_2O_4$, are stable, and form during the exposure to the He + 5% H_2 environment at elevated temperatures. These contrasting findings imply that a dynamic process was established during the initial stages of the corrosion process. The oxidation reactions with Cr and Mn lead to an increase in the weight of alloy 230. Meantime, the loss of nickel in the environment, observed from the result of ICP-ME, contributes to a weight loss. The overall effect is that the weight decreases. It is very likely that the weight loss may be due to the diffusion of nickel and carbon through the oxide scale. Also, as suggested by Fig. 4.21 (e) and (f), the scale was observed to form with small openings or pores on which nickel element was detected. These results suggest that the scale may not be able to act as an effective diffusion barrier during the incipient

corrosion process. Furthermore, both the thickness of the scale and the amount of weight loss increased with increasing temperature (Fig. 4.21(a)-(d) and Fig. 5.11). It is found that, despite the thicker oxide scale formed at higher temperatures, the weight loss was still more aggressive and the thicker scale was actually less effective in retarding the amount of weight loss in the incipient corrosion testing.

5.5 Comparison of growth kinetics and microstructures in air and low-pO_2 gas

After long-term exposure under the He + 5% H_2 environment, the weight of alloy 617 increased with increasing exposure time (Fig.4.23 (a)). The weight gain follows parabolic law, which implies that the rate-controlling step is diffusion of ions migrating through a dense oxide layer. After long-term exposure, the microstructures shown in Fig. 4.24 (a) indicates that the oxide scale consists of Cr_2O_3 and $MnCr_2O_4$, which is different from the phases obtained in the case of air environment. Therefore, it is worthwhile to understand the difference regarding the kinetics and the microstructures between the two environments.

Fig. 5.13 shows the weight gain as a function time for alloy 617 and alloy 230 in the two different environments. For alloy 617, it is noted that the oxidation rate in the reducing environment (He+5% H_2) is higher than in air. The rate constants are summarized in Table 5.2. The reducing environment (low-pO_2 gas) produces an increase in oxidation rate around a factor of 2 compared with the air environment. Furthermore, the weight gain in the reducing environment is relatively stable, whereas there is significant spallation in air environment after 1224 h exposure. To understand the difference, microstructure of the thermally grown oxide for the two environments is necessary. Fig. 5.14 (a) and (b) shows the surface morphology of the oxide between air and low-pO_2 gas, respectively. It clearly shows that there is significant difference in grain size between the oxides. In the air environment, larges grains are observed, whereas extremely fine grains are formed in the low-pO_2 gas. The much finer grain size of the oxide grown in the low-pO_2 gas could provide a greater contribution to mass transport by grain boundary diffusion. It has been experimentally found [5.19] that a faster growth rate of chromia-forming alloys in Ar- 4%H_2 - 7% H_2O is observed, compared to the rate in Ar-20% O_2. It is

suggested [5.19] that inward oxygen grain boundary diffusion is the main cause for the increased growth rate. In the present case, if the higher growth rate mainly comes from the outward diffusion of chromium, more significant pores or voids in the alloy near the scale are expected to be observed in the low-pO_2 gas, as were observed in the air environment. Fig. 5.15 (a) and (b) shows the cross-sectional view of the two scales obtained after 6 h exposure at 1000^{o}C. There are few or no significant pores observed in the low-pO_2 gas compared with in the air. It is likely that the oxygen inward diffusion via grain boundaries contributed substantially to the overall oxide scale growth in the low-pO_2 gas. Furthermore, it is noted that the $MnCr_2O_4$ phase appears after 144 h exposure in the low-pO_2 gas, whereas the $NiCr_2O_4$ phase appears in the air environment (after 360 h exposure). In the present case, it is believed that significant amount of oxygen inward diffusion together with diffusion of Mn and Cr along grain boundary may lead to the formation of $MnCr_2O_4$. In contrast to low-pO_2 gas, $NiCr_2O_4$ was formed in the air environment, which is related to Cr-depleted regime (or Cr outward diffusion), as discussed in Sec. 5.3.

In the present study, the effect of H_2 is to react with oxygen producing low pO_2 gas by the following equation: $H_{2(g)} + 1/2\ O_{2(g)} = H_2O_{(g)}$, and therefore, the effect of $H_2O_{(g)}$ (or $H_{2(g)}$) on the grain size of the scale is of importance. The detailed mechanism for the formation of these extremely small grains in the low-pO_2 gas is still unclear. On the one hand, it was proposed [5.21,5.22] that that the presence of water vapor could interact with grain size. One interpretation is that the H_2O may retard the movement of the oxide grain boundaries and thus grain growth. As a result, extremely small grains are observed, and thus, increase the rate of the oxide growth. On the other hand, another likely mechanism is that the faster growth rate is more related the hydroxyl ions being transport through grain boundaries [5.23]. The occurrence of smaller grains is related to the nucleation process, which might be more easily occur than growth of existing grains in the low-pO_2 gas.

For alloy 230 exposed to the low-pO_2 gas, the weight gain follows the parabolic law, suggesting that the scale growth is controlled by solid-sate diffusion. Compared with the short-term exposure where the weight decrease is obtained, the increase in weight with increasing exposure time suggests that the scale may effectively cover the alloy surface with thicker scale. Therefore, a protective layer is formed. The surface morphology shows that extremely fine grains are grown on the alloy, which is similar to the case of alloy 617 in the same environment. It is noted that the growth rate of the oxide is decreased by a factor of 2 in the low-pO_2 gas

compared with the air, which is different from the case of alloy 617 (Fig. 5.13). Similar result has been reported for Ni-Cr base alloys [5.19]. However, no definite mechanism has been established so far to account for the decrease in the scale growth rate. It was speculated that grain boundary segregation of Mn in the scale in the low-pO_2 might hinder the inward movement of oxygen [5.19].

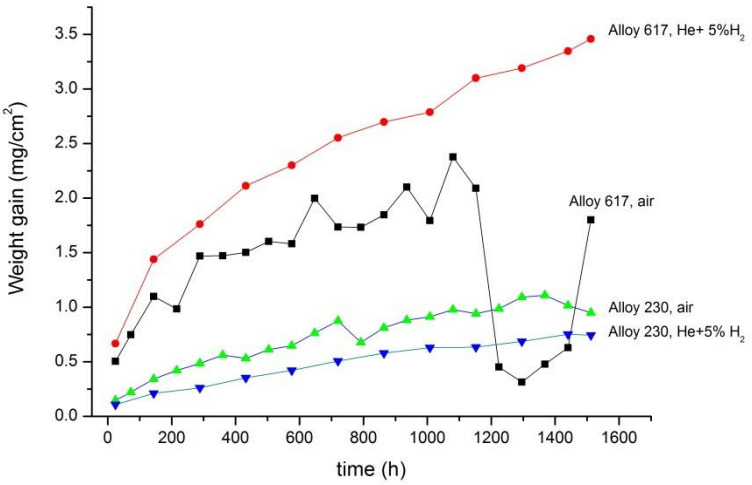

Fig. 5.13: Weight gain as a function time of alloy 617 and alloy 230 exposed to air and He + 5% H_2 at 950^{o}C

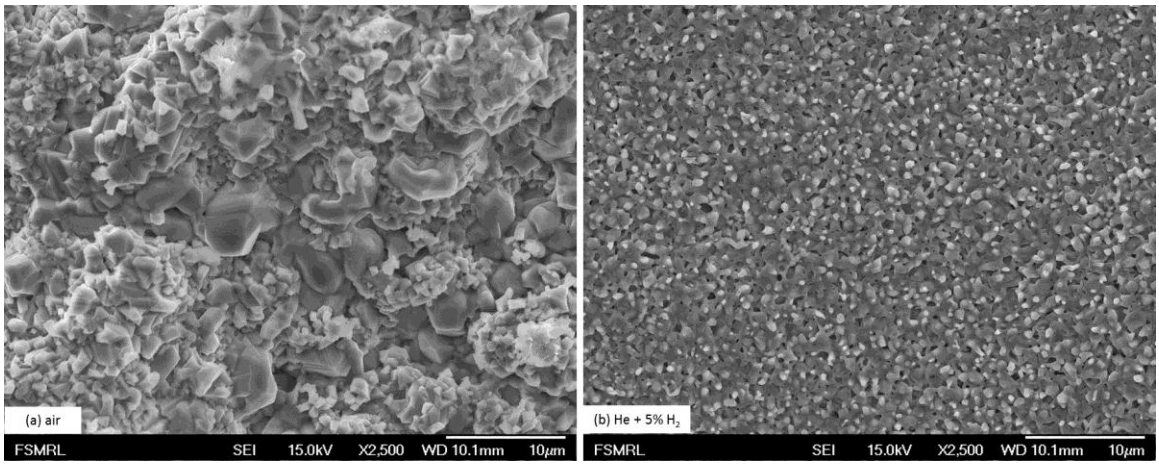

Fig. 5.14: Surface morphology of alloy 617 after 1512 h exposure in (a) air (b) He + 5%H_2. Note that smaller surface grains grown in He + 5% H_2 atmosphere at 950^{o}C.

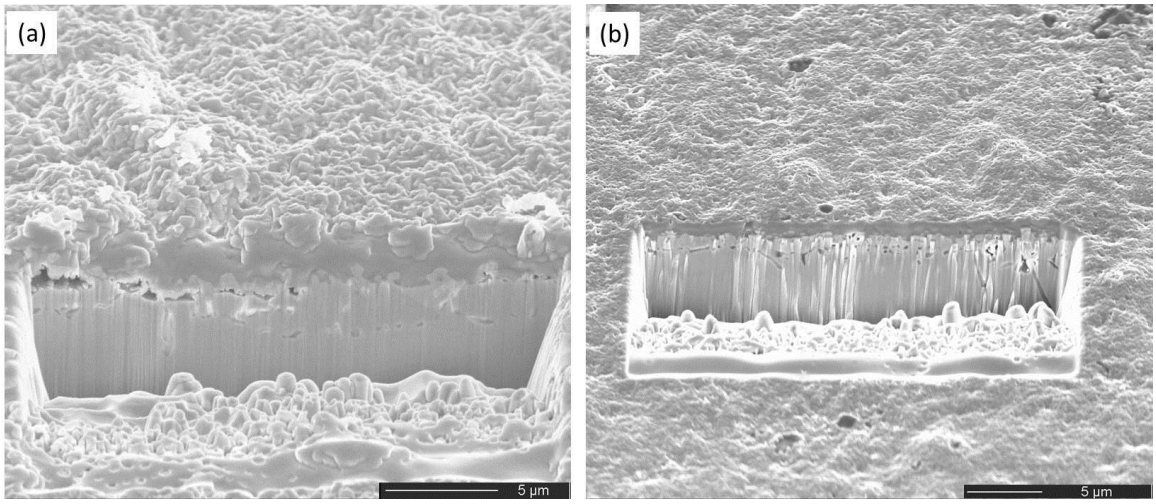

Fig. 5.15: Cross-sectional view of oxide scale grown on alloy 617 after 6 h exposure in (a) air (b) He+5% H_2 at 1000^{o}C.

Table 5.2: Reaction rate constant for alloy 617 and alloy 230 in air and He + 5% H_2

Materials	Parabolic rate constant ($g^2/cm^4/sec$)	Air	He + 5% H_2
Alloy 617	K_{617}	$8.18x10^{-13}$	$1.69x10^{-12}$
Alloy 230	K_{230}	$2.15x10^{-14}$	$1.12x10^{-14}$

5.6 Carburization behavior of alloy 617 and alloy 230

After exposure to a carbonaceous environment at selected temperatures, carbides are formed on both alloys. For alloy 617, XRD (Fig. 4.27) shows that Cr_3C_2 are formed on the surface. The depth of the carburization zone increases with increasing exposure temperature which is evident from SEM pictures (Fig. 4.28). For alloy 230, the carbides, Cr_3C_2, are grown on the surface, as indicated in Fig. 4.29. SEM pictures showed that the carburization zone is very significant. It is noted that the weight gain for alloy 230 did not follow parabolic law, suggesting that the rate controlling step is not controlled by diffusion of carbon based on a concentration gradient in alloy 230 over the range of conditions studied.

On the basis of thermodynamics, it is found experimentally [5.24] that chromium in alloy 230 has higher activity to react with carbon than in alloy 617. For engineering application, the concern is about the kinetics of carburization related to either weight gain or the extent of the carburization zone. The comparison of depth of carburization for both alloys is shown in Fig. 5.16. It demonstrates that alloy 617 has better carburization resistance than alloy 230. At 850^{o}C, the difference between the carburization depth is significant between the two alloys. With increasing exposure temperature, the difference between the depth for the two alloys decreases. The result of carburization resistance is also consistent with the weight change shown in Fig. 4.26 and Fig. 4.29 where alloy 230 exhibits greater increase in weight gain. It is noted that Cr_2O_3 for alloy 617 and Cr_2O_3/$MnCr_2O_4$ for alloy 230 are not observed in the present study, probably because the large amount of carbon was released to react with chromium in the very low oxygen partial pressure atmosphere. It was observed that the carburization rate is related to the oxygen partial pressure [5.25]. With increasing oxygen partial pressure, the oxide is relatively easy to form and carburization rate is decreased [5.25].

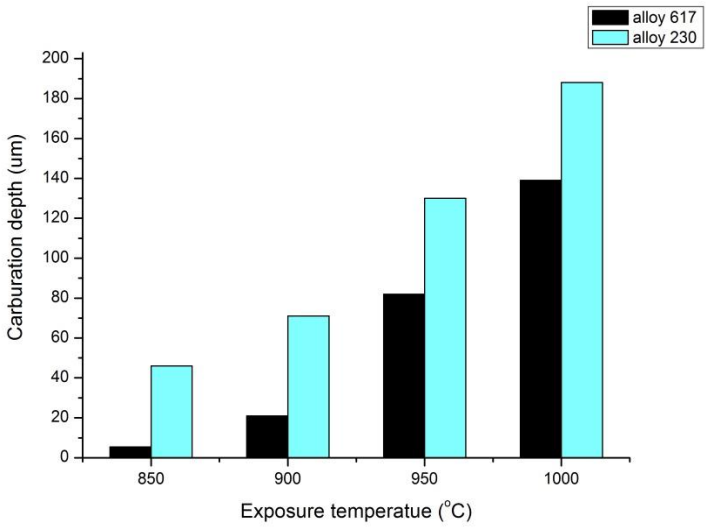

Fig. 5.16: Comparison of carburization depth of alloy 617 and alloy 230 under carbonaceous environment from 850 to 1000 ^{o}C

5.7 Biaxial thermal creep behavior of alloy 617 and alloy 230

Creep is time dependent plastic deformation for materials under constant load or stress applied at higher homologous temperatures. In the HTGR, the expected operating temperature is likely to reach about 950^{o}C where creep deformation is a major consideration for the design constraints. Since the melting temperatures are almost the same (1350^{o}C for alloy 617 and 1343^{o}C for alloy 230), the homologous temperatures for the two alloys are the same, which are 0.69 and 0.75 at 850 and 950^{o}C, respectively.

Creep deformation of alloy 617, shown in Fig. 4.32 and 4.33, suggests that tertiary creep regime quickly develops and takes a greater portion of the materials' life. It has been observed [5.26] that at 850^{o}C, creep deformation follows the classical form and at 950^{o}C, the secondary creep stage was missing. To further inspect biaxial creep deformation, strain rate vs. average creep time using equation (4.5) and (4.6) is plotted, as shown in Fig. 4.34 and 4.35. It shows that alloy 617 at the two temperatures under a biaxial stress state consisted of three distinct regimes: primary, secondary and tertiary. Compared with typical creep curves generally obtained (e.g. creep deformation of austenitic steel at about 550^{o}C), the period of secondary creep regime of alloy 617 is very short, even down to a minimum point at higher stress (e.g. 55 MPa at 850 ^{o}C and 32 MPa at 950^{o}C), followed by an increased creep rate until the specimen rupture. Similar results for alloy 617 under applied uniaxial stress have been also found [2.10,5.25-5.28]. The stress exponent analysis using equation (2.2) for alloy 617 is shown in Fig. 5.16 where n = 4.1 for 850^{o}C and n =3.3 for 950^{o}C are obtained. At 850^{o}C, n = 4.1 suggests climb-controlled dislocation creep [5.29] whereas at 950^{o}C, n= 3.3 implies a viscous glide mechanism as the rate-controlling step [5.30]. However, it is impossible to attribute a specific creep mechanism based only on the creep index.

Fig. 4.36 and 4.37 shows many intergranular creep voids or cavities, suggesting that nucleation, growth and coalescence of intergranular creep voids or cavities is the responsible micro-mechanism for creep fracture. The locations of void formation observed include: (1) grain boundaries (GBs) and (2) triple junction of GBs. In addition, these figures suggest that the grain boundaries where void formation is located are perpendicular to the hoop stress along the cross section area examined.

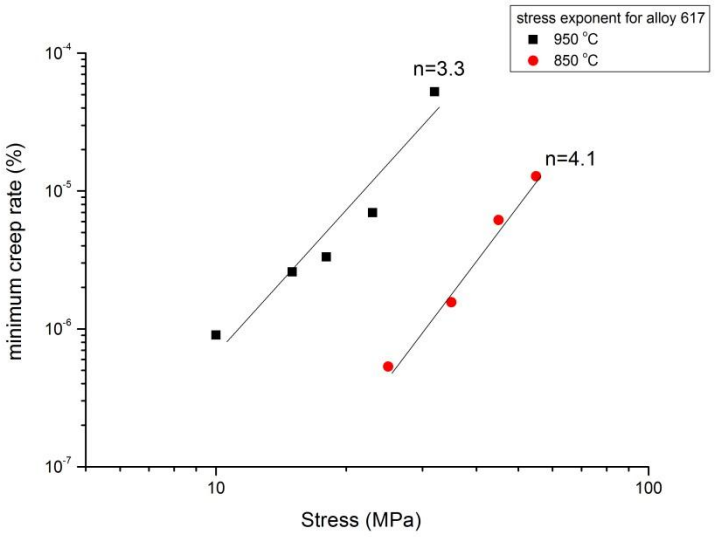

Fig. 5.17: stress exponent analysis of alloy 617 at 850 and 950^{o}C

As for alloy 230, Fig. 4.38 and 4.39 shows the diameter strain as a function of creep exposure time. It can be seen that secondary creep regime is more distinct at lower applied stresses. With increasing applied stress, the secondary creep regime decreases. Similar to alloy 617, creep deformation of alloy 230 exhibits three distinct creep regime: primary, secondary and tertiary (Fig. 4.40 and 4.41). Also, the tertiary part occupies a greater portion of the materials' creep lives. Very few studies were available for the creep response of alloy 230 in the uniaxial stress state. It was experimentally observed [5.31] that alloy 230 follows classical creep form, with short period of time in secondary creep regime, which is similar to creep behavior of alloy 617 discussed above.

Since these two alloys exhibit short secondary creep regime, it is necessary to inspect the microstructure that was developed at the beginning of tertiary creep. An interrupted test was conducted for alloy 230 with creep strain of 0.48% at 950^{o}C under the applied stress of 12 MPa. Fig. 5.17 (a) and (b) shows the cross-sectional view of alloy 230 at different locations. It clearly shows that voids developed at the grain boundaries perpendicular to the direction of hoop stress (Fig. 5.17 (a)) and at triple junction of GBs (Fig. 5.17 (b)). Therefore, the nucleation and growth of creep voids continuously develops at high temperatures at the onset of the tertiary creep regime. The development of creep voids reduces effective area subjected to the applied hoop stress, which increases the true stress and thus causes accelerated deformation within the

materials. This shortens the period of secondary creep and thus leads to an increasing in creep rate characteristic of tertiary creep. In principle, since the creep void development is stress-dependent, higher stress applied to the alloys may cause higher rate of nucleation and growth of the voids. As a result, one may expect that the secondary creep regime may become more prominent with decreasing the applied stress. This is consistent with the experimental findings in the present study. Fig. 5.17(a) and (b) also implies that surface oxidation might not be associated with internal development of creep voids.

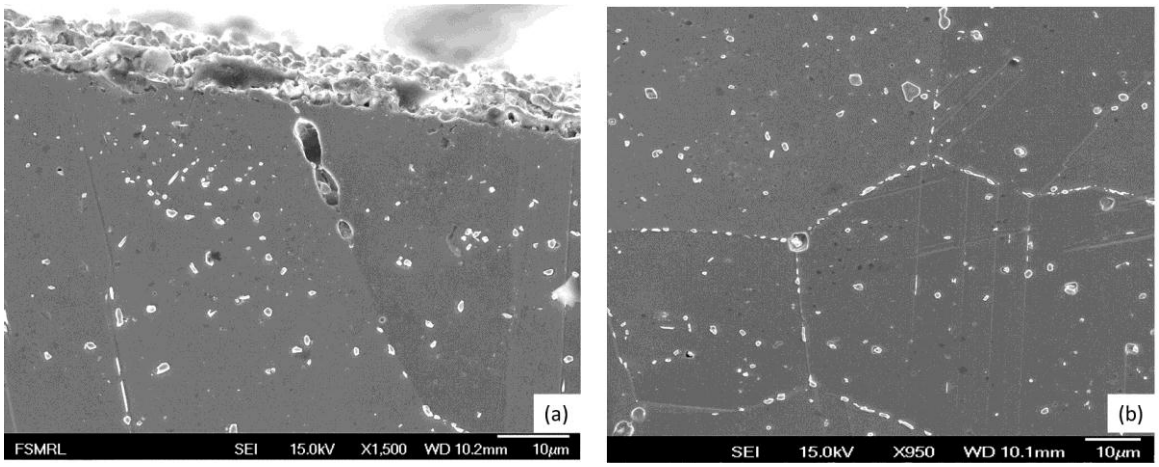

Fig. 5.18: Microstructure of alloy 230 crept at 950^{o}C for 100 h with void formation at (a) grain boundary (b)triple junction of GBs

Stress exponent analysis of alloy 230 (Fig. 5.18) indicates n = 11.1 at 850^{o}C and n= 2 at 950^{o}C. It was suggested [5.32] that higher stress exponent in high stress regime is attributed to the disruption of dislocation motion by carbides present within the materials. Therefore, high stress exponent is likely related to the interaction of dislocation with precipitates (e.g. W-rich carbide) in the present case. It is noted that at 950^{o}C, the stress exponent is decreased to 2, suggesting that a significant change in deformation mechanism and diffusional creep (lattice diffusion or boundary diffusion) is not the main controlling process. Some other mechanisms should be considered. According to existing models, n = 2 is presumed to be associated with a creep process where grain boundary sliding (GBS) is a likely dominated mechanism responsible for deformation. This mechanism is important in large strain deformation by GBS with diffusional accommodation, as is important in superplasticity. However, Fig. 5.17 (a) and (b) suggests that the voids formed along the grain boundaries, and there is little evidence of

displaced structures across grain boundaries. Therefore, GBS does not seem to be dominant in the conditions studied here. Since dislocations can exist in specimens with large grain size, dislocation creep is possible. The stress exponent deduced from the dislocation creep mechanism lies in a range of 3-12, which is larger than the observed value. Hence, the creep rate of alloy 230 is possibly controlled by a combination of creep mechanisms involving dislocation creep as a major component. Furthermore, Fig. 5.20(a) shows that there is a significant amount of large chromium-rich carbides, forming along the grain boundaries for alloy 230 after fracture following exposure to 950^{o}C under a stress of 12MPa. In contrast, the formation of large chromium-rich carbides along the grain boundaries was not observed after fracture for alloy 230 exposed to 850^{o}C under the stress of 35MPa, as shown in Fig. 5.19(b). Also noted that at 850^{o}C, fine precipitates within the grains are still uniformly distributed (Fig. 5.19 (a)), while zones relatively free of carbides are observed within the grains close to the inner wall (Fig. 5.19(b)). A study by Kihara et al. [2.12] suggests that intragranular carbides are effective in lowering creep rate, and the unstable intragranular carbides redissolve in favor of the more stable grain boundary carbides. The results of microstructures (Fig. 5.20) indicate that the stress exponent was influenced by internal microstructural change, which could be attributed to the increasing creep exposure temperature as well as the presence of the applied stress in the present case.

Fig. 5.21 shows creep life vs. applied stress for both alloys, indicating that alloy 617 and alloy 230 possess similar creep lives at 950^{o}C whereas alloy 230 has better creep properties than alloy 617 at 850^{o}C.

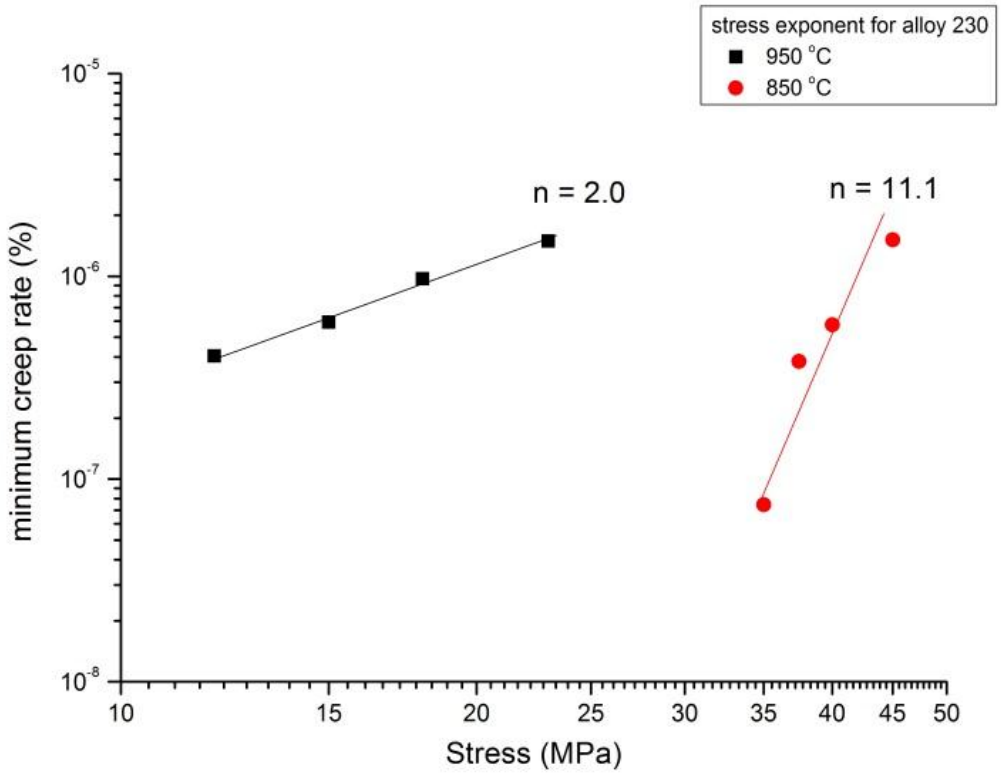

Fig. 5.19: stress exponent analysis of alloy 230 at 850 and 950°C

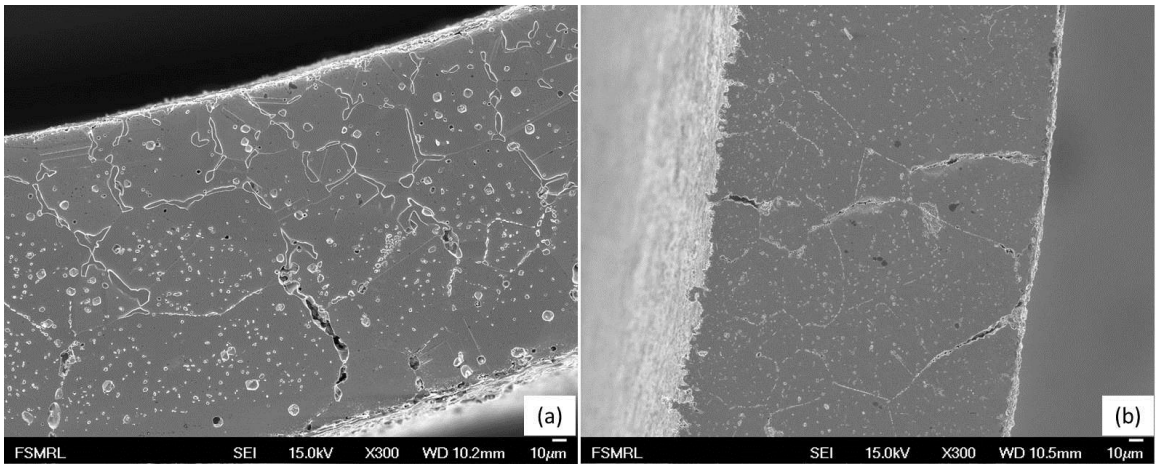

Fig. 5.20: Microstructure of alloy 230 after fracture at (a) 12 MPa, 950°C (b) 35 MPa, 850°C. Noted that formation of chromium-rich carbide along grain boundaries at 950°C.

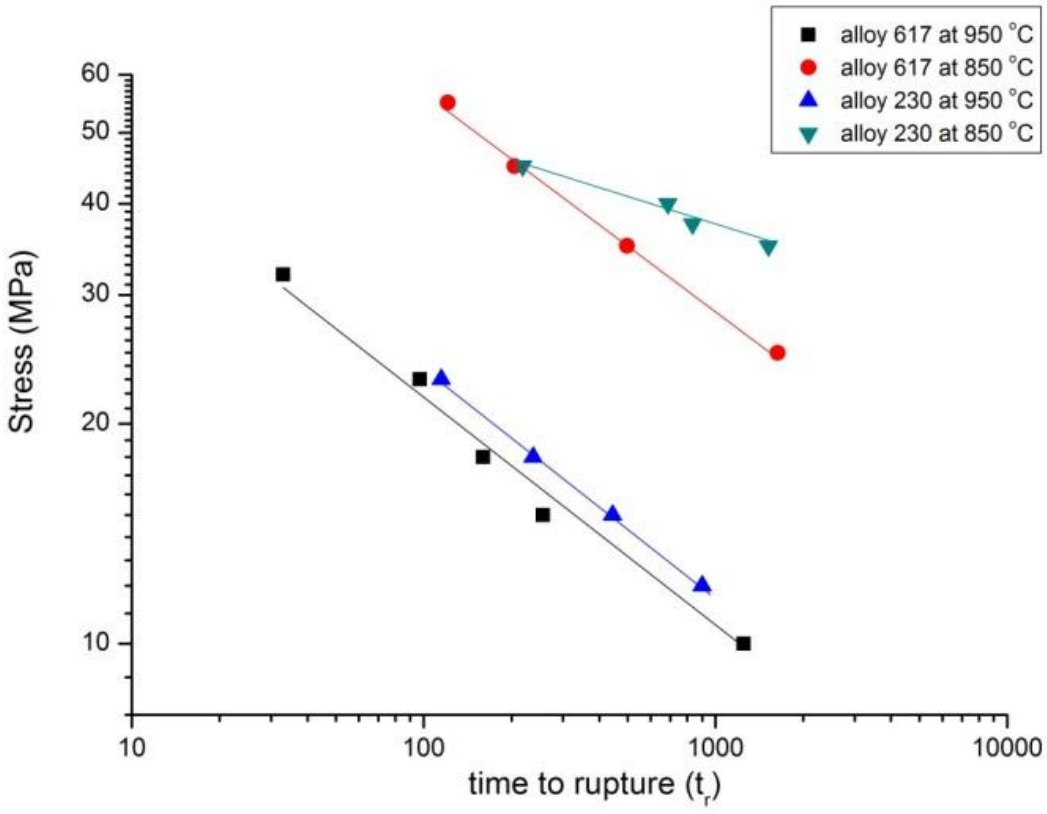

Fig. 5.21: Creep rupture life of alloy 617 and alloy 230 at 850 and 950^{o}C

5.8 Comparisons of creep behavior between biaxial stress and uniaxial stress state at high temperatures

The equivalent stress for biaxial stress state in the study is described by von Mises criterion, which was analyzed to be an appropriate parameter to assess the biaxial creep damage for 304 stainless steel [5.33]. Fig. 5.22 and 5.23 show the creep life vs. applied stress for uniaxial and biaxial stress state for alloy 617. Two main differences can be observed. First, the equivalent stress based on von Mises stress (or shear stress) is much lower than the applied uniaxial stress. Contributions from other stress components that exist in the alloy 617 have to be considered. In 1972, Hayhurst proposed [5.34] that creep life due to multi-axial states of stress can be expressed by the following equation:

$$t_r = C\left[\alpha\sigma_{MP} + \beta J_1 + \gamma J_2^{'1/2}\right]^{-\chi} \quad (5.9)$$

where t_r is time to rupture, σ_{MP} is maximum principle stress, C and χ are constants independent of stress for a given materials, α, β and γ are constants to be determined experimentally, and J_1 and $J_2^{'}$ in terms of principle stresses are given by $J_1 = \sigma_1 + \sigma_2 + \sigma_3$ and $J_2 = \frac{1}{6}\left[(\sigma_1 - \sigma_2)^2 + (\sigma_2 - \sigma_3)^2 + (\sigma_3 - \sigma_1)^2\right]$. To determine the three constants (α, β and γ), three independent tests with different stress states have to be conducted. However, there are no data available for alloy 617 to directly determine these parameters. Therefore, in the present case, assuming that only shear stress and hydrostatic stress are important, one can obtain the following equation:

$$t_r = \left[\sigma_s + \lambda\sigma_h\right]^{-\chi} \quad (5.10)$$

where σ_s is shear stress determined by equation (3.2) and σ_h is hydrostatic stress described by $\sigma_h = \sigma_1 + \sigma_2$ under biaxial stress state. For alloy 617, by assuming $\lambda = 0.5$, one can obtain creep life vs. equivalent stress, as shown in Fig. 5.22 and 5.23 at 850^{o}C and 950^{o}C, respectively. It can be seen that equation (5.9) or (5.10) cannot accurately predict each equivalent stress back to the uniaxial stress. This is due to the difference in the slope between the two stress state, which is represented by the constant χ. Equation (5.10) assumes that χ is a constant independent of stress, which was found to be accurate in some materials. However, for alloy 617 crept at high temperatures, this constant appears to be stress-state dependent. It is noted that creep damage arising from a biaxial stress state appears to be more severe than that from a uniaxial stress state, based on the steeper slope.

For alloy 230,a similar analysis was performed and shown in Fig. 5.24 and 5.25. It clearly displays that on the one hand, at 950^{o}C, the slope in biaxial stress state is steeper than in uniaxial stress state, similar to the case of alloy 617 at the same temperature. On the other hand, at 850^{o}C, it appears that the slope in biaxial state is similar to that in uniaxial state. This suggests that equation (5.9) or (5.10) can be appropriately used at 850^{o}C without significant change in χ. Also, it can be inferred that χ is temperature dependent in the present case.

To further discern the effect of biaxial stress state on creep life, creep damage may need to be considered in terms of a microstructure point of view. In this study, hoop stress produced by internal pressure is larger than longitudinal stress by a factor of 2. In addition, the cross-sectional view of the fracture surface also indicates that the crack growth is perpendicular to hoop stress by which the creep failure is generated. Therefore, the presence of longitudinal stress affecting creep life is of importance. Two types of damage that were caused by longitudinal stress during creep deformation need to be considered: one is macroscopic plastic deformation; the other is stress-generated void nucleation and growth. The first term can be estimated by the equation of power-law creep. For instance, at 950^{o}C, the creep rate of alloy 617 would be decreased to $(1/3)^{3.3}$ = 2.66% of its original value if the hoop stress were not present; 3.3 comes from the stress exponent at 950^{o}C. It clearly shows that the substantial creep strain was generated from the applied hoop stress. Also, it has been found experimentally that the corresponding axial strain is much lower than diameter stain [5.33,5.35,5.36]. Therefore, longitudinal stresses can significantly enhance nucleation and growth of creep void in these alloys.

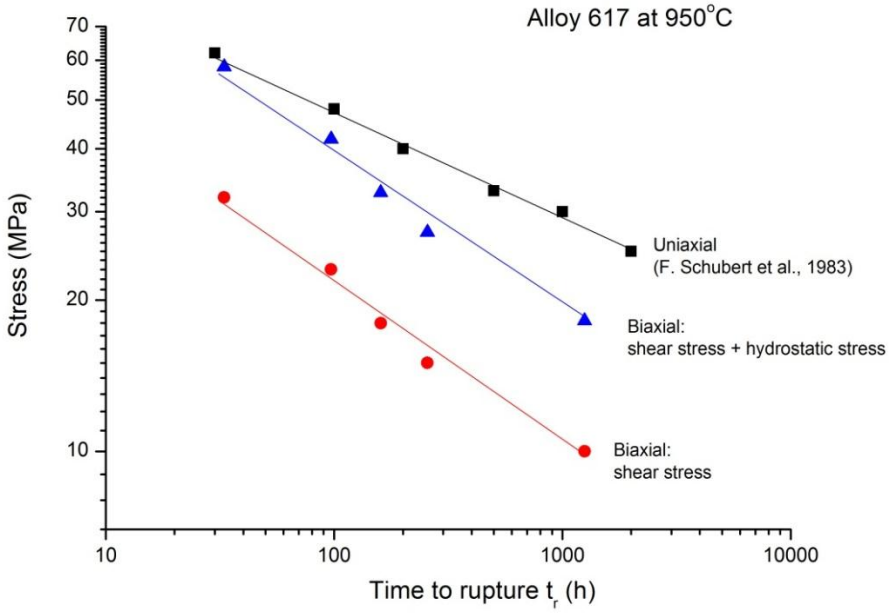

Fig. 5.22: Comparisons between uniaxial and biaxial stress state for alloy 617 at 950^{o}C

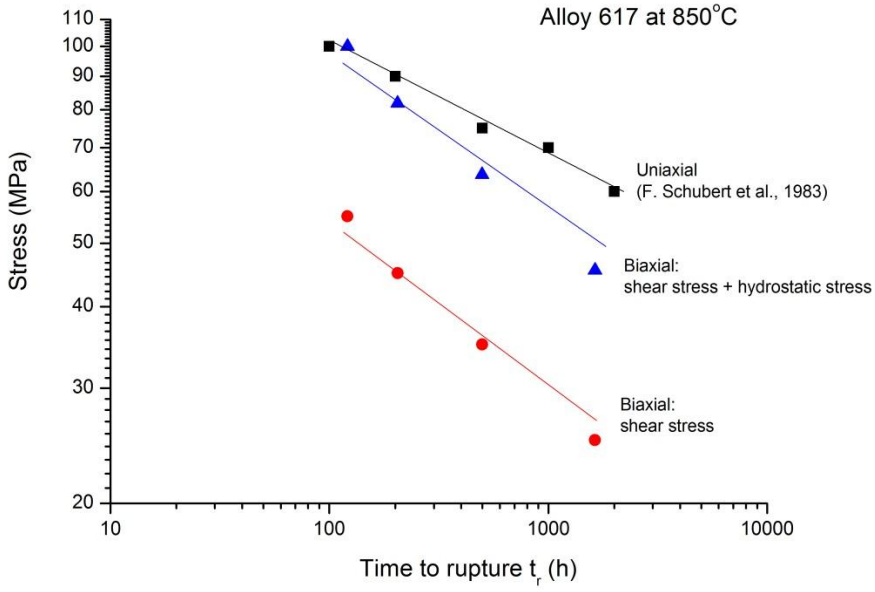

Fig. 5.23: Comparisons between uniaxial and biaxial stress state for alloy 617 at 850°C

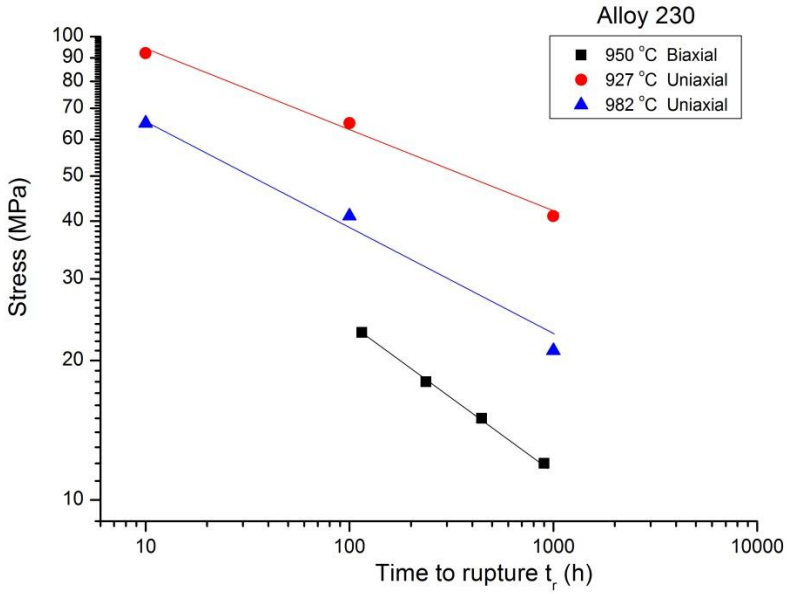

Fig. 5.24: Comparisons between uniaxial and biaxial stress state for alloy 230 at 950°C

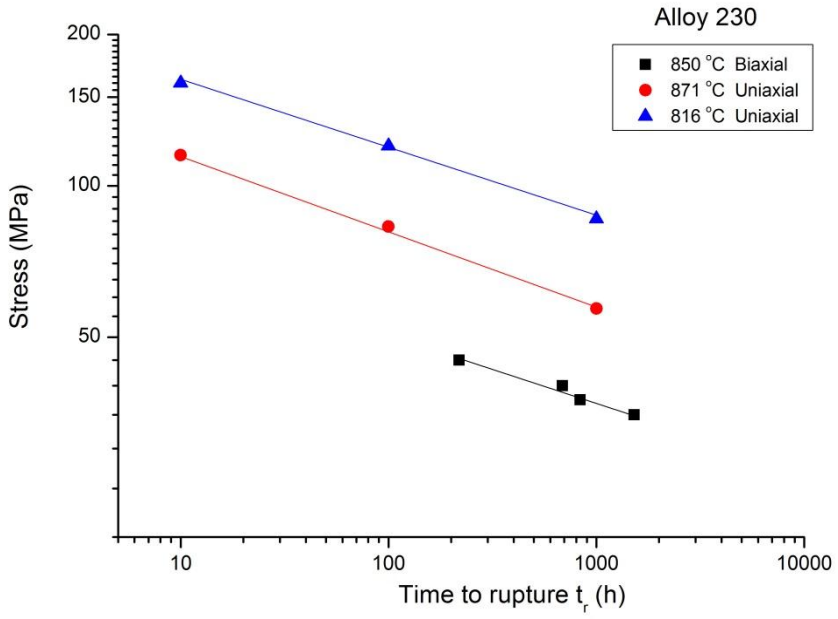

Fig. 5.25: Comparisons between uniaxial and biaxial stress state for alloy 230 at 850^{o}C

5.9 Evaluation of the empirical relation of predicting long-term creep life from short term testing

A large number of creep tests indicates that a correlation of steady-state (or minimum) creep rate and creep rupture time can be described as follows

$$t_r \dot{\varepsilon}_{\min}^{\alpha} = C_0 \qquad (5.11)$$

where α and C_0 are materials constants, independent of stress and temperature. These constants need to be determined experimentally. The relation is termed Monkman-Grant relation [5.37]. It was verified for many materials including pure metals, solid solution alloys and more complicated alloys (e.g. austenite stainless steel and Ni-base superalloys). This relation reveals a strong dependence between creep life and minimum creep rate. In the present case, Fig. 5.26 and Fig. 5.27 show creep life as a function of minimum creep rate for alloy 617 and alloy 230, respectively. For alloy 617, the Monkman-Grant relation seems to provide promise for

estimating long-term creep rupture life. However, alloy 230 did not follow the relation suitably due to a wide scatter band of data points. This also suggests that that the material constants α and C_0 are temperature dependent. Tables 5.3 and 5.4 list the values of α and C_0. The difference between alloy 617 and alloy 230 might be attributed to differences in deformation mechanisms. Deformation mechanism for alloy 617 at the two temperatures is likely associated with dislocation movement. For alloy 230, dislocation creep is dominated mechanism at 850^{o}C, whereas other deformation mechanisms combined with dislocation creep may operate at 950^{o}C.

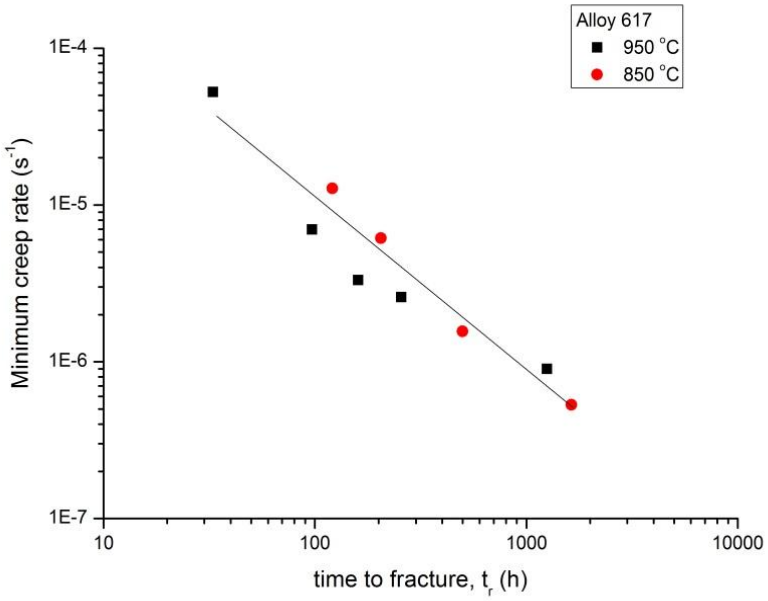

Fig. 5.26: Relation between minimum creep rate and rupture time for alloy 617.

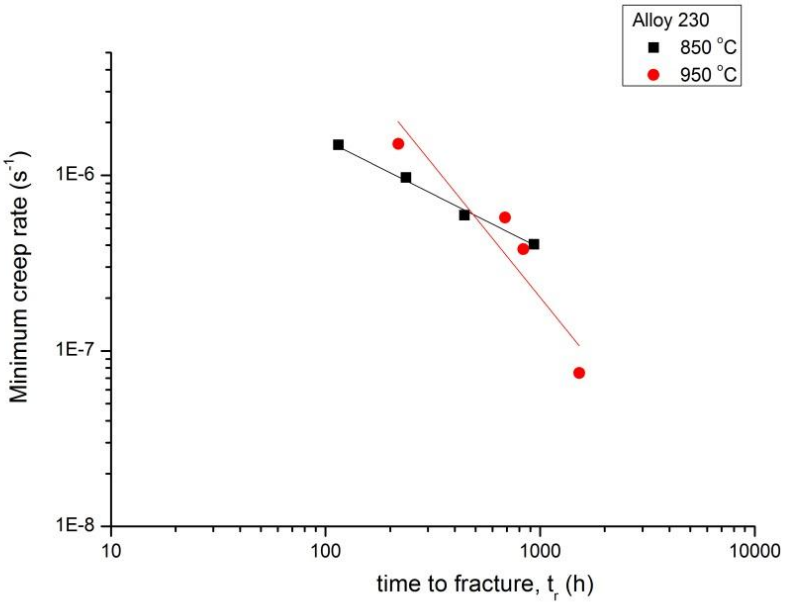

Fig. 5.27: Relation between minimum creep rate and rupture time for alloy 230.

Table 5.3: Creep Parameters in the Monkman–Grant Equation of alloy 617

α	C_0
0.91957	0.00258.

Table 5.4: Creep Parameters in the Monkman–Grant Equation of alloy 230

Temperature	α	C_0
950	1.5731	$7.85*10^{-8}$
850	0.6887	0.2575

CHAPTER 6

CONCLUSIONS

Surface degradation of alloy 617 and 230 was investigated by exposures to air, reducing (H_2+5%H_2) and reducing plus carburizing environments (H_2+5%H_2+1%CH_4) at elevated temperatures. The study included short-term and long-term exposure. In addition, biaxial thermal creep deformation and rupture studies using pressurized creep tube technology were carried out at 850 and 950^{o}C. Creep deformation and damage mechanisms were analyzed based on those test results. The following conclusions could be drawn fron this study:

1. Incipient oxidation of alloy 617 showed a two-stage oxidation kinetics, with each stage obeying a parabolic oxide scale growth law. The activation energy for the first stage and the second stage are 271.2 and 318 kJ/mol, respectively, indicating that the first stage is controlled by Cr diffusion through chromia, and the second stage by Cr diffusion through an interfacial layer between the alloy and the oxide film.
2. Incipient oxidation kinetics of Haynes 230 alloy exhibited a two-stage oxidation process; the two stages obey parabolic oxidation rate law. The activation energies for stage I and stage II are 246.5 and 212.1 kJ/mol, respectively. The oxidation rate is lower in stage II than stage I. The results of structural characterization revealed that Cr_2O_3 and $MnCr_2O_4$ are mixed with each other and uniformly distributed throughout the oxide scale. SEM results show that the oxide scale grown on the substrate is dense and maintains good adhesion at the scale/substrate interface over the entire temperature range.
3. Incipient corrosion tests in low-pO_2 gas indicated that a protective layer of Cr_2O_3 was grown on alloy 617 although weight decrease was observed at the very beginning stages of exposure. For alloy 230, the weight loss increased with increasing exposure temperature, which is attributed to the loss of nickel and carbon.
4. Results of long-term exposure in air showed that around 360 h of exposure, the oxide scale grown on alloy 617 consisted of Cr_2O_3 and $NiCr_2O_4$. Significant spallation of oxide scale

result in the decrease in weight after 1224 h exposure for alloy 617, while alloy 230 exhibited stable increase in weight with increasing exposure time. Both short-term and Long-term exposure indicated that alloy 230 possesses better oxidation resistance than alloy 617.

5. Reducing environment may cause a faster scale growth rate in alloy 617 whereas slower scale growth rate was observed in alloy 230. Microstructural characterization showed that much finer grains were formed in low-pO_2 gas, compared with air environment for both alloys.
6. Carburization tests showed that alloy 617 had superior carburization resistance compared to alloy 230. X-ray diffraction analysis showed that chromium-rich carbide near the surface area is in a form of Cr_3C_2.
7. Residual stress measurements showed that the intrinsic residual stress of Cr_2O_3 are tensile during the growth of the oxide for both alloys. The development of intrinsic stresses with increasing exposure time in low-pO2 gas is relatively stable than in air, which may be attributed to smaller grain size formed in the reducing environment.
8. Creep behavior of the two alloys showed that three distinct regimes: primary, secondary and tertiary regime. Tertiary creep takes a greater part of the materials' creep lives with increasing applied stresses, and the fraction of time for the secondary creep regime decreases.
9. At 950^{o}C, alloy 617 and alloy 230 had similar creep rupture life, whereas alloy 230 exhibited a better creep rupture life than alloy 617 at 850^{o}C. Nucleation, growth and coalescence of creep voids are the dominant micro-mechanisms for creep fracture. During deformation at the onset of the tertiary creep regime, void formation was observed along grain boundaries and at triple junction of grain boundaries.
10. Creep life arising from biaxial stress state was not able to be appropriately evaluated using the existing model. It was found that creep damage from biaxial stress state at high temperatures was more severe than that from uniaxial stress in most cases.
11. The Monkman-Grant relation seems to provide a promising method in estimating long-term creep rupture life for alloy 617, while alloy 230 did not follow the relation, which might be related to the significant change in microstructure at high temperatures.

CHAPTER 7

FUTURE WORK

7.1 Corrosion issues

The current research focused on the oxidation, low pO_2 pressure and carburization phenomena for both alloys and the resulting microstructures, which provides a fundamental understanding of gas corrosion. According to the gas chemistry shown in Table 2.2 and the stability diagram suggested in Fig. 2.5, it is necessary to know the corrosion phenomena under these environments. As mention before, it is expected that the alloys are slightly oxidized with internal stable carbides, and therefore, the goal is to understand how different gas species reaction with metallic surface. Due to the complexity of gas compositions at high temperatures, a good starting point is the use of gas-chromatography (GC), to independently study the effect of each gas on the metallic surface. Then, by controlling partial pressure of oxygen (or water vapor), it is possible to determine reasonable the amount of oxygen (or water vapor) in ppm or partial pressure which could form a protective oxide on the metallic surface. The GC was installed in our laboratory, providing the simulated HTGR environments for the research purpose.

7.2 Creep issues

In this study, creep damage was found to be more severe in biaxial stress conditions compared to uniaxial loading. This is due to the presence of the other tensile stress in the materials. Since the damage is attributed to creep void development, it is important to consider how the rate of nucleation and growth of creep voids is enhanced due to biaxial tensile stress. Development of a model which takes into account multiaxial stress states in creep is necessary.

Another way to deal with the failure of the accelerated creep damage related to creep cavities is to consider the propagation of macroscopic cracks. This process takes up the largest

fraction of the creep rupture life. The initial macroscopic cracks inside the materials may come from some metallurgical defects, manufacturing processes and most likely from the evolution of grain boundary carbides. Therefore, fracture mechanics should be used as a fundamental tool to study the microscopic crack formation processes and the macroscopic crack growth mechanisms. In the present study, a good starting point is to consider the stress intensity factor based on biaxial stress state. Fig. 7.1 shows a schematic diagram of a crack under biaxial stress state. It is necessary to evaluate the intensity of stress concentration at the crack tip and the corresponding crack propagation.

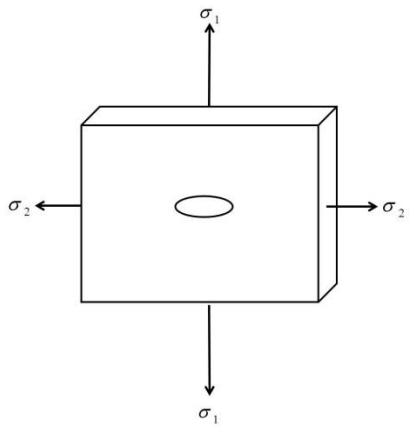

Fig. 7.1: Crack in a large plate under a biaxial stress state

7.3 Creep-Corrosion issues

For the designer's point of view, it is necessaryto investigate the creep deformation under various simulated HTGR environments. The results directly provides useful data base for the construction of HTGR. Furthermore, by examining the microstructure, we can understand the effects of corrosive environments, especially for carburization and decarburization atmospheres, on the creep deformation.

REFERENCES

[1.1] "A Technology Roadmap for Generation IV Nuclear Energy Systems," U.S. DOE Nuclear Energy Research Advisory Committee and the Generation IV International Forum 2002.

[1.2] W. Ren and R. Swindeman, "A Review on Current Status of Alloys 617 and 230 for Gen IV Nuclear Reactor Internals and Heat Exchangers", Journal of Pressure Vessel Technology, vol. 131, 2009.

[1.3] D. Butler, 2004, "Energy: Nuclear power's new dawn," Nature, Vol. 429, pp. 238-240.

[1.4] K.G.E. Brenner, and L.W. Graham, Nucl. Technol. 66(2), (1984), p. 404

[1.5] H.G.A. Bates, Nucl. Technol., 66(2), (1984), p. 415

[1.6] C. Cabet and F. Rouillard, ASME J. Eng. Gas Turbines Power, 131 (2009), pp. 062902.

[1.7] K. Hada, I. Nishiguchi, Y. Muto and H. Tsuji, Nucl. Eng. Des. 132 (1991), pp. 1–11

[1.8] P.J. Ennis and D.F. Lupton, Proceedings of the Petten International Conference on Behaviour of High Temperature Alloys in Aggressive Environments, The Metals Society, ed., (1980) pp. 979–991.

[1.9] P.S. Shankar and K. Natesan, J. Nucl. Mater. 366 (2007), 28–36

[1.10] http://www.heatric.com.

[1.11] Saito, S., et al., 1991. Present status of the high temperature engineering test reactor (HTTR). Nucl. Eng. Des. 132, 85–93.

[1.12] R. E. Mizia, "Next Generation Nuclear Plant Intermediate Heat Exchanger Acquisition Strategy," Idaho National Laboratory2008

[1.13] K. Natesan, A. Purohit, et al., 2003, Materials Behavior in HTGR Environments, ANL 02/37, February, 2003.

[1.14] Takahashi, T., Fujiwara, J., Matsushima, T., Kiyokawa, M., Morimoto, I., Watanabe, T., 1978. Analysis of precipitated phase in heat treated INCONEL alloy 617. Transactions ISIJ 18, 221–224.

[1.15] Gariboldi, E., Cabibbo, M., Spigarelli, S., Ripamonti, D., 2008. Investigation on precipitation phenomena of Ni–22Cr–12Co–9Mo alloy aged and crept at high temperature. International Journal of Pressure Vessels and Piping 85, 63–71.

[1.16] H. M. Tawancy, D. L. Klarstrom, and M. F. Rothman, 1984, "Development of a New Nickel-Base Superalloy," Jom-J Min Met Mat S, Vol. 36, pp. 58-62.

[1.17] H.M. Tawancy, J. Met., 27 (1992), pp. 6481–6489

[1.18] H.M. Tawancy, Oxid. Met., 45 (1996), pp. 323–348

[2.1] Garofalo, F., "Fundamentals of creep and creep-rupture in metals", The MacMillan Company, New-York, 1965.

[2.2] S.O. Ojediran, O. Ajaja, J. Mater. Sci., 23 (1988), p. 4037

[2.3] J.E. Bird, A.K. Mukherjee, J.E. Dorn, D.G. Brandon, A. Rosen (Eds.), Quantitative Relation Between Properties and Microstructure, Jerusalem University Press (1969), pp. 255–342

[2.4] Kassner, M.E., "Fundamentals of Creep in Metals and Alloys", 2009, Elsevier Science; 2nd edition, p.125.

[2.5] F.R.N. Nabarro, Acta Metall., 37 (1989), pp. 2217–2222

[2.6] T. Shrestha, M. Basirat, I. Charit, G. Potirniche, K. Rink, U. Sahatm, J. Nucl. Mater., 423 (2012), 110
[2.7] D.V.V. Satyanarayana, G. Malakondaiah, D.S. Sarma, Mater. Sci. Eng., A, 323 (2002), pp. 119–128
[2.8] Ashby, M.F., "The Microstructure and Design of Alloys", Proceedings, Third International Conference on Strength of Metals and Alloys, Vol. 2, Cambridge, England, 1973, p.8
[2.9] F. Schubert, U. Bruch, R. Cook, H. Diehl, P.J. Ennis, W. Jakobeit, H.J. Penkalla, E.T. Heesen and G. Ullrich. Nucl. Technol., 66 (1984), p. 227.
[2.10] A.K. Roy, M.H. Hasan, J. Pal, Mater. Sci. Eng., A,, 520 (2009), pp. 184–188
[2.11] S. Chomette, J.M. Gentzbittel and B. Viguier. J. Nucl. Mater., 399 (2010), pp. 266–274.
[2.12] S. Kihara, A. Ohtomo, Y. Saiga, and J.B. Newkirk: Metall. Mater. Trans. A, 1980, vol. 11A, pp. 1019–31
[2.13] S. Schlegel, S. Hopkins, E. Young, J. Cole, T. Lillo, and M. Frary: Metall. Mater. Trans. A, 2009, vol. 40A, DOI: 10.1007/s11661-009-0027-7.
[2.14] http://www.specialmetals.com
[2.15] F. Schubert, H.J. Seehafer and E. Bodmann, Status of design code work in Germany concerning materials and structural aspects for the heat exchanger components of advanced HTR's, Proc. ASME-Conf. Status of Materials Development and Technology for Advanced Nuclear Heat Exchangers Denver, USA (Oct. 1982).
[2.16] Kim, W.-G., Yin, S.-N.a , Lee, G.-G.a , Kim, Y.-W. , Kim, S.-J. Creep oxidation behaviour and creep strength prediction for Alloy 617, INT J PRES VES PIP, 87 (2010) 289-295
[2.17] S.K. Sharma, G.D. Ko, F.X. Li, K.J. Kang, J. Nucl. Mater., 378 (2008), pp. 144–152
[2.18] Bates, H. G. A., 1984, "The Corrosion Behavior of High-Temperature Alloys During Exposure for Times Up to 10000 h in Prototype Nuclear Process Helium at 700 to 900°C," Nucl. Technol., 66(2), pp. 415–428.
[2.19] Ennis, P. J., and Lupton, D. F., 1980, "The Relationship Between Carburisation and Ductility Loss," Proceedings of the Petten International Conference on Behaviour of High Temperature Alloys in Aggressive Environments, The Metals Society, ed., pp. 979–991.
[2.20] Kurata, Y., Ogawa, Y., Nakajima, H., and Kondo, T., 1989, "Creep Rupture Characteristics in the HTGR Simulated Helium Gas Environment and Their Relevance to Structural Design," Proceedings of the Workshop on Structural Design Criteria for HTR, pp. 275–291
[2.21] C. Cabet, J.Jang, J.Konys, and P.F. Tortorelli. MRS Bull. 34, (2009) 35-39.
[2.22] Wright, R., 2006, "Summary of Studies of Aging and Environmental Effects on Inconel 617 and Haynes 230," Report No. INL/EXT-06–11750.
[2.23] R. D. Burnette and N. L. Baldwin, 1980, "Primary Coolant Chemistry of the Peach Bottom and Fort St. Vrain High Temperature Gas-Cooled Reactors," Specialists Meeting on Coolant Chemistry, Plate-out and Decontamination in Gas Cooled Reactors, Juelich, Germany, December 1980, IAEA, Vienna, IWGGCR-2, pp. 132-137.
[2.24] R. A. Simon and P. D. Capp, 2002, "Operating Experience with the Dragon High Temperature Reactor Experiment," Proceedings on High Temperature Reactors, Petten, Netherlands, April 2002, IAEA, Vienna, HTR-2002. pp. 1-6.
[2.25] R. Nieder and W. Stroter, 1988, "Long-term Behavior of Impurities in an HTR Primary Circuit," VGB Kraftwerstechnik, Vol. 68, July 1988, pp. 671-676.

[2.26] R. Nieder, 1980, "Prediction on an HTR Coolant Composition After Operational Experience with Experimental Reactors," Specialists Meeting on Coolant Chemistry, Plate-out and Decontamination in Gas Cooled Reactors, Juelich, FRG, December 1980, IAEA, Vienna, IWGGCR-2, pp. 144-152.
[2.27] C. Wagner, Z. Phys. Chem., 21 (1933), 25.
[2.28] N. Birks, H. Rickert, J. Inst. Metals, 91 (1961-62), 308.
[2.29] E.A. Gulbransen, K.F. Andrew, J. Electrochem. Soc., 106 (1959), 941
[2.30] A. Duval, F. Miserque, M. Tabarant , J.-P. Nogier and A. Gédéon, Oxid. Met., 74 (2010) 215–238.
[2.31] H. J. Christ, L. Berchtold, and H. G. Sockel, Oxid. Met. 26 (1986) 45–76.
[2.32] D. Kim, C. Jang, W.S. Ryu, Oxid. Met. 71 (2009) 271–293.
[2.33] J. Li, J. Pu, B. Hua, and G. Xie, J. Power Sources, 159 (2006) 641–645.
[2.34] D.M. England and A.V. Virkar, J. Electrochem. Soc. 146 (9) (1999) 3196-3202
[2.35] Caplan, D. and G.I. Sproule, Effect of grain structure on the high-temperature oxidation of Cr. Oxidation of Metals, 1975. 9(5): p. 459-472.
[2.36] Skeldon, M., J.M. Calvert, and D.G. Lees, An investigation of the growth mechanism of Cr2O3 on pure chromium in 1 atm oxygen at 950oC. Oxidation of Metals, 1987. 28(1-2): p. 109-125.
[2.37] Graham, M.J., et al., Anion transport in growing Cr2O3 and Al2O3 scales. Materials science forum, 1989. 43: p. 207-242.
[2.38] Barnes, D.G., et al., Philosophical Magazine, 1973. 28: p. 1303.
[2.39] Lees, D.G. and J.M. Calvert, Corrosion Science, 1976. 16: p. 767
[2.40] Zurek, J., et al., Materials Science and Engineering A, 2008. 477: p. 259.
[2.41] B. Pieraggi, R.A. Rapp, Acta Metall., 36 (1988), p. 1281
[2.42] N. B. Pilling and R. E. Bedworth, J. Inst. Met., 29 (1923), 529.
[2.43] F.N. Rhines, J.S. Wolf, Met. Trans., 1 (1970), p. 1701
[2.44] A.M. Huntz, S. Daghigh, A. Piant, J.L. Lebrun, Mater. Sci. Eng. A, 248 (1998), p. 44.
[2.45] B.R. Barnard, T.R. Watkins, P.K. Liaw, Oxid. Met., 74 (2010), pp. 305–318
[2.46] Brenner, K.G.E. and L.W. Graham, The development and application of a unified corrosion model for high-temperature gas-cooled reactor systems. Nuclear Technology, 1984. 66: p. 40.
[2.47] Brenner, K.G.E. Ternary diagrams for characterization of metallic corrosion in high temperature reactors. In Proc. Conf. on Gas-Cooled Reactors Today. 1982. Bristol, UK.
[2.48] Brenner, K.G.E. Ternary diagram for characterization of metallic corrosion in high temperature reactors. In Gas Cooled Reactors Today. 1982. London: British Nuclear Energy Society.
[2.49] Quadakkers, W.J. and H. Schuster, Corrosion of high temperature alloys in the primary circuit of high temperature gas cooled reactors.-Part I: theoretical background. Werkstoffe and Korrosion, 1985. 36: p. 141-150.
[2.50] Quadakkers, W.J., Corrosion of high temperature alloys in the primary circuit helium of high temperature gas cooled reactors. Part II: Experimental results. Werkstoffe and Korrosion 1985. 36: p. 335.
[2.51] Christ, H.-J., et al., Mechanism of high-temperature corrosion in helium containing small amounts of impurities. I. theoretical and experimental characterization of the gas phase. Oxidation of Metals, 1988. 30(1-2): p. 1-26.
[2.52] C. Cabet and F. Rouillard, ASME J. Eng. Gas Turbines Power, 131 (2009), pp. 062902.

[3.1] http://www.ms.ornl.gov/fusionreactor/pdf/june1999/kurtz1.pdf
[3.2]http://www.betalasermike.com/index.php/en/beta-lasermike-products-en/diameter-a-ovalityen
[3.3] C.-H. Ma, J.-H. Huang, Haydn Chen, Thin Solid Films, 418 (2002), p. 73
[3.4] J.H. Huang, Y. Kae-Jy, P. Sit and G.-P Yu., Surface and Coatings Technology, 200 (2006), pp. 4291–4299
[5.1] H.J. Christ, L. Berchtold, H.G. Sockel, Oxid. Met. 26 (1986) 45–76.
[5.2] D. Kim, C. Jang, W.S. Ryu, Oxid. Met. 71 (2009) 271–293.
[5.3] W.C. Hagel, A.U. Seybolt, J. Electrochem. Soc. 108 (1961) 1146.
[5.4] R.E. Lobnig, H.P. Schmidt, K. Hennesen, H.J. Grabke, Oxid. Met. 37 (1992) 81–93.
[5.5] S.C. Tsai, A.M. Huntz, C. Dolin, Oxid. Met. 37 (1995) 581–596.
[5.6] D.J. Young, High Temperature Oxidation and Corrosion of Metals, Elsevier Ltd., 2008. p.33
[5.7] D. Burgreen, Elements of Thermal Stress Analysis, C.P. Press, New York, 1971. p. 462.
[5.8] C.S. Richard, J. Lu, G. Béranger, F. Decomps, J. Therm. Spray Technol. 4 (4) (1995) 342.
[5.9] M. Schütze, Protective Oxide Scales and Their Breakdown, Wiley, New York, 1997. p. 43.
[5.10] J.F. Shackelford, W. Alexander, CRC Materials Science and Engineering Handbook, 3rd ed., CRC Boca Raton FL, 2001. p. 465.
[5.11] http://www.specialmetals.com/products/inconelalloy617.php.
[5.12] R.W. Hoffman, Thin Solid Films 34 (1976) 185.
[5.13] W.D. Nix, B.M. Clemens, J. Mater. Res. 14 (1999) 3467–3473.
[5.14] P. Kofstad, K.P. Lillerud, Oxid. Met. 17 (1982) 177–194.
[5.15] A.C.S. Sabioni, B. Lesage, A.M. Huntz, J.C. Pivin, C. Monty, Phil. Mag. A 66 (3) (1992) 333.
[5.16] S.J. Rothman, L.J. Nowicki, G.E. Murch, J. Phys. F. 10 (1980) 383.
[5.17] P. Jian, L. Jian, H. Bing, G. Xie, J. Power Sources 158 (2006) 354–360.
[5.18] A. Ul-Hamid, Anti-Corrosion Methods and Materials, 51 (2004) pp. 216 – 222
[5.19] H.J. Christ, U. Kunecke, K. Meyer and H.G. Sockel, Oxid. Met., 30 (1988), pp. 27–51
[5.20] J. Zurek, D.J. Young, E. Essuman, M. Hansel, H.J. Penkalla, L. Niewolak, W.J. Quadakkers, Mater. Sci. Eng. A 477 (2008) 259–270.
[5.21] T. Norby, J. Phys. IV Coll. C9 3, (1993) 99.
[5.22] T. Norby, Adv. Ceram. 23, (1987) 107.
[5.23] A. Galerie, Y. Wouters, M. Caillet, Mater. Sci. Forum, 369–372 (2001), pp. 237–238.
[5.24] S. Gossé, T. Alpettaz, S. Chatain and C. Guéneau, Journal of Engineering for Gas Turbines and Power, 131 (2009) 062901.
[5.25] H. Li, W. Chen, Corr. Sci. 52 (2010) 2481
[5.26] Schubert, F., Bruch, U., Cook, R., Diehl, H., Ennis, P., Jakobeit, W., Penkalla, H. J., Te Hessen, E., and Uhlrich, G., 66 (1984), 227.
[5.29] W.G. Kim, S.N. Yin, G.G. Lee, Y.W. Kim, S.J. Kim, Int. J. Pressure Vessels Piping, 87 (June (6)) (2010), pp. 289–295
[5.28] F. Schubert, H.J. Seehafer, E. Bodmann, Proc. ASME-Conf. Status of Materials Development and Technology for Advanced Nuclear Heat Exchangers, Denver, USA (Oct. 1982)
[5.29] Kassner, M.E., "Fundamentals of Creep in Metals and Alloys", 2009, Elsevier Science; 2nd edition, p.61

[5.30] Kassner, M.E., “Fundamentals of Creep in Metals and Alloys”, 2009, Elsevier Science; 2nd edition, p.125
[5.31] M. Maurizio, A. Giuliano, L.Valentino, Materials Science Forum, 2285 (2010) 638.
[5.32] P.J. Ennis, A. Zielinska-Lipiec, O. Wachter, A. Czyrska-Filemonowicz, Acta Mater. 45 (1997) 4901–4907.
[5.33] M Sakane, H. Tokura., Int J Damage Mech 11 (2002) 247.
[5.34] D.R. Hayhurst, J Mech Phys Solids, 20 (1972) 381390.
[5.35] C.S. Seok, B.K. Bae, J.M. Koo, K.L. Murty, Eng Failure Anal, 13 (2006), p. 389
[5.36] S. Gollapudi, I. Charit, K.L. Murty, Acta Mater. 56 (2008) 2406–2419.
[5.37] F.C. Monkman, N. J. Grant: Proc. ASTM， 1956, vol. 56, pp. 593-620.